

ULTIMATE LOAD AND DEFLECTION BEHAVIOUR OF CELLULAR BEAMS

By

Juliet Warren

961067006

Submitted in complete fulfilment of the
requirements for the degree of
Master of Science
in the
School of Civil Engineering, Surveying and Construction
University of Natal
2001

Durban

2001

ABSTRACT

Cellular beams were developed in 1987 and are an adaptation of castellated beams having many of the same advantages and disadvantages. There are no published results of tests on cellular beams and there is only one recognised method of analysis and design.

Full scale destructive tests were carried out for this investigation on eight cellular beams. Beams loaded at midspan and at the third points were tested. Failure load, failure mode and deflections were obtained for each beam.

The existing analysis method as well as three new methods for both ultimate load behaviour and deflections were checked against the experimental results. The existing method of analysis was found to be over-conservative in predicting failure loads and inaccurate in predicting deflections. The analysis method which best predicted the failure loads and modes was the design chart which was developed for this investigation. The theoretical method which best predicted the deflection was the Vierendeel method which was also developed for this investigation.

CONTENTS

	page
List of Symbols	i
List of Figures	iii
Acknowledgments	vi
1. Introduction	1
1.1 Use of cellular beams in practice	1
1.1.1 Development	
1.1.2 Comparison with solid-webbed beams	
1.1.3 Comparison with castellated beams	
1.1.4 Applications	
1.2 Problem statement	3
1.3 Previous research	4
2 Laboratory tests on cellular beams	6
2.1 Introduction	6
2.2 Test beam details	8
2.3 Fabrication of beams and test rig	10
2.3.1 Beams	
2.3.2 Test rig	
2.4 Test procedure	13
2.4.1 Beam preparation and instrumentation	
2.4.2 Test procedure	
2.5 Test results	14
2.6 Summary	26
3 Ultimate load analysis	27
3.1 Introduction	27
3.2 Potential modes of failure	28
3.2.1 Pure Bending	
3.2.2 Vierendeel mechanism	
3.2.3 Horizontal shear	
3.2.4 Shear buckling of a web post	
3.2.5 Compression buckling of a web post	
3.2.6 Compression buckling of a tee section	
3.2.7 Lateral-torsional buckling	
3.3 Existing method of analysis	33
3.4 Proposed new methods of analysis	39
3.4.1 Plastic analysis	39
3.4.1.1 The Computer Program	39
3.4.1.2 The Spreadsheet	54
3.4.1.3 Design charts	60
3.4.2 Finite Element Analysis	70
3.5 Summary	79

4	Deflections of cellular beams	82
4.1	Introduction	82
4.2	Existing methods of analysis	82
4.2.1	British Steel Construction Institute Method	82
4.2.2	Simplified British Steel Construction Institute method	87
4.3	Proposed new methods	89
4.3.1	Vierendeel Method	89
4.3.2	Finite Element Analysis	92
4.4	Summary	95
5	Conclusions	100
5.1	Introduction	100
5.2	Experimental work	100
5.3	Ultimate load behaviour	100
5.4	Deflections	101
5.5	Summary	101
5.6	Future Work	102
6	References	103
7	Appendices	105
	Appendix A1	105
	Drawings of test beams	105
	Positions of strain gauges and dial gauges	110
	Positions of lateral supports	115
	Appendix A2	119
	Stress strain curves	119
	Mesh for Finite Element Analysis	120
	Graphical comparisons between experimental and FEA nodal stresses	125
	Appendix A3	140
	Graphical comparisons between theoretical and experimental deflections	140
	Deflection ratios for each dial gauge position	156

LIST OF SYMBOLS

A_{tee}	Area of tee section
A_z	Area of narrowest part of web post
c	width of equivalent rectangle
D_o	Diameter of opening
E	Young's modulus
f_y	yield stress
f_{yf}	yield stress of flange
f_{yw}	yield stress of web
f_w	effective yield stress of web after adjustment for shear
f_x	stress caused by bending
F_{tee}	axial force that the tee section can develop
F_{vh}	horizontal shear resistance of the web post
F_{vy}	vertical shear resistance of a section
G	shear modulus
h	lever arm between centroids of top and bottom tee sections
H	Height of the beam
h_s	depth of equivalent rectangle
h_t	height of tee section
h_w	height of web at tee section
I	second moment of area
L	span of beam
m	actual bending moment in the beam (design charts)
M	maximum bending moment that can be resisted by the beam (design charts)
M_e	elastic bending resistance of the perforated section
M_p	plastic bending resistance of the perforated section
M_u	applied bending moment
N	axial force in the tee from bending moment caused by the unit load
P	applied load for Euler deflection calculations
P_o	transformed axial force
P_u	resistance of the inclined section
q	actual vertical shear force in the beam (design charts)
Q	maximum vertical shear that can be resisted by the beam (design charts)
q_v	shear force causing a given Vierendeel bending moment
R	Radius of opening
S	Spacing of openings, centre to centre
T	axial force in the tees due to primary bending
t_f	thickness of flange
t_w	thickness of web
V	vertical shear force in the beam
V_h	horizontal shear force
w_f	width of flange
Z	section modulus

δ	deflection due to one opening
Δ	total deflection
$\varepsilon_{a,b,c}$	strains from strain gauges
$\varepsilon_{1,2}$	major and minor principle strains
γ	shear stress
θ	angle between ε_a and the major principle strain
σ	stress
σ_{\max}	outer fibre bending stress
τ	average shear stress in the web

LIST OF FIGURES

Chapter 1

Figure 1.1 : Incoming secondary members

Figure 1.2 : Beam layouts

Chapter 2

Figure 2.1 : Lateral support used by Hosain and Spiers

Figure 2.2 : Lateral support used by Okubo and Nethercot

Figure 2.3 : Lateral support used by Nethercot and Kerdal

Figure 2.4 : Fabrication of a castellated beam

Figure 2.5 : Fabrication of a cellular beam

Figure 2.6 : Test rig for experimental work

Figure 2.7 : Typical test beam setup

Figure 2.8 : Lateral support

Figure 2.9 : Failure of Beam 1A

Figure 2.10 : Yield pattern for Beam 1A

Figure 2.11 : Failure of Beam 1B

Figure 2.12 : Yield pattern for Beam 1B

Figure 2.13 : Failure of Beam 2A

Figure 2.14 : Yield pattern for Beam 2A

Figure 2.15 : Failure of Beam 2B

Figure 2.16 : Yield pattern for Beam 2B

Figure 2.17 : Failure of Beam 3A

Figure 2.18 : Yield pattern for Beam 3A

Figure 2.19 : Failure of Beam 3B

Figure 2.20 : Yield pattern for Beam 3B

Figure 2.21 : Failure of Beam 4A

Figure 2.22 : Close up failure of Beam 4A

Figure 2.23 : Close up of opening failure, Beam 4B

Figure 2.24 : Buckling of Beam 4B

Chapter 3

Figure 3.1 : Vierendeel mechanism in a castellated beam.

Figure 3.2 : Equivalent rectangular openings for castellated and cellular beams

Figure 3.3 : Elastic Vierendeel analysis

Figure 3.4 : Plastic Vierendeel analysis

Figure 3.5 : Free body diagram for horizontal web shear failure

Figure 3.6 : Section considered for web buckling calculations

Figure 3.7 : Section considered for web buckling calculations

Figure 3.8 : Sahlmel's curved beam approach

Figure 3.9 : Forces and lever arms

Figure 3.10 : Centroids for equal areas

Figure 3.11 : Theoretical and experimental failure loads, SCI method

- Figure 3.12 : Load case considered for computer program
- Figure 3.13 : Primary bending, low moment side
- Figure 3.14 : Primary bending, $x > t_f$
- Figure 3.15 : Primary bending, high moment side
- Figure 3.16 : Primary bending, $x > h_w$
- Figure 3.17 : Decision-making chart for Vierendeel stress adjustments
- Figure 3.18 : Low moment side, Case 1
- Figure 3.19 : Low moment side, Case 1.1.1
- Figure 3.20 : Low moment side, Case 1.1.2
- Figure 3.21 : Low moment side, Case 1.1.2
- Figure 3.22 : Low moment side, Case 2
- Figure 3.23 : Low moment side, Case 2.1
- Figure 3.24 : Low moment side, Case 2.2.1
- Figure 3.25 : Low moment side, Case 2.2.2
- Figure 3.26 : High moment side, Case 1
- Figure 3.27 : High moment side, Case 1.1
- Figure 3.28 : High moment side, Case 1.2.1
- Figure 3.29 : High moment side, Case 1.2.2
- Figure 3.30 : High moment side, Case 2
- Figure 3.31 : High moment side, Case 2.1.1
- Figure 3.32 : High moment side, Case 2.1.2
- Figure 3.33 : High moment side, Case 2.2
- Figure 3.34 : Root-finding for the program analysis
- Figure 3.35 : Positions considered for failure with spreadsheet.
- Figure 3.36 : Cellular beam spreadsheet graph
- Figure 3.37 : Castellated beam spreadsheet graph
- Figure 3.38 : Calculated and experimental failure loads, spreadsheet
- Figure 3.39 : Equivalent rectangular opening for design charts
- Figure 3.40 : Calculations for design charts
- Figure 3.41 : Root-finding for the design charts
- Figure 3.42 : Features of the design chart
- Figure 3.43 : Pure bending failure design chart
- Figure 3.44 : Design chart for Beam 1A, midpoint loading
- Figure 3.45 : Design chart for Beam 1B, third point loading
- Figure 3.46 : Design chart for Beam 2A, midpoint loading
- Figure 3.47 : Design chart for Beam 2B, third point loading
- Figure 3.48 : Design chart for Beam 3A, midpoint loading
- Figure 3.49 : Design chart for Beam 3B, third point loading
- Figure 3.50 : Design chart for Beam 4A, midpoint loading
- Figure 3.51 : Design chart for Beam 4B. third point loading
- Figure 3.52 : Calculated and experimental failure loads, chart
- Figure 3.53 : Finite Element Analysis model, Beam 3B
- Figure 3.54 : Typical stress strain curve
- Figure 3.55 : Convergence of FEA solution
- Figure 3.56 : Beam 3A, Finite Element Analysis mesh
- Figure 3.57 : Principle stress directions from strain gauges
- Figure 3.58 : Comparison between FEA and strain gauges, Beam 1B, opening

- Figure 3.59 : Comparison between FEA and strain gauges, Beam 4A, flange
 Figure 3.60 : Calculated and experimental failure loads, chart
 Figure 3.61 : Normal distributions of failure ratios, including Beam 4B
 Figure 3.62 : Normal distributions of failure ratios, excluding Beam 4B

Chapter 4

- Figure 4.1 : Free body diagrams for SCI deflection calculations
 Figure 4.2 : Internal forces due to unit load
 Figure 4.3 : Summing methods for SCI deflection calculations
 Figure 4.4 : SCI deflections, Beam 2A
 Figure 4.5 : SCI deflections, Beam 3B
 Figure 4.6 : Deflection ratios for SCI method
 Figure 4.7 : Simplified SCI deflections, Beam 2A
 Figure 4.8 : Simplified SCI deflections, Beam 3B
 Figure 4.9 : Deflection ratios for simplified SCI method
 Figure 4.10 : Cantilever section for Vierendeel deflections
 Figure 4.11 : Vierendeel deflections, Beam 2A
 Figure 4.12 : Vierendeel deflections, Beam 3B
 Figure 4.13 : Deflection ratios for Vierendeel method
 Figure 4.14 : Deformation of Beam 2A
 Figure 4.15 : Finite Element deflections, Beam 2A
 Figure 4.16 : Finite Element deflections, Beam 3B
 Figure 4.17 : Deflection ratios for Finite Element method
 Figure 4.18 : Shear-to-moment and deflection ratios, SCI
 Figure 4.19 : Shear-to-moment and deflection ratios, simplified SCI
 Figure 4.20 : Shear-to-moment and deflection ratios, Vierendeel
 Figure 4.21 : Shear-to-moment and deflection ratios, FEA
 Figure 4.22 : Deflection ratios normal distributions.
 Figure 4.23 : Factored deflection ratios, normal distributions

ACKNOWLEDGMENTS

Thank you to Professor Dougherty for suggesting the project as well as all his help and guidance along the way.

This project was funded by the Southern African Institute for Steel Construction and the National Research Foundation.

Figure 1.1 is adapted from the Westok information brochure on cellular beams of 1993.⁹

Figure 1.2 is adapted from the Westok information brochure on cellular beams of 1997.¹⁴

Figure 2.1 is from “Experiments on Castellated Steel Beams” by Hosain and Speirs.⁷

Figure 2.2 is from “Web post strength in castellated steel beams” by Okubo and Nethercot.⁸

Figure 2.3 is from “Lateral-torsional Buckling of Castellated Beams” by Nethercot and Kerdal.⁵

Figures 3.1 and 3.5 are adapted from “Castellated beams: A state of the art report” by BK Dougherty.¹¹

Figures 3.3 and 3.4 are from “Castellated beams: A state of the art report” by BK Dougherty.¹¹

Figures 3.6, 3.7, 3.8, 4.1 and 4.2 are adapted from the Steel Construction Institute Cellular beam design guide.¹⁰

Figure 3.54 is from the MSc thesis “Serviceability Limit States of Composite Beams” by Paolo Trinchero.¹

Thank you to Impact Engineering for the fabrication of the test beams.

Thanks are due to Mr M Sanders and Mr C Parel and their assistants in the laboratory for their help in the fabrication of the test rig and the testing procedure.

Thanks must go to my mother, Mrs JL Warren, for assisting in the proof reading of this thesis.

CHAPTER 1

INTRODUCTION

1.1 Use of cellular beams in practice

1.1.1 Development

Cellular beams were introduced in 1987; and were initially developed for architectural purposes where circular openings in exposed steelwork were considered to be aesthetically pleasing.. Westok Structural Service Ltd. are the inventors and patent holders of the cellular beam ⁹. Circular web openings were previously achieved by burning a circle in the web of a Universal section. A double cut profiling process was developed to fabricate cellular beams working on the same principles as castellated beams ¹⁰.

Castellated beams may be regarded as the forerunner of cellular beams, and were developed primarily to improve the structural efficiency of rolled I beams. Castellated beams were first used in 1910 by HE Horton of the Chicago Bridge and Iron Works. A British patent for castellated beams was granted to GM Boyd in 1939 and the beams were marketed in the United Kingdom in 1940 ¹¹.

1.1.2 Comparison with solid-webbed beams

Castellated and cellular beams have similar advantages over solid-webbed beams. The increase in height from the expansion process causes a corresponding increase in vertical bending stiffness. There is thus a saving in weight compared to a solid-webbed beam subjected to the same loading with the same span. The web openings can also be used as passages for services thereby reducing the floor-to-floor height. This significantly reduces the height of multistory buildings.

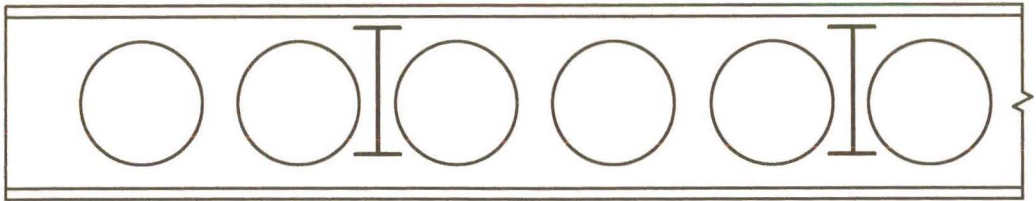
1.1.3 Comparison with castellated beams

The circular openings in cellular beams are more aesthetically pleasing than the hexagonal openings of castellated beams.

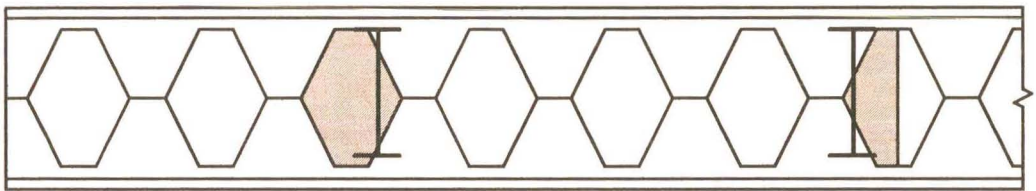
The double cut fabrication process for cellular beams wastes a small amount of material whereas the single cut process for castellated beams does not waste any material.

Cellular beams have a far more flexible geometry than castellated beams. Finished depth, opening diameter and opening spacing are all flexible dimensions in cellular beams, whereas in castellated beams the opening height fixes the finished depth and opening spacing. In consequence, cellular beams are frequently lighter than the most efficient castellated beam⁹. Cellular beam geometry can be arranged to eliminate the need for infill plates which greatly increase the cost of fabrication. Infill plates are used in castellated beams in areas of high shear at the ends of the beam or at positions of

concentrated loads. A cellular beam can be made to have a high resistance to shear by spacing the openings to give wide web posts. Conversely, where a member is lightly loaded, i.e. bending moments are dominant; a cellular beam will be chosen with the maximum depth and closely spaced openings to create a beam with the highest possible moment of inertia. Opening geometry can be adjusted to allow any incoming secondary members to connect onto a web post. (Figure 1.1)



Cellular Beam



Castellated Beam

Figure 1.1 : Incoming secondary members

Openings can be stiffened with a ring stiffener instead of the infill plates used for castellated beams. This has the advantage that the openings are still available for the passage of services.

1.1.4 Applications

Cellular beams can be used as floor beams or roof beams. They are most economical when used in long spans or when inclusion of services is a consideration. The Westok brochure¹⁴ advises that cellular beams are most economical when used as long span secondary members. (Figure 1.2) The layout of Figure 1.2(b) costs no more than traditional short spans using solid-webbed beams (Figure 1.2(a)). Additional benefits are column free floor space, fewer foundations and faster erection.

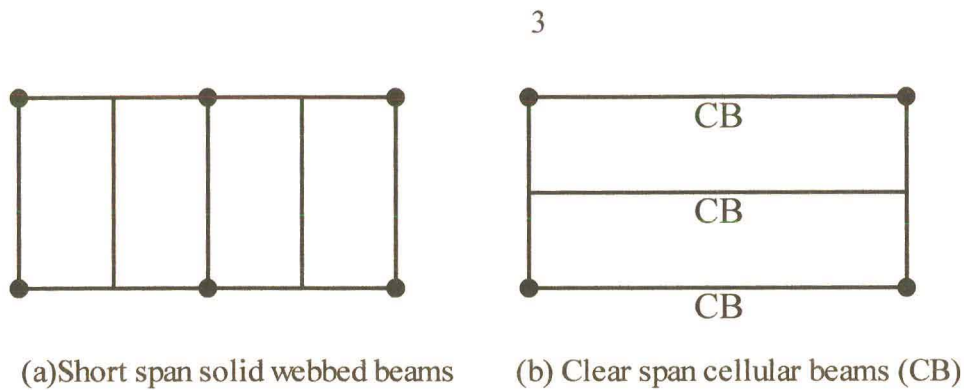


Figure 1.2 : Beam layouts

1.2 Problem statement

At present there is only one proposed method of analysing cellular beams, viz. the British Steel Construction Institute (SCI) method. This method was reported to have been verified by experimental tests,¹⁰ but neither the test results nor the verification of the analysis method have been published.

This project had the objects of compiling a set of results for experimental tests on cellular beams and finding an accurate, yet straightforward, method of analysis for calculating the failure loads, failure modes and service deflections.

Eight full scale cellular beams were tested to destruction and failure loads, failure modes and deflections were recorded. Four theoretical approaches were used to analyse the cellular beams for failure load and failure mode, viz.

- (i) SCI design method
- (ii) computer program and spreadsheet
- (iii) design charts
- (iv) Finite element analysis

Four theoretical approaches were used to analyse the cellular beams for deflections, viz.

- (i) SCI design method
- (ii) simplified SCI method
- (iii) Vierendeel deflection method
- (iv) Finite element analysis

The test beams were analysed using the SCI design method as given by Ward in the SCI publication¹⁰. The SCI method gives the failure load, failure mode and deflections. Two new methods were developed to model ultimate load behaviour, viz a computer program (and spreadsheet) and design charts. The spreadsheet was a refinement of the computer program which was based on plastic Vierendeel analysis. Failure load and failure mode were given by the spreadsheet for each test beam.

The computer program creates design charts which were used to obtain failure loads and

failure modes for the test beams.

A finite element analysis was carried out for each beam. The output from this analysis was failure load and deflections.

A new deflection method combining the effects of primary bending and Vierendeel bending was developed. Deflections for the eight test beams were calculated using this method.

The theoretical results were compared to the experimental results.

1.3 Previous research

Two series of full scale destructive tests were carried out previously on cellular beams, viz. at Bradford University in 1988, and at Leeds University in 1995, both supervised by the British Steel Construction Institute ¹⁴. The results of these tests have not been published. The design guide ¹⁰ mentions that web post flexural buckling was observed during the tests.

Previous tests had been confined to beams with isolated or pairs of circular openings. Redwood and McCutcheon ⁴ carried out a series of destructive tests on wide-flange steel beams under varying shear-to-moment ratios, where the openings were machine cut with a fly cutter. Deflections along the beams at each load increment were plotted against the moment at the opening to find the plastic failure moment.

Nine beams with circular openings were tested, four with single openings and five with pairs of openings. Of the five beams with pairs of openings, three had closely spaced openings (1,5 times the diameter centre to centre) and two had widely spaced openings (twice the diameter centre to centre).

A Vierendeel type failure was observed in the beams with single openings subjected to shear. A general yielding of the web surrounding the opening was seen rather than definite plastic hinges. The web yielding was displaced slightly to the load side of the opening.

The beams with pairs of openings subjected to low shear failed in the opening nearer the load in the same manner as those with single openings. A higher shear caused the web post to buckle and the pair of openings failed as a single unit.

The conclusions drawn were that the presence of shear reduced the moment capacity of the beam and that the beams with pairs of openings did not have a lower strength than those with single openings. It was found that the presence of circular web openings reduced the moment capacity of the beam by 64% to 72% depending on the shear-to-moment ratio.

Ravinger and Laščeková ¹⁵ carried out a series of tests on thin walled plate girders with

circular holes. Non-reinforced and reinforced openings were considered. The non-reinforced openings failed by buckling of the web around the opening because of the very thin webs. Cellular beams are unlikely to fail in this mode because the webs of universal sections are substantially thicker. It was recommended therefore that the openings be reinforced. This is expensive, however, and should be avoided wherever possible in cellular beams.

CHAPTER 2

LABORATORY TESTS

2.1 Introduction

Two series of experimental tests on cellular beams have previously been carried out under the supervision of the British Steel Construction Institute (SCI); one set at Bradford University in 1988 and the other at Leeds University in 1995. Both series comprised full scale destructive tests as described in the Westok information brochure⁹ but the results obtained have not been published.

A study of tests carried out on castellated beams was undertaken to determine the best test rig set up. Configuration of lateral supports was a concern and reports on three sets of previous experimental tests were consulted. Hosain and Spiers carried out a series of tests to investigate the effect of hole geometry on mode of failure⁷. Four lateral supports were used for each beam loaded at the third points, one at each load or reaction. Beams loaded at the midpoints had lateral supports at the load and reaction points and at the quarter points. Only the top flange was supported and teflon blocks were provided to allow free vertical deflections. (Figure 2.1)

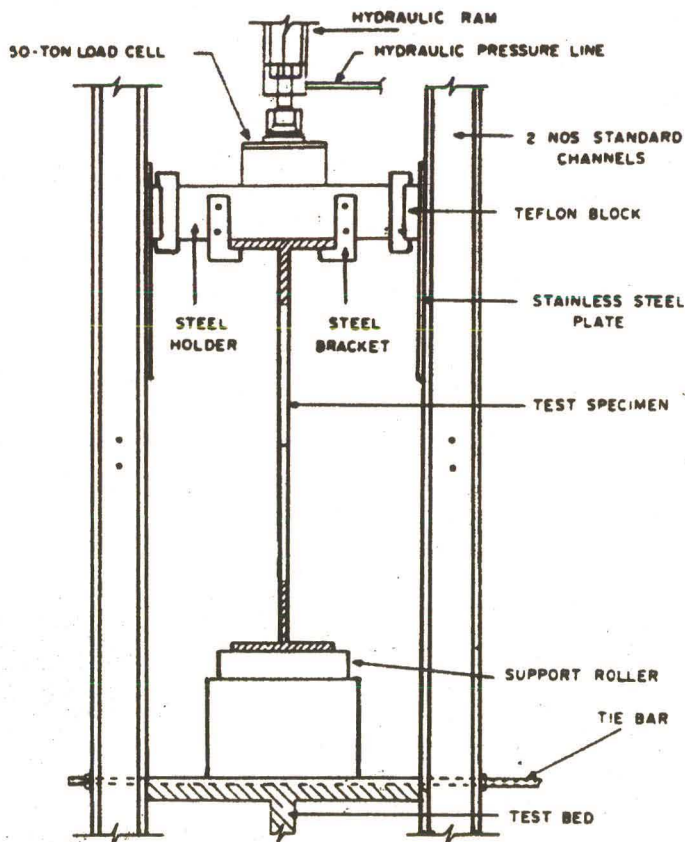


Figure 2.1 : Experimental setup used by Hosain and Spiers

Okubo and Nethercot⁸ performed a series of tests to determine the web post strength of castellated beams. The longest span tested was 3,2m and only the ends were laterally supported. Figure 2.2 shows the lateral support setup whereby the top flange was restrained by the support.

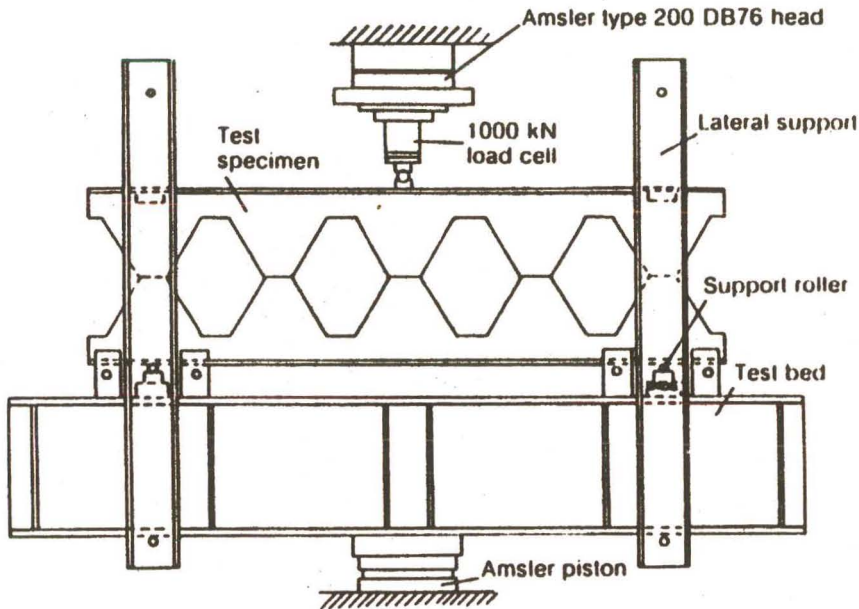


Figure 2.2 : Experimental setup used by Okubo and Nethercot

Nethercot and Kerdal⁵ carried out a series of tests to investigate lateral-torsional buckling of castellated beams. Lateral supports were placed at the loads and reaction points. The supports were in the form of yokes attached to the beam constrained to move in frames. (Figure 2.3)

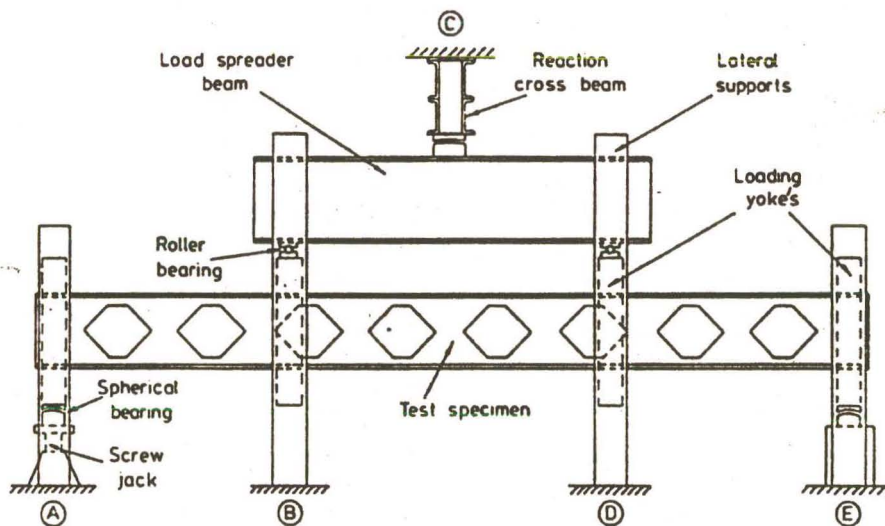


Figure 2.3 : Experimental setup used by Nethercot and Kerdal

It was concluded from the above that many lateral supports are needed along the length

of the beam. The design of the lateral supports was simplified but based on the three types given here. The lateral supports used are discussed in more detail in section 2.3.2.

The load incrementation method, viz. large increments initially then small increments to failure, was adopted on the basis of previous tests on beams with single, isolated openings carried out by Dougherty¹³. The method of painting the beams so as to reveal yield patterns was based on tests performed by Redwood and McCutcheon on beams with unreinforced web openings⁴. They noted that the paint flaked at lower values of compression than tension and this is shown to be so in the photographs in section 2.5.

The aim of the new tests was to investigate plastic behaviour of cellular beams. As is discussed later in section 2.2, the beams were chosen so as to avoid the possibility of web buckling failure.

2.2 Test beam details

Two different sizes of beam were chosen for testing, namely 203x133x25 and 305x102x25 I beams. These sizes were chosen as they are conveniently small sections, and ensured that the capacity of the testing equipment in the laboratory would not be exceeded. For each size two ratios of opening spacing to opening diameter were used, bringing the number of different beam geometries to four. The ratio of the opening spacing to the opening diameter determines the width of the web post and thus the tendency of the beam to fail in web buckling or shearing. The two sizes of beam chosen had different slenderness ratios (ratio of depth of beam to width of flange) and when combined with the variation in opening spacing gave a spread in beam geometry that covers the range likely to be encountered in practice.

Two loading conditions were chosen viz. midpoint and third point loading.

Spans were chosen so as to provide a wide variation in shear-to-moment ratio at the centre of the beam while avoiding web buckling or web post shearing. The beams were analysed using both the SCI method and the plastic method (which are discussed fully in Chapter 3) to eliminate the possibility of web post failure.

The different beam geometries are given in Table 2.1.

Table 2.1 : Test beam dimensions (in mm)

	Beam 1	Beam 2	Beam 3	Beam 4
Parent section	203x133x25	203x133x25	305x102x25	305x102x25
Height (H)	289,8	309,3	435	463,2
Cell Diameter (D_o)	200	225	300	325
Opening spacing (S)	300	300	450	400
Flange width (w_f)	133,4	133,4	101,6	101,6
Flange thickness (t_f)	7,8	7,8	6,8	6,8
Web thickness (t_w)	5,8	5,8	5,8	5,8

As can be seen from the above table, Beams 1 and 3 had an S/D ratio of 1,5 and Beams 2 and 4 a ratio of 1,33 giving them more slender web posts than Beams 1 and 3. Web post slenderness is the ratio of the diameter of the opening to the web post width.

The beams were further distinguished from each other by labeling all the beams to be loaded at the midpoint “A” and all those to be loaded at the third points “B”. Thus Beam 1A is a beam having the dimensions given in the first column of Table 2.1 and loaded at the midpoint.

The spans of the test beams are given in Table 2.2.

Table 2.2 : Test beam spans

Beam	span (m)
1A	3,1
1B	5,5
2A	3,8
2B	5,6
3A	3,8
3B	4,2
4A	8,2
4B	7,4

Appendix A1 contains detailed drawings of the test beams.

2.3 Fabrication of beams and test rig

2.3.1 Beams

Cellular beams are fabricated in similar fashion to castellated beams. Castellated beams are fabricated by cutting the web of a rolled I beam in a zig-zag pattern, turning the halves end to end and welding them together. (Figure 2.4) By comparison, cellular beams employ a double cut process (Figure 2.5) which, unlike the castellated beam, entails a small wastage of material.

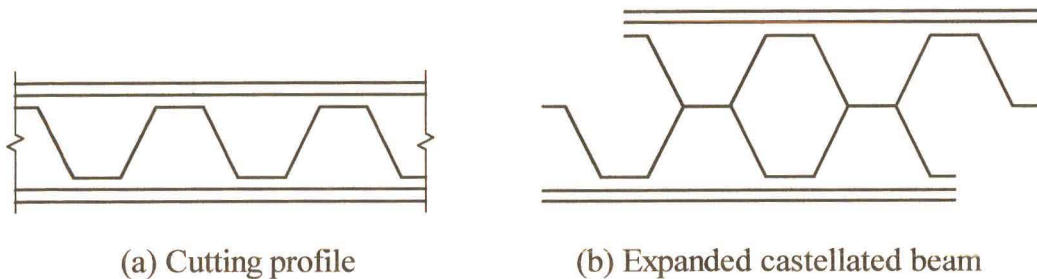


Figure 2.4 : Fabrication of a castellated beam

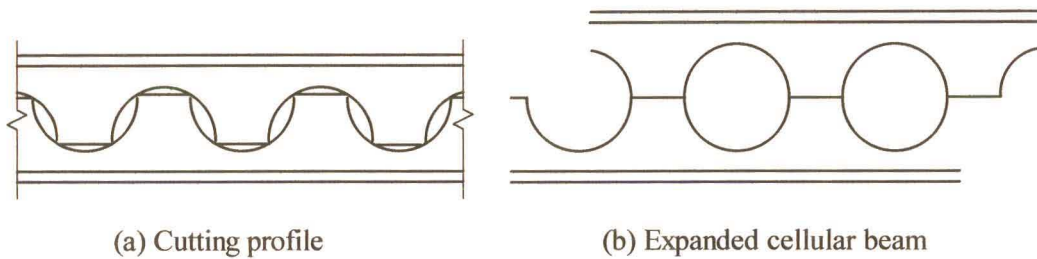
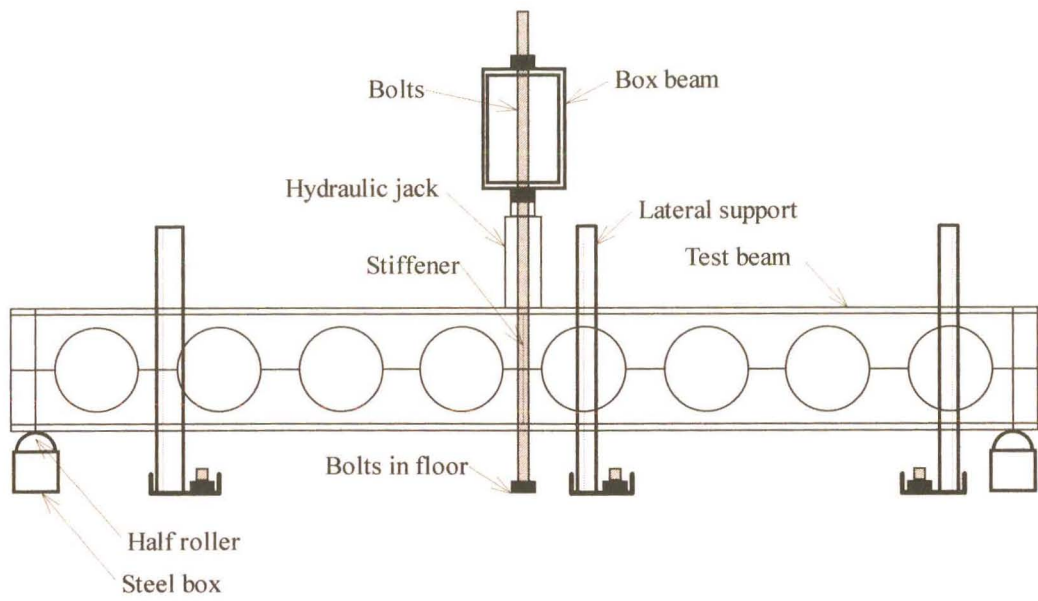


Figure 2.5 : Fabrication of a cellular beam

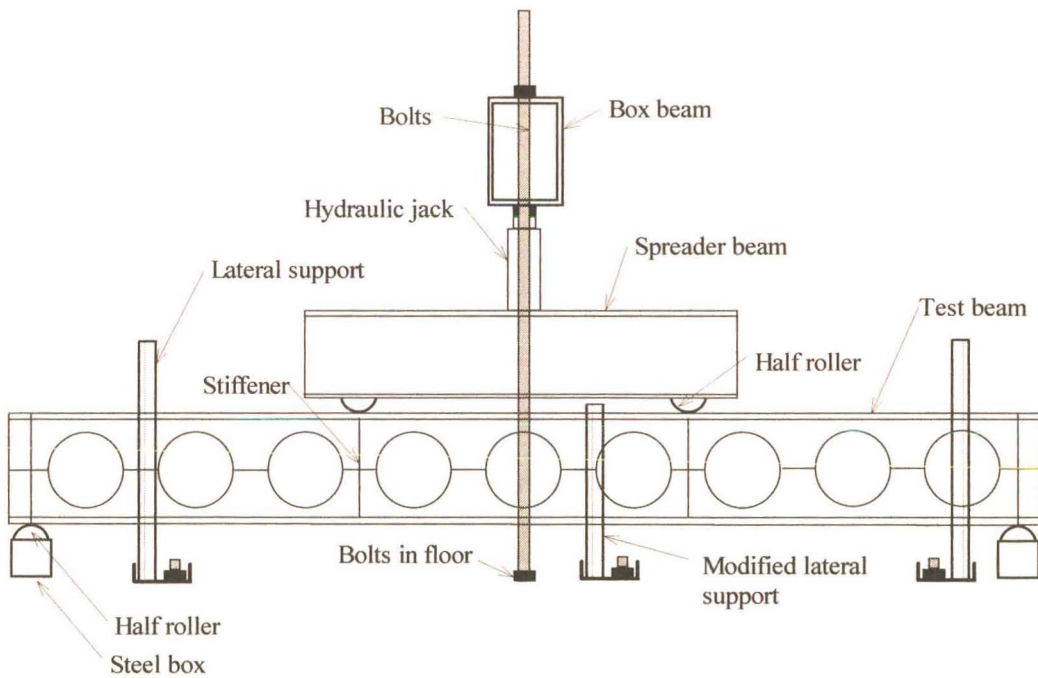
The beams used for the testing were fabricated by Impact Engineering. Full length web stiffeners were welded in at the positions of the end supports and the loads to prevent compression buckling of the web posts.

2.3.2 Test rig

The beams were tested in the heavy structures laboratory of the Civil Engineering Department of the University of Natal. The laboratory has a structural concrete floor with cast-in bolt sleeves that accommodated the tension rods used for beam loading and the bolts for securing the lateral support structures (Figures 2.6 and 2.7).



(a) Midpoint loading test rig



(b) Third point loading test rig

Figure 2.6 : Test rig for experimental work

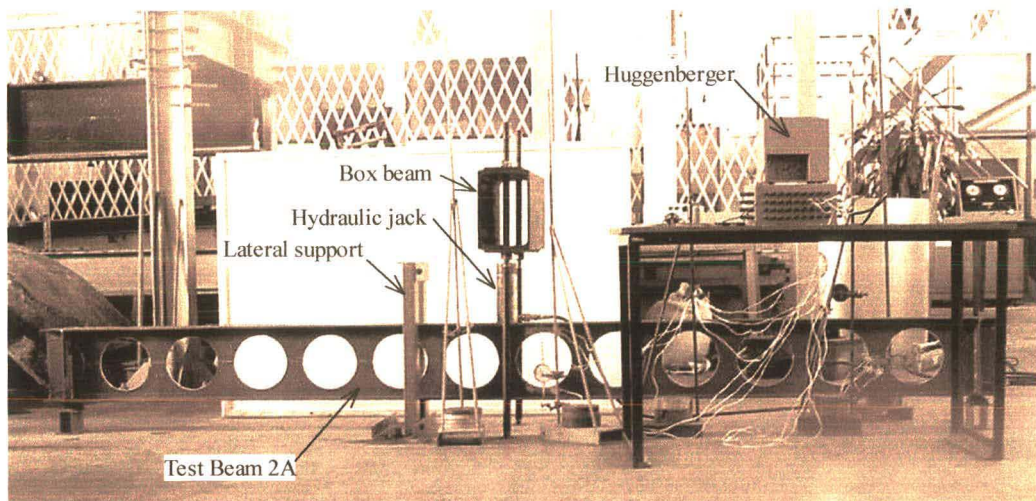


Figure 2.7 : Typical test beam setup

Lateral supports

The original lateral supports were made from channel sections welded together with an angle section joining the uprights at the top. (Figure 2.8) Beams that used the spreader beam, i.e. beams loaded at the third points, required a lateral support that fitted under the spreader beam. These lateral supports were modified by shortening the uprights and replacing the angle section with a flat plate. The lateral supports were also bolted to the structural floor.

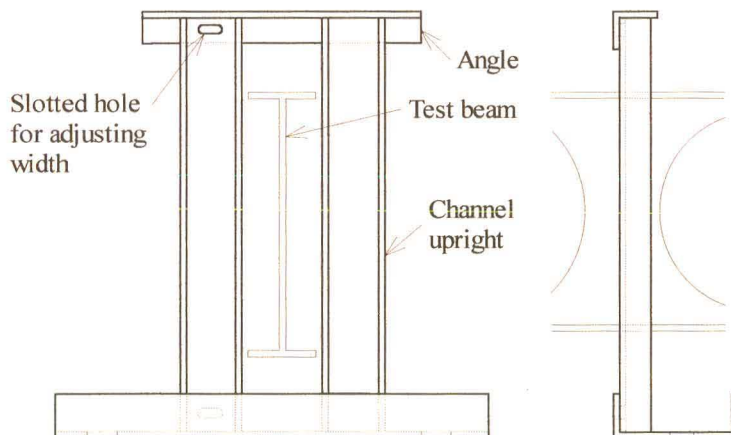


Figure 2.8 : Lateral support

End supports

The test beam was simply supported on each side by a half roller standing on a steel box made from two channels welded toe-to-toe. The half rollers were placed under the end stiffeners and covered the width of the flange. The steel boxes rested on the structural floor.

Loading

Loading was applied by a hydraulic jack acting against a box beam which was bolted to the floor, as shown in Figure 2.6. For beams loaded at the midpoint the jack was placed directly on the beam above the centre stiffener. A spreader beam was used to achieve third point loading. The spreader beam rested on two half rollers which were placed, flat side up, over the stiffeners at the third points. These half rollers also covered the width of the flange. The spreader beam was checked for moment resistance. Five pairs of web stiffeners were welded along the length of the beam to prevent twisting. The spreader beam had a mass of 122 kg, equivalent to 1,22 kN, which was added onto the applied load.

2.4 Test procedure

2.4.1 Beam preparation and instrumentation

The dimensions of each beam were measured and recorded.

Strain gauges were attached to the beams at the points where the highest stresses were expected to occur. These points were typically around the edge of the critical opening, along the flange under the centre of the critical opening and on the web post closest to the end support. Appendix A1 contains diagrams of the positions of the strain gauges for each beam. The strain gauges on the flange were single gauges running in the direction of the length of the beam; the gauges around the opening and on the web post were 45° rosettes. The strain gauges were attached to a Huggenberger strain bridge indicator which converts the voltage readings into millistrains.

The beam was painted with PVA on one side. When the metal yielded the paint cracked, and the yield pattern was revealed when the cracked paint was brushed off the beam.

Three vertical dial gauges were evenly spaced along half of the beam. Horizontal dial gauges were placed at the positions where horizontal movement was most likely; typically at the web post closest to the end support and in the centres of the laterally unrestrained sections. These gauges gave early warning of any horizontal movement at these points.

2.4.2 Test procedure

Two preliminary tests were carried out on each beam to 30% of the load predicted by the design charts. The preliminary tests were to ‘settle’ the loading rig, and to check the instrumentation. Strain gauge and dial gauge readings were taken at each increment during loading and after unloading. The strain gauges experience some hysteresis which improves with successive loading and unloading. Two cycles were sufficient to eliminate the hysteresis.

The test to failure was carried out in a similar way. The load increments were typically 10% of the predicted failure load up to 60% then 5% to failure. Strain gauge and dial gauge readings were recorded for each load increment. No readings were taken after unloading.

The gauge on the hydraulic jack measured the pressure exerted by the jack in Mega Pascals. The jack was calibrated to find the conversion factor between pressure and force. The load increments chosen were in values of Mega Pascals that could be easily read from the gauge.

The yield stresses of the flange and web of each beam were needed as input into the theoretical models. Yield test coupons were taken from areas of the beams distant from yielded areas, i.e. near the ends. Two coupons were taken from each the flange and the web. The yield stress was determined from a tensile test with the tension running in the same direction as the longitudinal axis of the beam.

2.5 Test results

Appendix A1 contains diagrams of the positions of lateral supports for each beam.

Beam 1A

Loading was in increments of 11,4 kN up to 80,1 kN then in increments of 5,7 kN to failure. Buckling of the flange above the centre opening was observed at a load of 114 kN, and at a load of 119,5 kN the beam continued to deflect under a constant load. This load was taken as the failure load. The failure was fully plastic Vierendeel failure in one of the openings adjacent to the load. (Figures 2.9 and 2.10)

The beam moved horizontally between the lateral supports by 2,15 mm. A horizontal movement of 2,62 mm at the unsupported end was observed after which the horizontal movement stopped. This indicated that settlement was taking place rather than buckling.

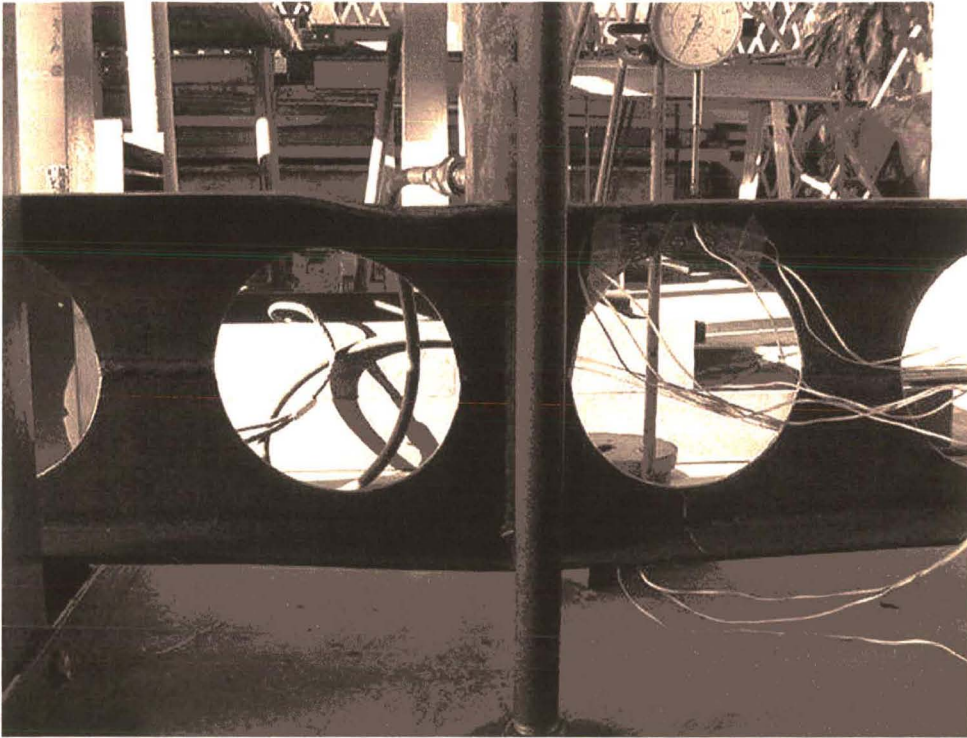


Figure 2.9 : Failure of Beam 1A

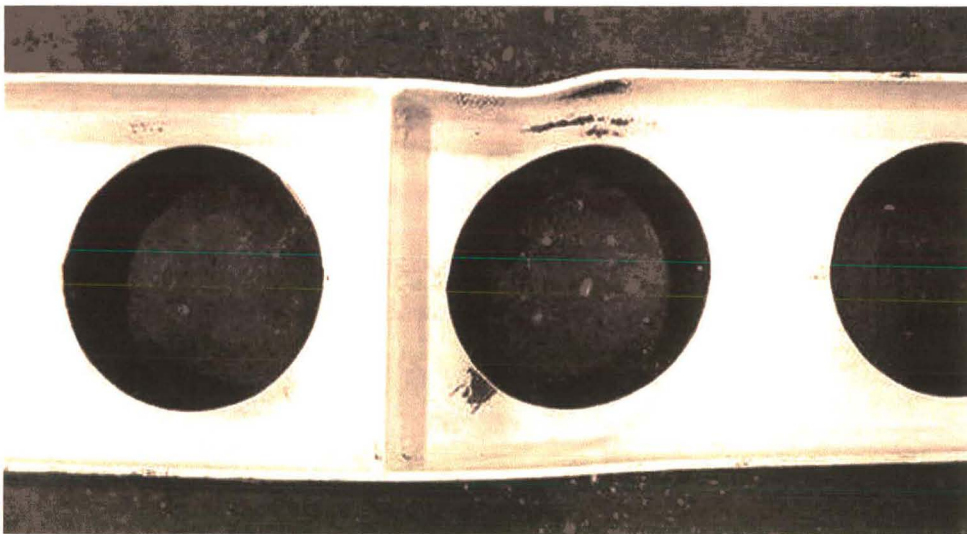


Figure 2.10 : Yield pattern for Beam 1A

Beam 1B

A horizontal displacement of 3mm was recorded during the second preliminary test at a total load of 45 kN. The rate of lateral displacement was constant indicating that the beam was still settling so loading began for the final test. After an initial settling period the rate of lateral displacement increased and the test was halted at a total load of 70 kN and a lateral displacement of 3,3mm. Distortion of the spreader beam was identified as a factor contributing to the lateral displacements. Web stiffeners were welded into the spreader beam to prevent further distortion. The beam showed no further tendency to move laterally, after initial settlement, and the test was carried out to failure.

The beam was loaded in increments of 11,4 kN total load up to 80,9 kN then in increments of 5,7 kN to failure. An increase in the rate of vertical deflection was observed at a load of 98 kN. At 108 kN the beam continued to deflect under a constant load, and this load was taken as the failure load.

Vierendeel failure was observed in the opening on the support side of each load. The failure was plastic with a slight lateral distortion. (Figures 2.11 and 2.12)

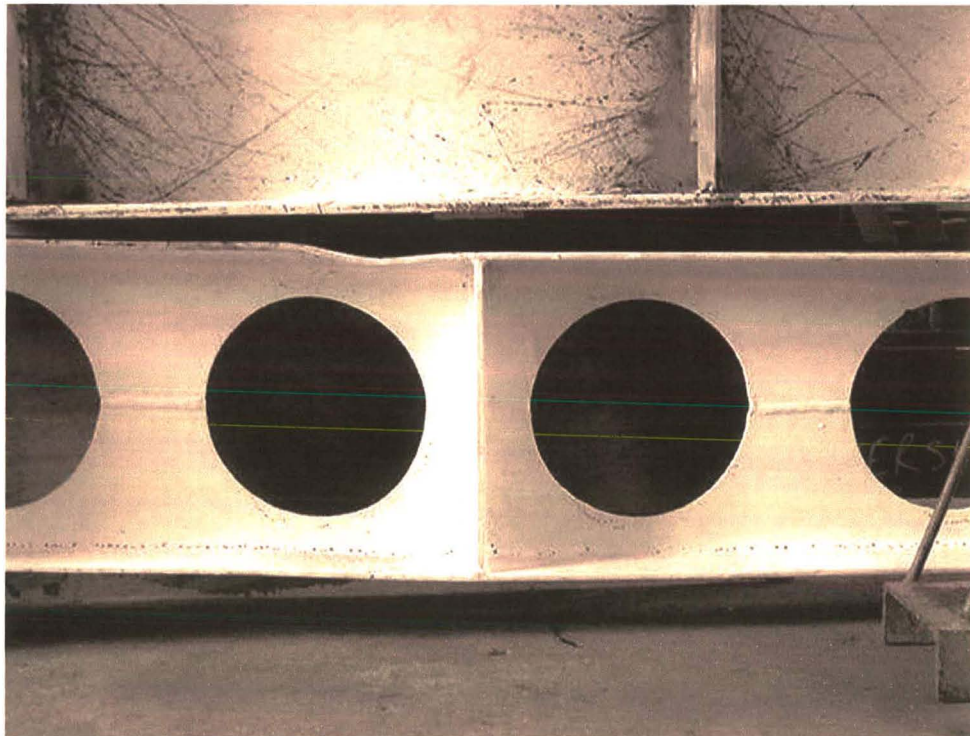


Figure 2.11 : Failure of Beam 1B

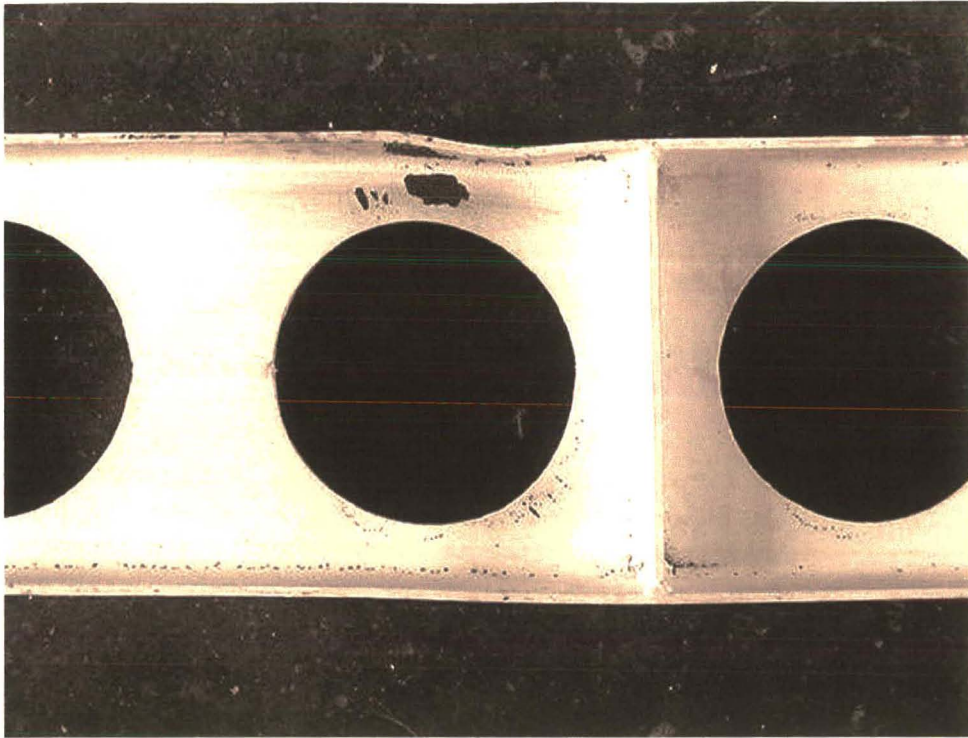


Figure 2.12 : Yield pattern for Beam 1B

Beam 2A

This beam showed no tendency to buckle.

Loading was in increments of 11,3 kN up to 79 kN then in increments of 5,6 kN to failure. At a load of 107 kN the flange at the centre of the beam began to buckle. The load was incremented further until the beam continued to deflect at a constant load of 112 kN. This load was considered the failure load. The failure was a fully plastic Vierendeel failure in one of the openings adjacent to the load. (Figure 2.13 and 2.14)

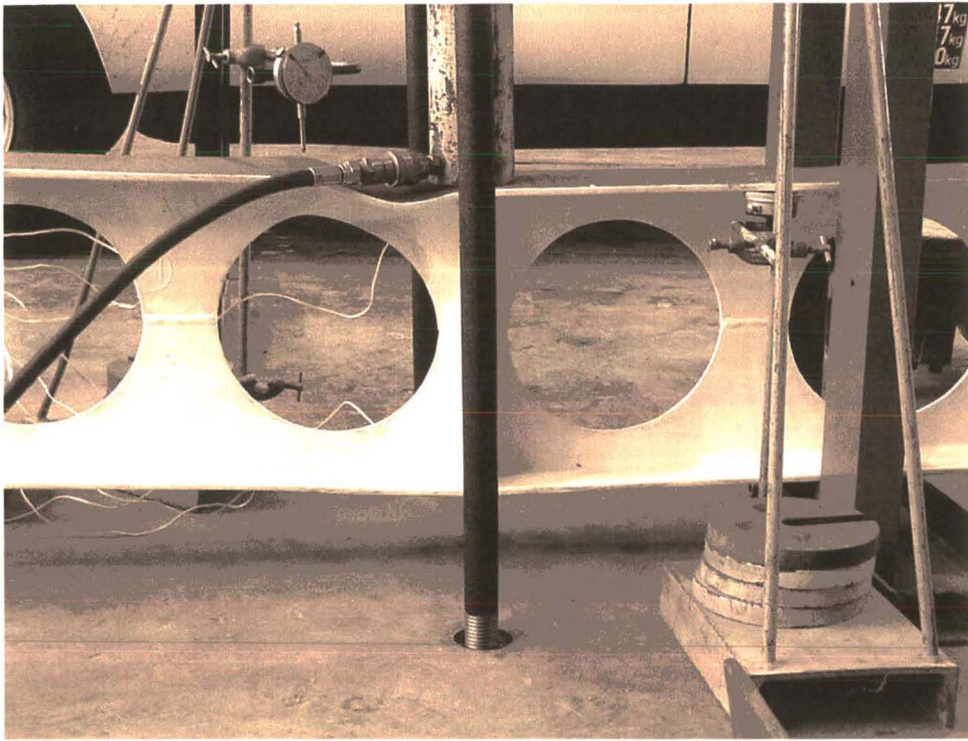


Figure 2.13 : Failure of Beam 2A

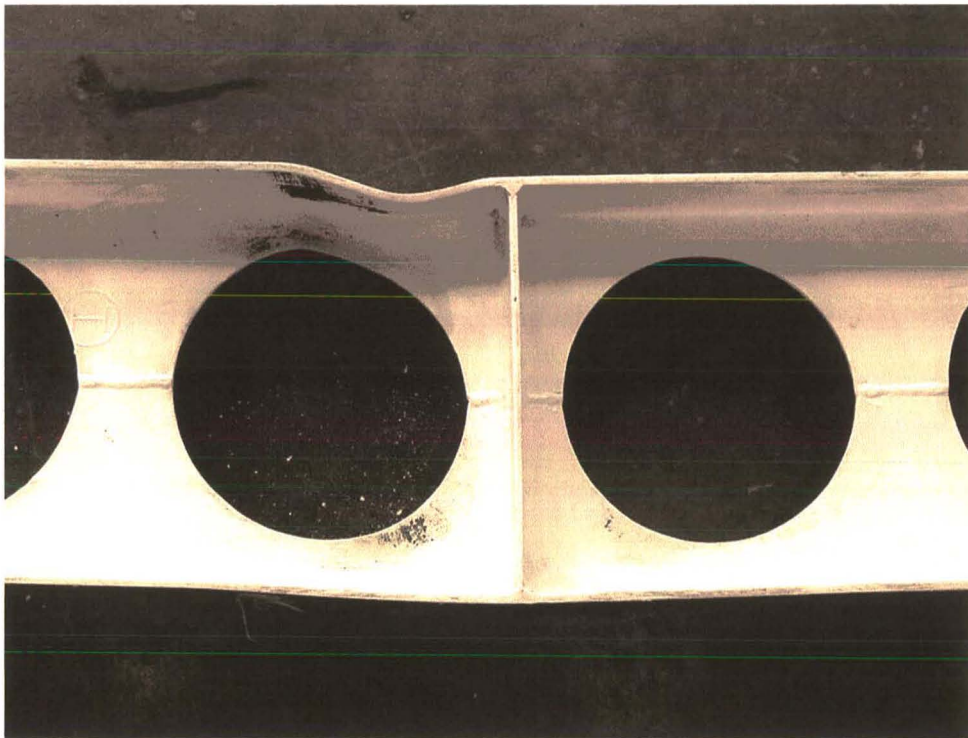


Figure 2.14 : Yield pattern for Beam 2A

Beam 2B

Loading was in increments of 11,4 kN total load up to 80,9 kN then in increments of 5,7 kN to failure. An increase in the rate of vertical deflection was observed at a load of 108 kN. The load was incremented further and the beam continued to deflect under a constant load of 117 kN, this load was taken as the failure load.

A lateral displacement of 4,77 mm was measured in the long laterally unsupported span in the centre of the beam at the end of the test. The lateral displacement did not cause buckling to occur before plastic failure was fully developed.

Vierendeel failure took place in the openings on the support side of both loads. (Figures 2.15 and 2.16) Some pure bending plastic deformation was observed in one of the openings in the central section of the beam.

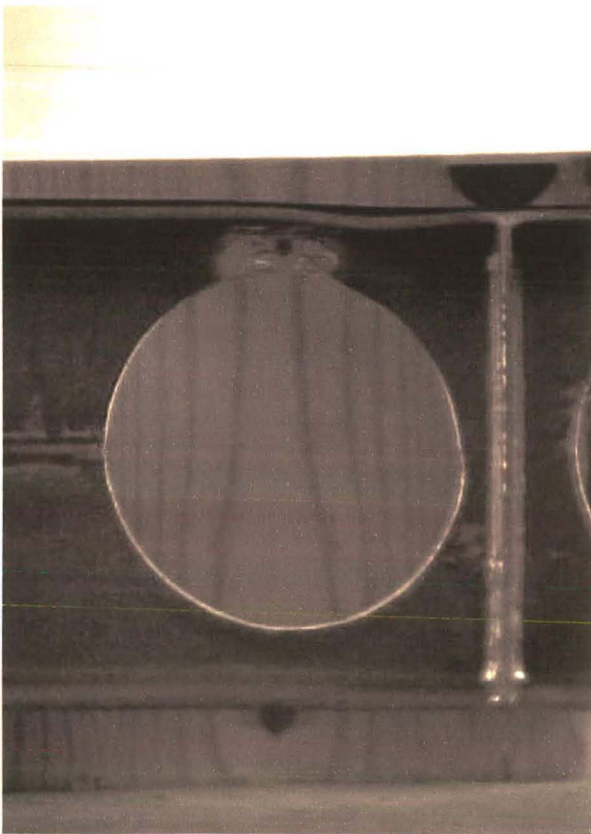


Figure 2.15 : Failure of Beam 2B

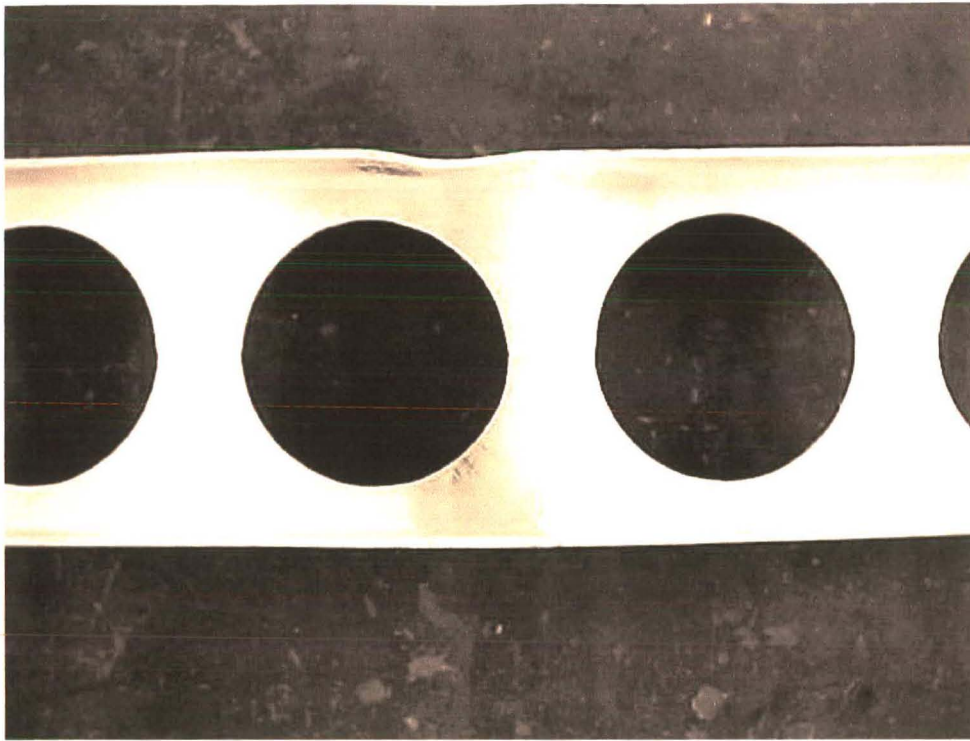


Figure 2.16 : Yield pattern for Beam 2B

Beam 3A

Loading was in increments of 11,4 kN up to 91 kN then in increments of 5,7 kN to failure. At a load of 142 kN the rate of deflection increased indicating that yielding was taking place. At a load of 151 kN the beam continued to deflect under constant load and this load was taken as the failure load. The beam failed in a fully plastic Vierendeel manner at both the openings adjacent to the load. (Figures 2.17 and 2.18)

A horizontal deflection of only 1,7 mm was recorded at the end of the test.

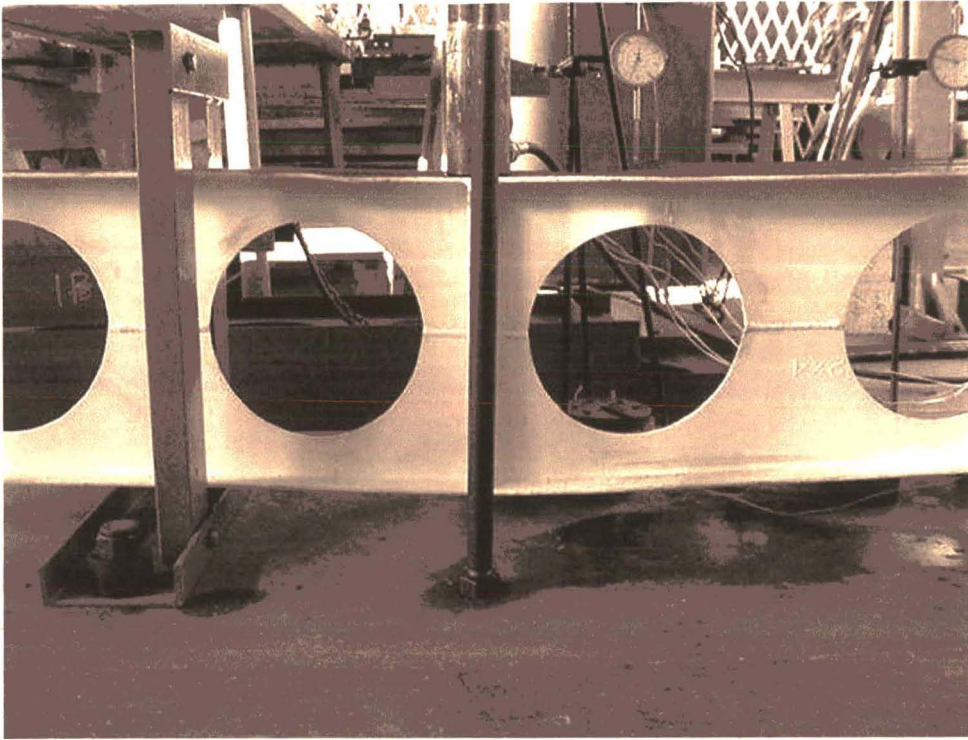


Figure 2.17 : Failure of Beam 3A

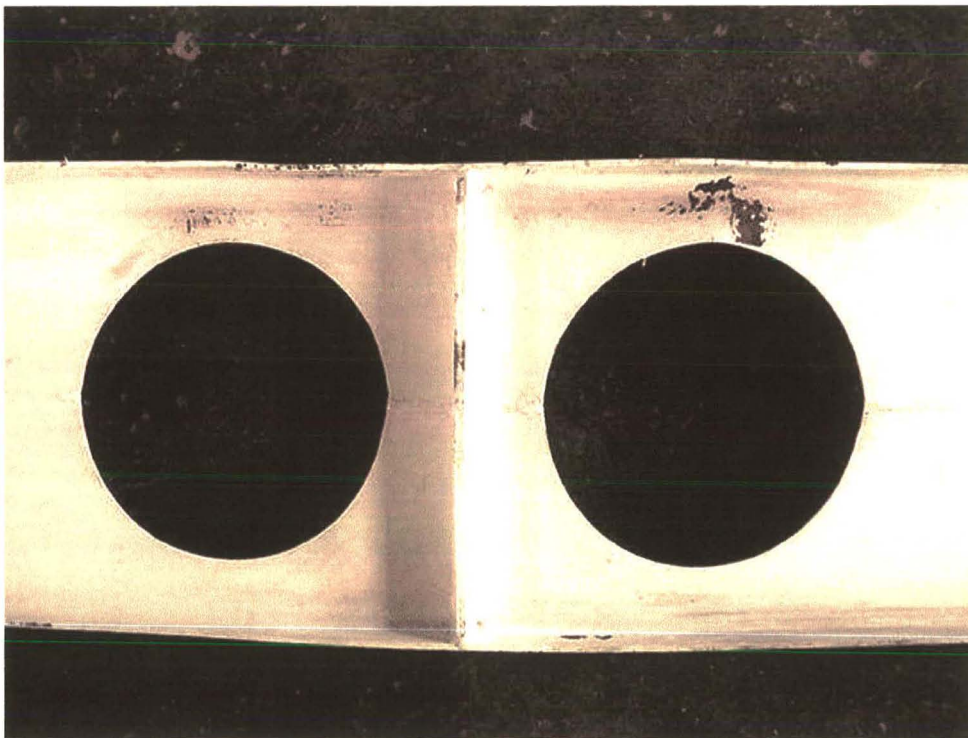


Figure 2.18 : Yield pattern for Beam 3A

Beam 3B

During the two preliminary tests no excessive lateral displacements were measured. The beam was loaded in increments of 11,4 kN. The rate of lateral displacement increased in the centre and at the ends of the beam, and at a load of 151 kN the test was halted. The beam recovered when the load was removed.

An extra lateral support was added to each end of the beam and the test procedure repeated. The beam deflected laterally throughout the test and at a load of 174 kN a large lateral displacement was noted and the test was halted. The beam made only a partial recovery with unloading and a 5 mm lateral distortion remained.

Two additional lateral supports were used in the final test. The beam was inverted so that the buckled compression flange became the tension flange. The lateral supports in the middle section of the beam were to one side of the centre so the beam was rotated horizontally to give lateral support to the buckled section. No gap was left between the lateral support uprights and the flange of the beam at the beginning of the test. At a load of 140 kN the beam began to buckle in an S shape between the supports. It was decided to continue the test and at a load of 193 kN the beam continued to buckle laterally at a constant load. Failure was deemed to have taken place.

Some vertical bending failure had occurred as could be seen from the distortion of the openings, yield patterns and the increased rate of vertical deflections. It was not fully plastic failure however as with unloading half the vertical displacement was recovered. The applied load of 193 kN was taken as the failure load but it is likely that if the lateral buckling had not taken place, a higher load would have been obtained. Vierendeel distortion was observed at the opening adjacent to the load on the support side, on one side only. (Figures 2.19 and 2.20)

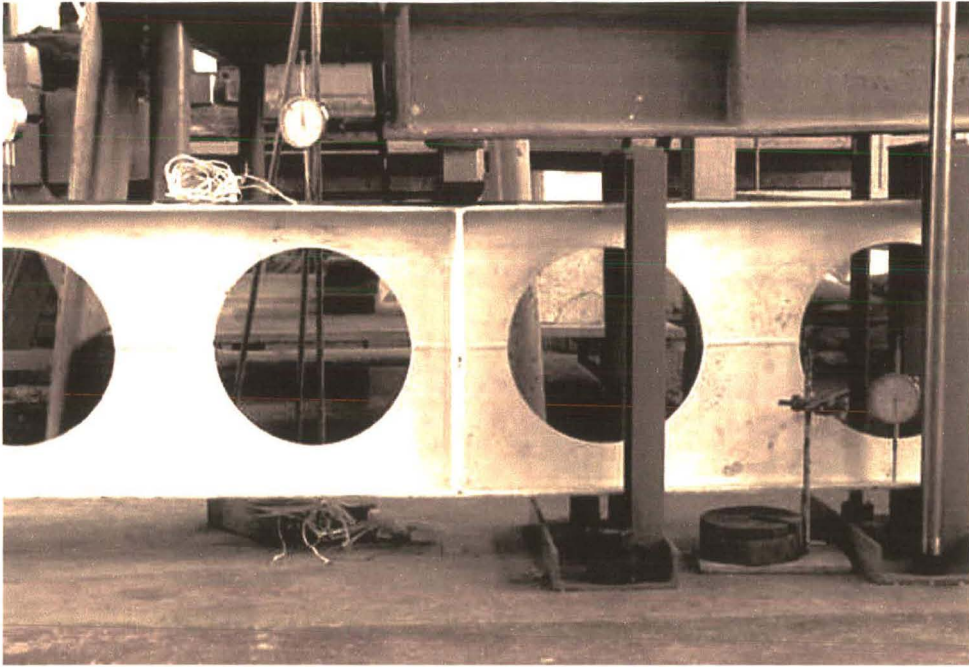


Figure 2.19 : Failure of Beam 3B

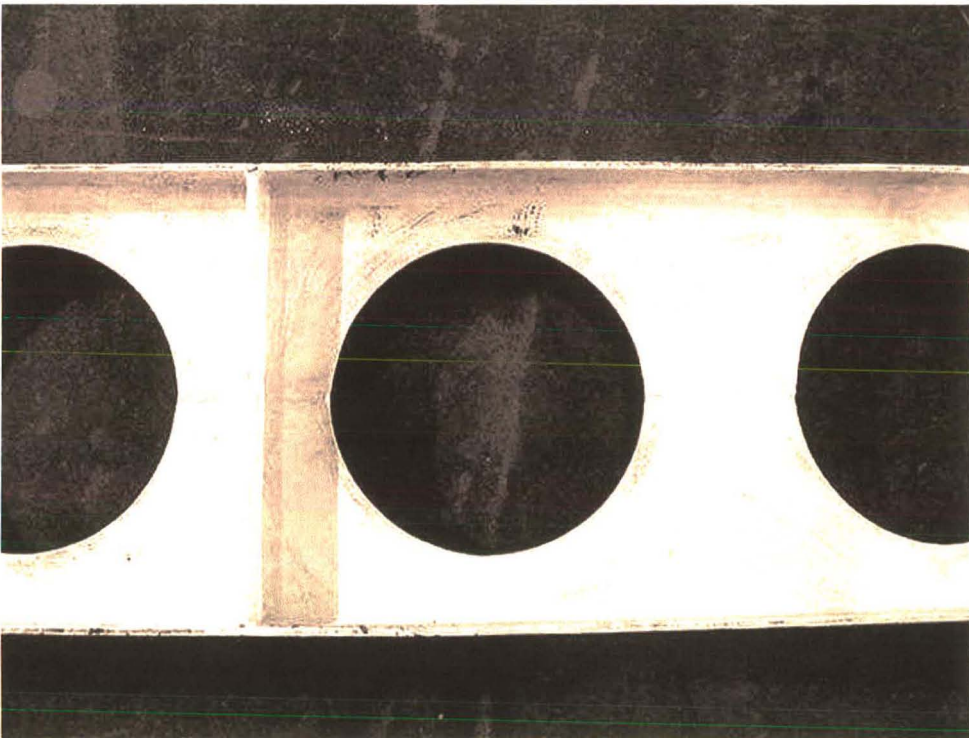


Figure 2.20 : Yield pattern for Beam 3B

Beam 4A

The beam showed no tendency to buckle laterally until plastic failure was well developed.

The beam was loaded in increments of 5,4 kN up to a load of 40 kN then in increments of 2,2 kN to failure. At a load of 65 kN the rate of vertical deflection increased and at a load of 90 kN the beam continued to deflect under constant load. This load was taken as the failure load.

This beam failed in a plastic primary bending mode. Little distortion can be seen in the openings of Beam 4A after failure because the failure was more of a pure bending failure than a Vierendeel failure. (Figures 2.21 and 2.22)

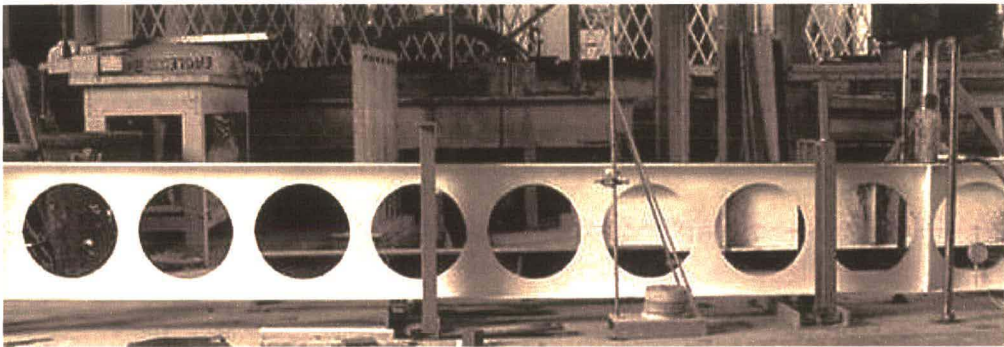


Figure 2.21 : Failure of Beam 4A

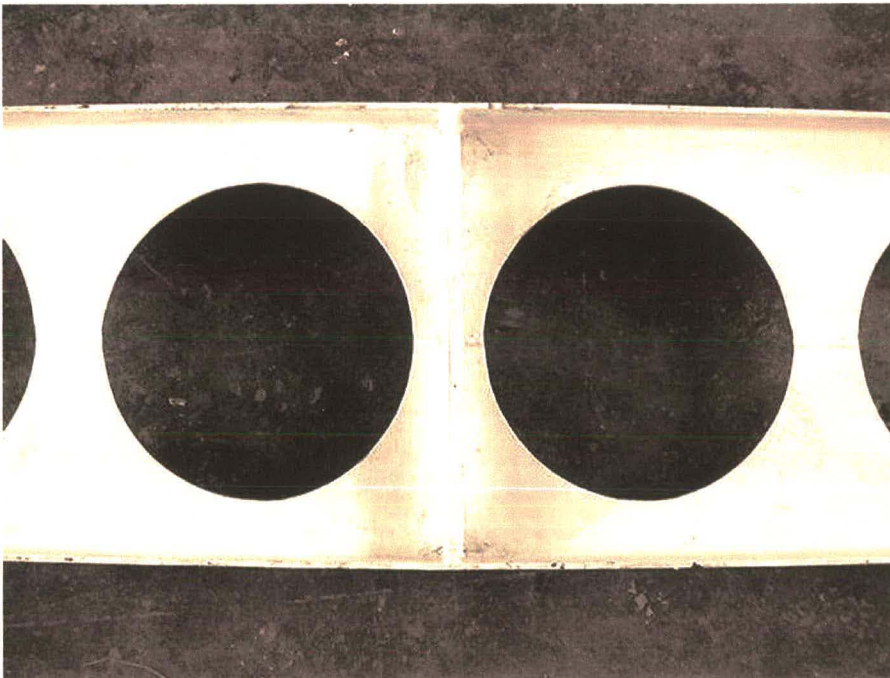


Figure 2.22 : Close up failure of Beam 4A

Beam 4B

Loading was in increments of 11,4 kN. At a load of 80 kN, the beam began to buckle in an S shape in the pure moment zone. The beam was unloaded and a further two supports were placed at the positions where buckling had occurred. The positions of the supports did not correspond with the positions of the bolts in the structural floor and weights were used to hold the supports in place. Insufficient weights were used and at a load of 102 kN the supports were pushed aside by the buckling of the beam. More weights were added with the result that buckling in the centre span of the beam was restrained and buckling occurred in the side span.

Once all the supports were in place and held firmly, the beam was loaded in increments of 23 kN up to 69 kN then in increments of 5,5 kN to failure at 114 kN. The rate of vertical deflection increased at 108 kN indicating that plastic failure was approaching. A slight distortion of the opening can be seen in Figure 2.21 indicating that Vierendeel failure was imminent. The beam buckled before fully developed plastic failure could occur. (Figures 2.23 and 2.24)

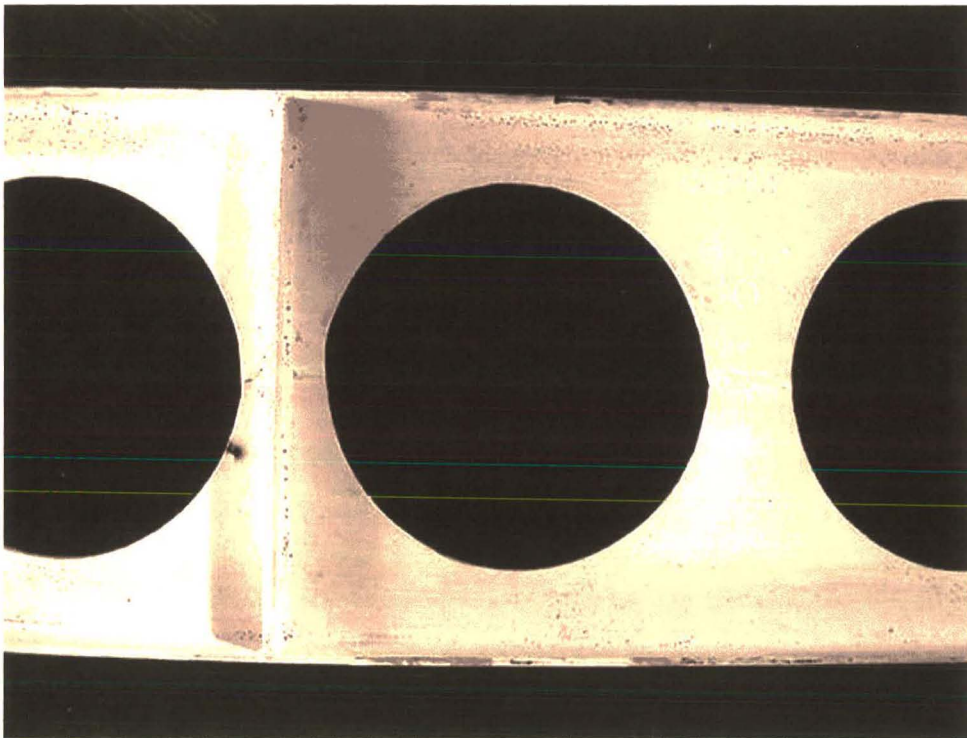


Figure 2.23 : Close up of opening failure, Beam 4B

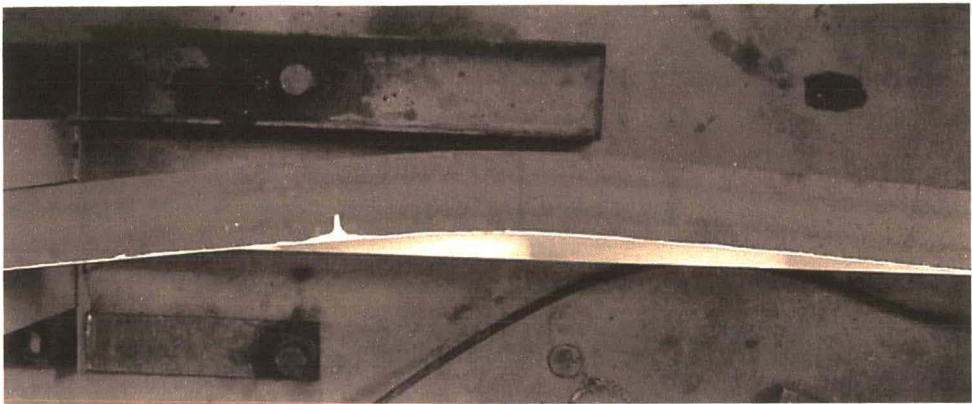


Figure 2.24 : Buckling of Beam 4B

2.6 Summary

Table 2.3 : Experimental results

Beam	Failure load	Failure Mode	Yield stress (flange)	Yield stress (web)
	kN		MPa	MPa
1A	119,5	plastic, Vierendeel	310	328
1B	108	plastic, Vierendeel	323	354
2A	112	plastic, Vierendeel	320	347
2B	117	plastic, Vierendeel	343	394
3A	151	plastic, Vierendeel, both openings	350	370
3B	193	plastic, Vierendeel/ buckling	337	343
4A	90	plastic, pure bending	437	430
4B	108	buckling/ slight evidence of plastic failure	360	390

CHAPTER 3

ULTIMATE LOAD ANALYSIS

3.1 Introduction

The cellular beams were analysed using four theoretical methods to predict failure loads and failure modes. All the possible modes of failure are given in section 3.2.

The first method used was the British Steel Construction Institute (SCI) design method from the SCI publication by Ward ¹⁰. The failure modes considered by the SCI method are pure bending, horizontal shear and buckling of a web post, vertical shear and Vierendeel bending. The analysis using the SCI method is discussed further in section 3.3.

A plastic analysis method was considered and developed into a computer program (section 3.4.1.1). The program makes simplifying assumptions, some of which were eliminated by producing a spreadsheet to carry out the analysis (section 3.4.1.2). The spreadsheet was used to analyse the beams.

The computer program is based on a very limiting load case. Design charts were developed which are created by the computer program. These design charts are able to handle any load case and would be a practical analysis tool for use in a design office. The design charts are discussed fully in section 3.4.1.3.

The plastic analysis methods check for Vierendeel bending, primary bending, horizontal shear of the web post and vertical shear failure.

A non-linear finite element analysis (FEA) was carried out for each beam using a commercial structural finite element analysis program, LUSAS. The models for each beam were developed involving the beam geometry, material properties, supports and loading. The output from the FEA was failure load and yield pattern. The FEA is discussed fully in section 3.4.2.

The failure loads and modes obtained from the four theoretical methods have been compared to the experimental results in the “Results” part of each section.

A summary and discussion of the comparisons between the theoretical and experimental results is given in section 3.5.

3.2 Potential modes of failure

3.2.1 Pure Bending ✓

This occurs when the beam is subjected to significant bending and minimal vertical shear. The beam can be analysed elastically or plastically using the properties of the perforated section.

For plastic analysis the top tee is regarded as fully stressed to the yield point in compression and the bottom tee fully stressed to the yield point in tension, thus forming a plastic hinge.

The plastic bending resistance of the beam is given by:

$$M_u \leq M_p = A_{tee} \times f_y \times h$$

The elastic bending resistance of a cellular beam is given by:

$$M_e = Z_x f_y$$

where $Z_x = \frac{2I}{H}$ is the elastic section modulus of the beam, using the properties of the perforated section.

3.2.2 Vierendeel mechanism ✓

This failure mechanism occurs when the beam is subjected to a significant vertical shear force. The tee sections above and below the openings are subjected to primary bending and shear. In addition to this, they are also subjected to a secondary Vierendeel moment caused by the shear force acting over a lever arm the length of the tee. The opening deforms as a parallelogram, causing crushing or tearing at the weakest points. Figure 3.1 illustrates such a failure for a castellated beam; cellular beams will evidently behave in similar fashion, though the positions of the plastic hinges are not so clearly defined.

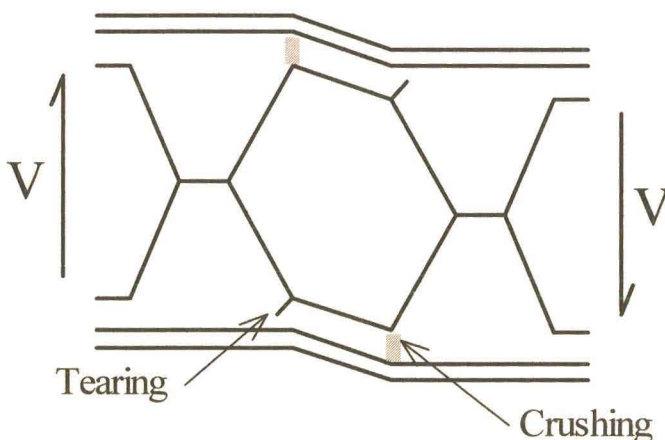


Figure 3.1 : Vierendeel mechanism in a castellated beam.

For a rectangular web opening, plastic hinges will form at the corners of the opening¹¹. Similarly in castellated beams the plastic hinges form at the top and bottom corners of the opening and the opening can be considered as a rectangle with the same depth h_s as the hexagonal opening and a width c equal to the length of the tee section (Figure 3.2).

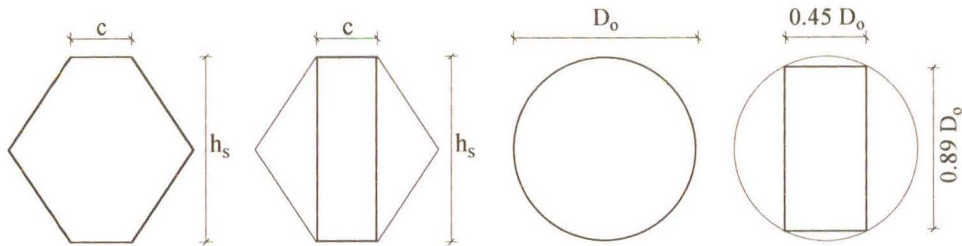


Figure 3.2 : Equivalent rectangular openings for castellated and cellular beams

Research into circular openings¹² suggested that the circular opening could be equated to a rectangular opening of width 0,45 times the diameter which gives a depth of 0,89 times the diameter. (Figure 3.2) It was found that a more accurate approximation to the width of the opening is 0,3 times the diameter, giving a depth of 0,95 times the diameter. This is discussed more fully in section 3.4.1.2.

The Vierendeel mechanism can be analysed using elastic or plastic methods. The two methods are discussed here briefly.

Elastic

The primary moment stresses are calculated at sections 1-1 and 2-2 in Figure 3.3, using the properties of the perforated section.

Two assumptions are made to render the structure statically determinate.

- (i) The vertical shear force divides equally between the top and bottom tees
- (ii) Points of contraflexure are at the centre of the tees.

The stresses caused by the Vierendeel moments are calculated using the section properties of the tees. The final design stress is the sum of the primary bending stress and the Vierendeel bending stress.

The elastic method was found to be inaccurate¹¹. The linear stress distributions inherent in this method were not confirmed by experimental work. The effect of the shear stress was ignored and it was found that this could effect the bending capacity of the tees. When plasticity develops, the point of contraflexure does not lie in the centre of the tee. The biggest criticism was that an elastic method should not be applied to an indeterminate structure. The allowable load is then dictated by peak stresses at critical sections leading to an inefficient utilisation of the section's stress capacity. Experimental tests confirmed this, giving large factors of safety when compared to the theoretical failure loads¹¹.

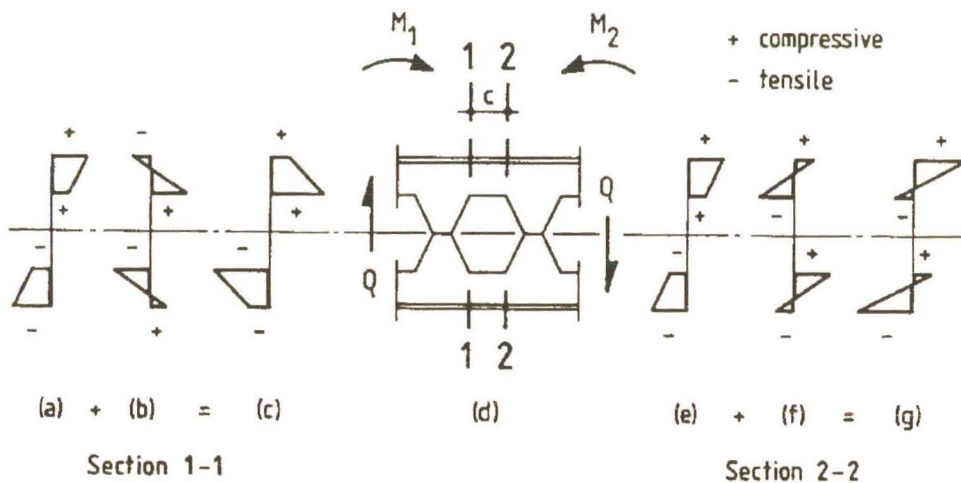


Figure 3.3 : Elastic Vierendeel analysis

Plastic

The plastic method treats the hexagonal opening as an equivalent rectangle, with a width c , which forms plastic hinges at the corners. The critical sections are fully stressed when a plastic hinge forms.

Two assumptions are made viz.

- (i) The shear and bending stresses interact according to Von Mises yield criterion. (Refer page 40) This has the effect of reducing the stress available for bending in the web of the tee section. f_w in Figure 3.4 is the effective yield stress in the web after the shear has been taken into account.
- (ii) The section is sufficiently ductile to allow the stresses to distribute in such a way as to maximise the section's resistance to bending.

The analysis is carried out in a similar way to the elastic analysis. The effective bending yield stress for the web is calculated by taking the shear into account. The primary bending stresses at the critical sections are calculated using the properties of the perforated section. The stress blocks are rectangular for plastic analysis. (Figure 3.4) The primary bending stresses effectively "prestress" the section to maximise its resistance to Vierendeel stresses. The stresses due to Vierendeel bending are calculated, if they act in the opposite direction to the primary bending stresses they can approach twice the yield stress because they partly cancel out when added together as can be seen from Figure 3.4. The final values of the Vierendeel stresses are dictated by horizontal equilibrium, tension equals compression.

There are no "peaked" stresses dictating artificially low strengths in the plastic method. This method is dealt with in detail in section 3.4.1.

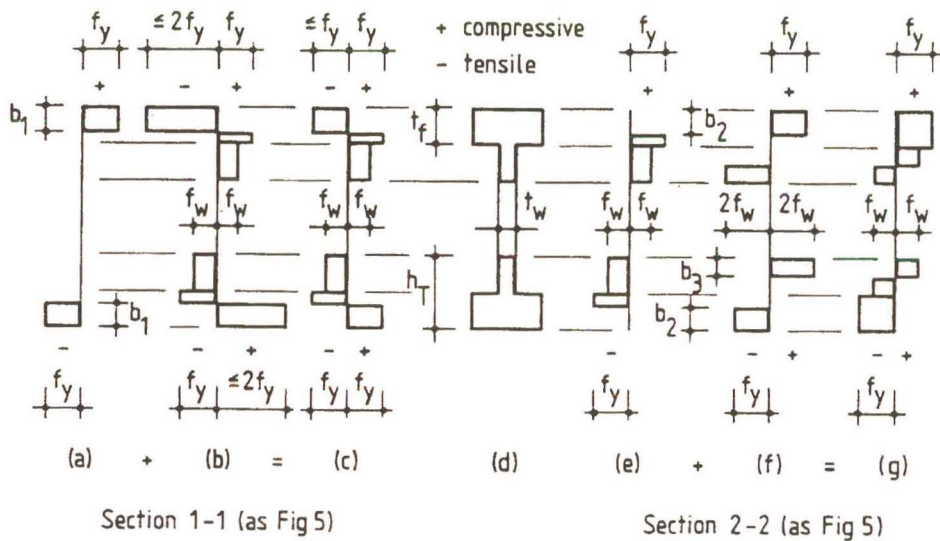


Figure 3.4 : Plastic Vierendeel analysis

3.2.3 Horizontal shear

The applied vertical shear induces a horizontal shear force V_h in the web post which can cause the web to fail at the weld. This horizontal shear V_h can be calculated by considering the free body of Figure 3.5 where T_1 and T_2 are the compressive forces due to the primary bending moment, and W is the applied vertical load. V_1 and V_2 are the shear forces at the centres of the adjacent tees. The shear force and the applied load are assumed to be equally distributed between the top and bottom tees. Taking moments

about the point A gives: $V_h = \frac{S(2V_1 - W)}{2H - 4t_f}$

In the special case when W is zero $V_1 = V_2 = V$ and $V_h = \frac{SV}{H - 2t_f}$. This is the case in the computer program (section 3.4.1) because of the load case considered.

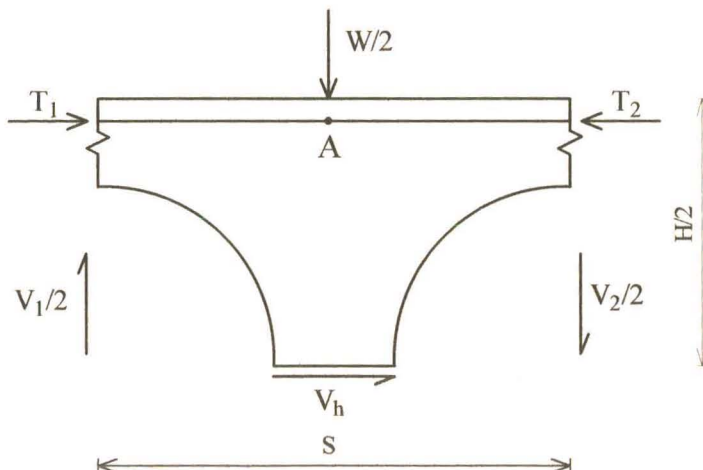


Figure 3.5 : Free body diagram for horizontal web shear failure

3.2.4 Shear buckling of a web post

The horizontal shear forces induced in the web post can cause it to fail in lateral-torsional buckling and this mechanism can be analysed elastically or plastically¹¹. The method of analysis used here for this failure mechanism is an elastic method taken from the British Steel Construction Institute design method and is based on the resistance of section A-A shown in Figure 3.6. The horizontal shear force causes a moment at section A-A which is compared to the section's elastic moment of resistance. This failure mechanism is dealt with further in section 3.3

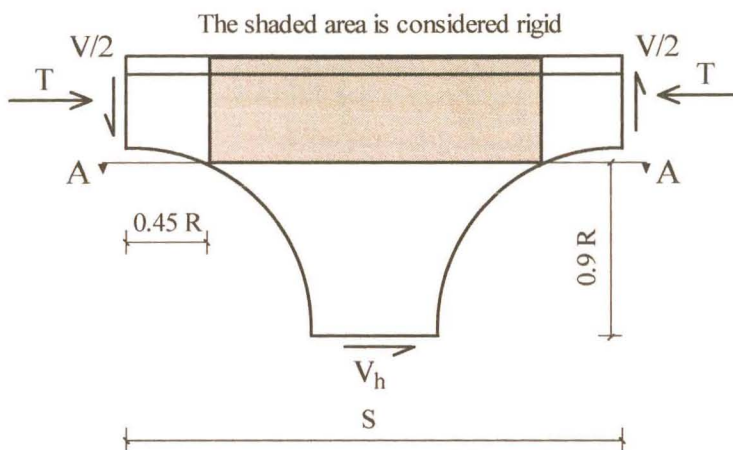


Figure 3.6 : Section considered for web buckling calculations

3.2.5 Compression buckling of a web post

This may occur when a concentrated applied load or reaction is applied directly above or below a web post. The web post buckles laterally (without twisting), as for web crippling in a solid webbed beam. The web posts can be treated as columns having a width equal to the narrowest section of the web post, a length equal to the depth of the opening, a thickness equal to the thickness of the web and an effective length factor of 0.5. Column curves can then be used to determine the compressive buckling strength of the web post.⁸

3.2.6 Compression buckling of a tee section

The tee section above the opening is not supported along the bottom edge and is subjected to compression from the primary moment, thus buckling of the tee section may occur. This type of buckling failure has not been observed in practice.¹¹

3.2.7 Lateral-torsional buckling

The behaviour of cellular beams does not differ significantly from castellated beams in lateral torsional buckling¹⁴. Nethercot and Kerdal carried out a series of tests

investigating lateral-torsional buckling of castellated beams⁵. It was observed that even with considerable lateral distortion of the beams, no additional distortion of the web posts occurred. It was found that the presence of the web openings had no noticeable effects on the lateral-torsional buckling behaviour of the beams. It was therefore recommended that castellated beams be analysed as for solid webbed beams, but that the section properties be those at the centre of an opening.

3.3 Existing method of analysis

British Steel Construction Institute Method ¹⁰

Theory

The Steel Construction Institute (SCI) design method is based on experimental work and the results of finite element analysis. Plastic analysis was used for the ultimate load analysis.

The method is only valid for beams that satisfy the following conditions:

- (i) simply supported
- (ii) $1,08 < \frac{S}{D_o} < 1,5$
- (iii) $1,25 < \frac{H}{D_o} < 1,75$

Five different failure mechanisms are checked in the ultimate load analysis:

(a) *Overall Beam Flexure*

This failure mechanism is the Pure Bending mechanism discussed in section 3.2.1 where a plastic hinge is formed in the centre of the opening due to both the tee sections having reached their full stress capacity in bending. Plastic methods are being used here so the check for this failure mechanism is given by:

$$M_u \leq M_p = A_{tee} \times f_y \times h$$

where M_u is the ultimate bending moment in the beam

M_p is the plastic moment that can be resisted

A_{tee} is the area of one tee section

f_y is the yield stress

h is the lever arm between the centroids of the top and bottom tee sections.

(b) *Shear*

Two sections of the beam are checked for shear resistance, viz. the centre of the opening for vertical shear, and the narrowest part of the web post for horizontal shear.

The vertical shear capacity is checked by:

$$V < F_{vy} = 0,6f_y(0,9\Sigma \text{ Tee web areas})$$

The horizontal shear capacity of the web post is checked by:

$$V_h < F_{vh} = 0,6f_y(0,9 \times \text{minimum area of web post})$$

where V and V_h are the vertical and horizontal shears in the beam respectively

F_{vy} and F_{vh} are the vertical and horizontal shear resistances of the sections respectively

(c) *Lateral Torsional Buckling*

The usual method of determining lateral torsional buckling strength can be employed using the beam properties through the centre of the opening as discussed in section 3.2.7.

(d) *Web Post Flexure and Buckling*

These design equations were based on a detailed linear and non-linear finite element analysis and a parametric study based on the ratios:

$$\frac{S}{D_o}; \quad \frac{D_o}{t_w}; \quad \frac{M}{M_e}$$

where $M = 0,9RV_h$ is the applied moment in the web post, at the section A-A, due to the horizontal force in the web. (Figure 3.7)

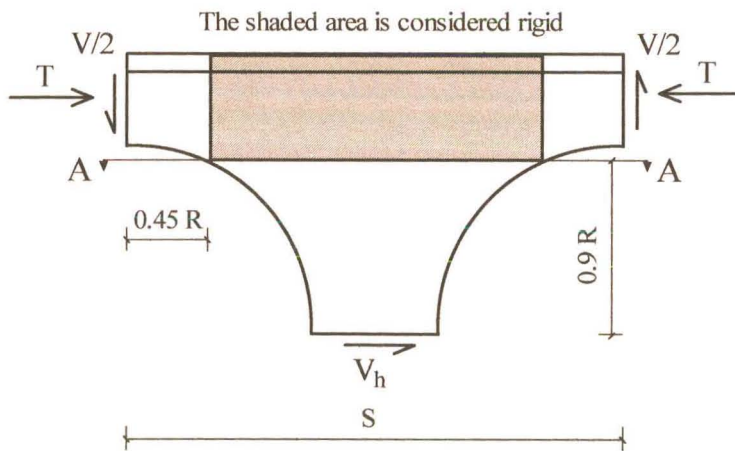


Figure 3.7 : Section considered for web buckling calculations

$M_e = Z_e f_y$ is the elastic moment which can be resisted by section A-A, where Z_e is the section modulus of the section A-A.

The ratios $\frac{S}{D_o}$ and $\frac{D_o}{t_w}$ were found to govern the web post buckling, and the design equation takes the form of a polynomial:

$$\frac{M}{M_e} = C_1 \left(\frac{S}{D_o} \right) - C_2 \left(\frac{S}{D_o} \right)^2 - C_3$$

where $C_1 = A_1 + A_2 \left(\frac{D_o}{t_w} \right) + A_3 \left(\frac{D_o}{t_w} \right)^2$

$$C_2 = A_4 + A_5 \left(\frac{D_o}{t_w} \right) + A_6 \left(\frac{D_o}{t_w} \right)^2$$

$$C_3 = A_7 + A_8 \left(\frac{D_o}{t_w} \right) + A_9 \left(\frac{D_o}{t_w} \right)^2$$

The coefficients A_1 to A_9 are given in Table 3.1.

Table 3.1 : Coefficients for the web buckling equation

A_1	A_2	A_3	A_4	A_5	A_6	A_7	A_8	A_9
5,097	0,1464	-0,00174	1,441	0,0625	-0,000683	3,645	0,0853	-0,00108

(e) *Vierendeel Bending*

Sahmel’s method for curved beams was used to analyse the openings for Vierendeel bending. The critical section was assumed to be at an angle of $\phi = 25^\circ$ from the vertical. (Figure 3.8)

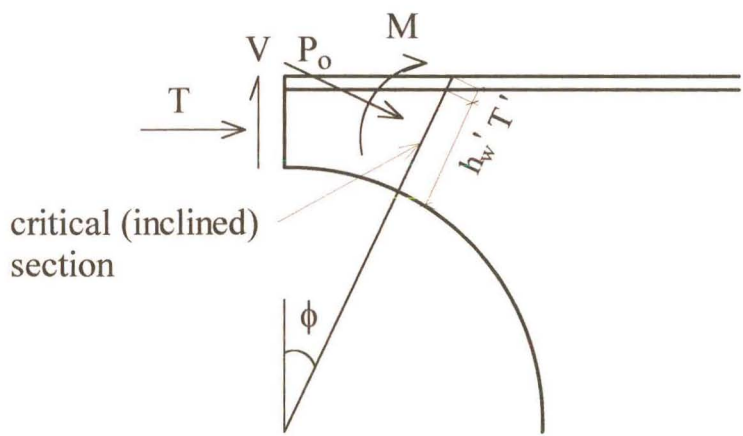


Figure 3.8 : Sahmel’s curved beam approach

The section dimensions are transformed to the dimensions of the inclined section so that:

$$T' = \frac{t_{fl}}{\cos 25^\circ}; \quad h'_w = \frac{H/2 - t_{fl}}{\cos 25^\circ} - \frac{D_o}{2}$$

The axial force and bending moment acting on the inclined section, as well as the section’s resistances, are calculated. The interaction between the Vierendeel moment

and the axial force is determined from the equation:

$$\frac{P_o}{P_u} + \frac{M}{M_p} \leq 1 \quad (\text{Eq. 3-1})$$

Application of the Theory

The SCI design method assumes that the flange and web have equal yield stresses. This was not the case for the beams that were used in the present experimental tests, and in applying the method the equations were adjusted to suit. This entailed using the axial force that a section could resist instead of the area of the section.

(a) Overall Beam Flexure

The plastic moment resistance of the section is found by taking moments of the forces that can be resisted by the section about the centroid of the section. (Figure 3.9)

$$M_u \leq M_p = A_{web} \times f_{y,web} \times h_{web} + A_{flange} \times f_{y,flange} \times h_{flange}$$

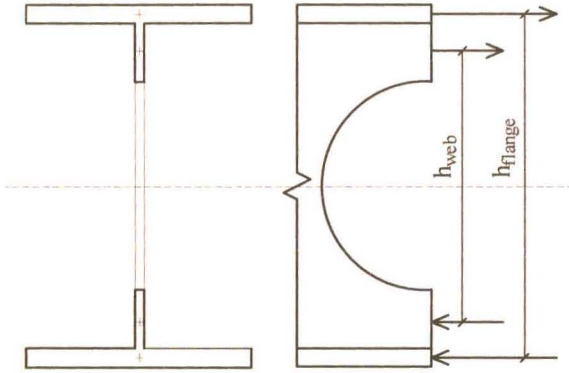


Figure 3.9 : Forces and lever arms

A_{web} and A_{flange} are the areas of the web and flange of one tee section respectively.

The formulae for shear and web post flexure and buckling remained unchanged, since only the web yield stress was involved.

(e) Vierendeel bending

The moment resistance of the tee section alone was required in calculating the Vierendeel resistance. This involved finding the centroid of the area of the tee section. Where the original equation used areas, the adjusted equation is based on forces, as follows:

$$F_{tee} = w_f \times t_f \times f_{y,flange} + t_w \times h_w \times f_{y,web}$$

Centroids for equal areas (Figure 3.10):

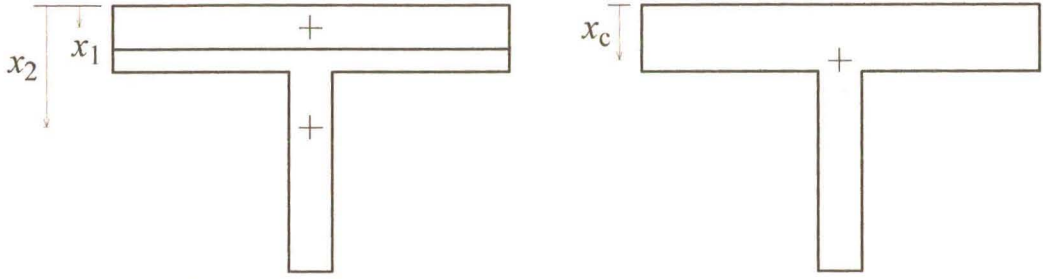


Figure 3.10 : Centroids for equal areas

$$\text{Flange: } x_1 = \frac{F_{tee}}{2 \times w_f \times f_{y,flange}}$$

Part flange and web:

$$x_2 = \frac{\frac{1}{2} w_f \times (t_f - x_1)^2 \times f_{y,flange} + t_w \times h_w \times (\frac{1}{2} h_w + t_f - x_1) \times f_{y,web}}{F_{tee} / 2}$$

$$\text{Whole tee section: } x_c = \frac{\frac{1}{2} w_f \times t_f^2 \times f_{y,flange} + t_w \times h_w \times (\frac{1}{2} h_w + t_f) \times f_{y,web}}{F_{tee}}$$

$$M_p = \frac{F_{tee}}{2} \times \left(x_2 + \frac{x_1}{2} \right)$$

The forces acting on a section are calculated using the equations:

$$P_o = T \cos 25 - \frac{V}{2} \sin 25$$

$$M = T(x_c' - x_c) + \frac{V}{2} (H - x_c) \tan 25$$

and substituted into Eq. 3-1.

The entire analysis was done on a spreadsheet. This permitted the imposed load to be altered manually until one of the checks failed.

Limitations

Although this method is only valid for simply supported beams, there are no limitations on the type of loading. The only requirements are the values of the shear forces and bending moments at the centres of the openings.

Results

The output from the SCI analysis was failure load and mode. Vierendeel failure was predicted in all the beams at the opening with the highest combined shear and moment, i.e. at the central opening for beams loaded at the midpoint, and at the openings adjacent to the loads on the support sides for beams loaded at the third points.

The failure loads calculated using the SCI method are compared to the experimental values in Figure 3.11:

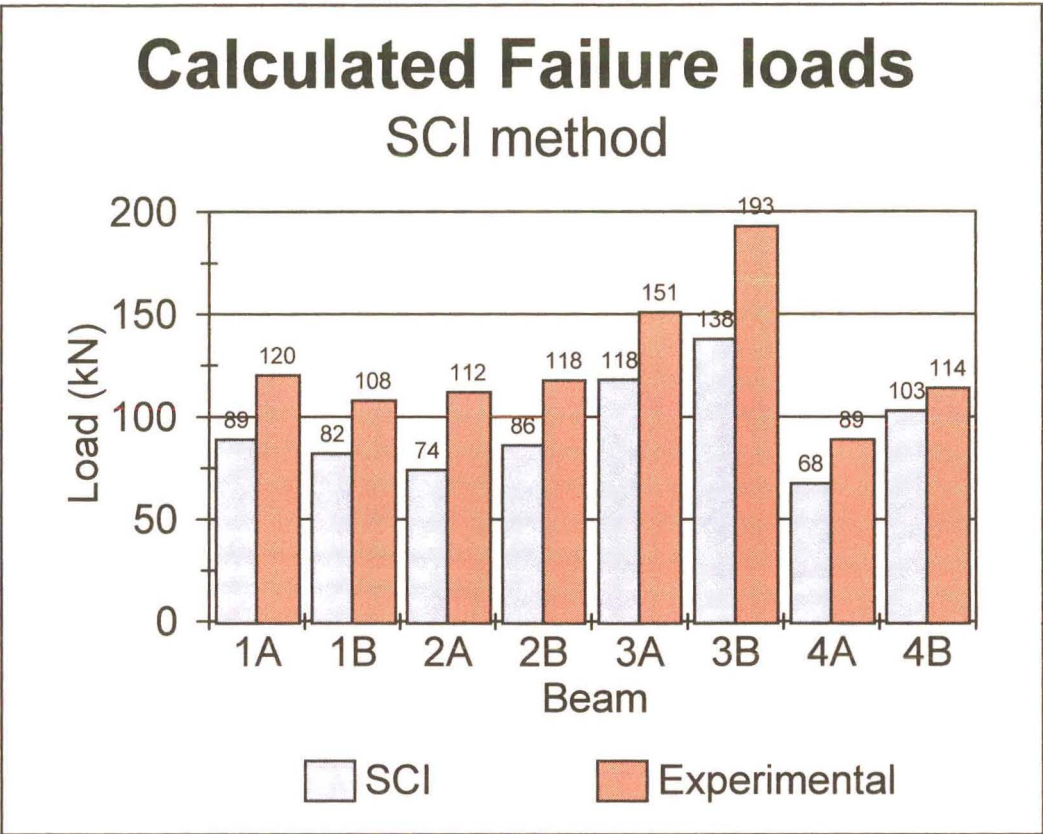


Figure 3.11 : Theoretical and experimental failure loads, SCI method

The SCI method is seen to be very conservative. The exception is Beam 4B, but it is likely that this beam did not reach its full plastic load before it failed in buckling.

The ratios of the theoretical failure load and the experimental values are given in Table 3.2:

Table 3.2 : Failure load ratios, SCI method

Beam	Failure load ratio
1A	0,74
1B	0,76
2A	0,66
2B	0,73
3A	0,78
3B	0,72
4A	0,76
4B	0,90
Mean	0,76

3.4 Proposed new methods of analysis

3.4.1 Plastic analysis

The plastic analysis models were developed on the assumption that the shear and primary moment combine with the Vierendeel moment to produce plastic hinges at four points around the opening. Whereas the plastic hinges in castellated beams will evidently occur at the corners of the opening, the positions of the hinges in cellular beams are not so easily predicted.

Two alternative approaches to the problem were developed, viz.
 a computer program
 a spreadsheet

3.4.1.1 The Computer Program

The computer program is based on the Vierendeel failure mechanism.

The load case assumed for the computer program is a simply supported beam loaded so as to induce a reaction V at the support. (Figure 3.12) This reaction produces the moments and shear forces used in the analysis; only openings between the load and the support are considered.

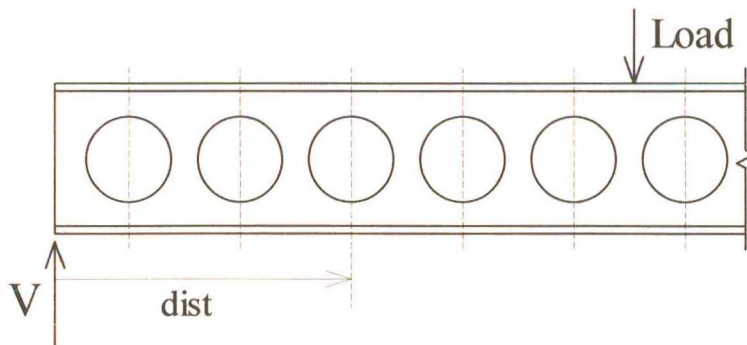


Figure 3.12 : Load case considered for computer program

Theory

The Vierendeel mechanism involves the interaction of three stresses (Figure 3.4):

(a) Primary Shear

The assumption was that the shear stress (γ) and bending stress (f_x) interact according to von Mises' yield criterion ¹¹ which states:

$$f_y^2 = f_x^2 + 3\gamma^2$$

where f_y is the yield stress.

(b) Primary Bending

It is further assumed that the tees are sufficiently ductile to ensure that the primary bending and Vierendeel bending stresses are distributed so as to maximise the section's bending resistance. (Figure 3.4) Referring to the load case of Figure 3.12, the left hand side of an opening will have a lower primary bending moment than the right hand side. The left hand side is thus the *low moment side* (section 1-1 of Figure 3.4) and the right hand side the *high moment side* (section 2-2 of Figure 3.4). On the low moment side of the tee section the primary bending stress block is located at the outer fibres of the tee; on the high moment side the primary bending stress block is located at the inner fibres of the tee. The primary moment stresses effectively prestress the beam so as to maximise its resistance to the Vierendeel bending stresses.

(c) Vierendeel Bending

Only the top tee section will be considered, since the bottom tee section differs only in that the compression and tensile stresses are reversed.

On the low moment side of the tee the Vierendeel bending induces tension at the top of the tee and compression at the bottom. Conversely on the high moment side the Vierendeel bending induces compression at the top of the tee and tension at the bottom. Since these sections are effectively prestressed by the primary moment, the Vierendeel stress can reach twice the yield stress.

Application of the Theory

Vierendeel mechanism

Each of the three components of the Vierendeel mechanism is discussed separately.

(a) Primary Shear

Because the shear is resisted by the web which has $area = h_t t_w$ and hence a shear stress:

$$\gamma = \frac{V}{h_t t_w}$$

$$\text{and } f_y^2 = f_x^2 + 3\gamma^2$$

the allowable residual bending stress in the web is:

$$f_w = \sqrt{f_{y,web}^2 - 3\gamma^2}$$

The stress f_w is thus the effective yield stress in the web.

(b) Primary Bending

The primary bending stresses are calculated at the hinge points.

Low moment side of the opening

The moment to be resisted is : $M = V \times \left(dist - \frac{c}{2} \right)$

The stress diagram for the primary bending moment was as shown in Figure 3.4. The distance x from the top of the tee section to the bottom of the stress block (Figure 3.13) was calculated as follows:

A preliminary value for x was calculated assuming that $x < t_f$, where t_f is the thickness of the flange.

$$\begin{aligned}
 M &= F y \\
 F &= (f_{y_f})(w_f)(x) \\
 y &= \frac{1}{2}(H - x) \\
 \therefore M &= (f_{y_f} w_f x) \frac{1}{2} (H - x) \\
 \therefore 2M &= f_{y_f} w_f H x - f_{y_f} w_f x^2 \\
 \therefore 0 &= f_{y_f} w_f x^2 - f_{y_f} w_f H x + 2M
 \end{aligned}$$

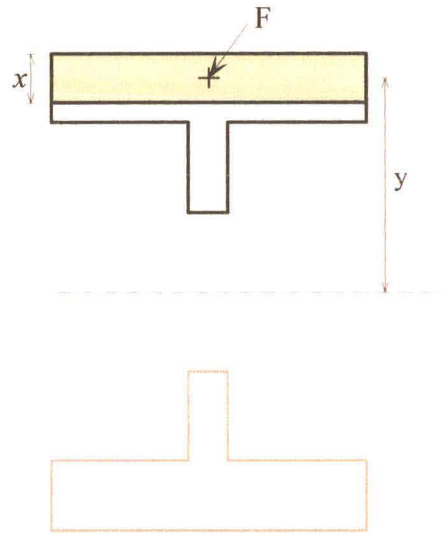


Figure 3.13 : Primary bending, low moment side

x was calculated using the formula : $x = \frac{-b \pm \sqrt{b^2 - 4ac}}{2a}$

$$\begin{aligned}
 \text{where } a &= f_{y_f} w_f \\
 b &= -f_{y_f} w_f H \\
 c &= 2M
 \end{aligned}$$

The smallest positive root was taken as x .

It was necessary to check that the stress block fell within the flange; if it did not, the depth x' of the web involved in resisting the primary moment had to be determined. (Figure 3.14)

$$\begin{aligned}
 M &= F_1 y_1 + F_2 y_2 \\
 F_1 &= f_{y_f} w_f t_f \\
 y_1 &= \frac{1}{2}(H - t_f) \\
 F_2 &= f_w t_w x' \\
 y_2 &= \frac{1}{2}(H - x') - t_f
 \end{aligned}$$

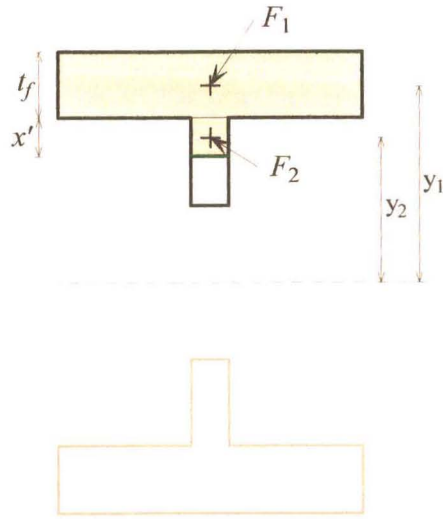


Figure 3.14 : Primary bending, $x > t_f$

$$\therefore (f_w t_w) x'^2 - (f_w t_w) (H - 2t_f) x' + 2(M - F_1 y_1) = 0$$

which is in the form $ax^2 + bx + c = 0$ and is solved as such to find x' , whence

$$x = t_f + x'$$

High moment side of the opening

The moment to be resisted is : $M = V \times \left(dist + \frac{c}{2} \right)$

The stress diagram for the primary bending moment was as shown in Figure 3.4. The distance x from the bottom of the tee section to the top of the stress block (Figure 3.15) was calculated as follows:

$$\begin{aligned}
 M &= F y \\
 F &= f_w t_w x \\
 y &= \frac{1}{2} (h_s + x) \\
 \therefore f_w t_w x^2 + f_w t_w h_s x - 2M &= 0
 \end{aligned}$$

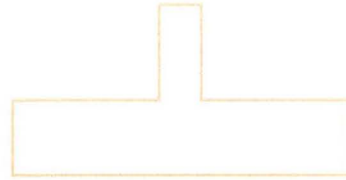
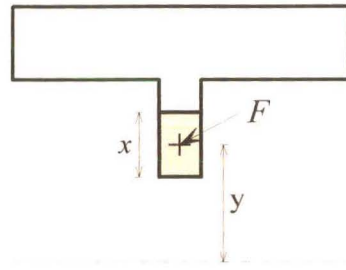


Figure 3.15 : Primary bending, high moment side

Having calculated x , it was necessary to check that the stress block fell within the web; if it did not, the depth x' of the flange involved in resisting the primary moment had to be determined. (Figure 3.16)

$$\begin{aligned}
 M &= F_1 y_1 + F_2 y_2 \\
 F_1 &= f_{y_f} w_f x' \\
 y_1 &= h_w + \frac{h_s + x'}{2} \\
 F_2 &= f_w h_w t_w \\
 y_2 &= \frac{h_s + h_w}{2}
 \end{aligned}$$

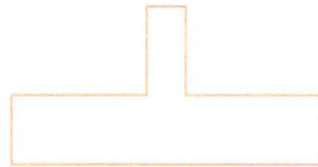
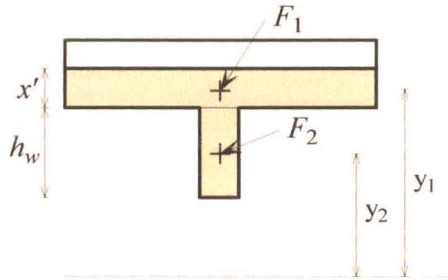


Figure 3.16 : Primary bending, $x > h_w$

$$\therefore f_{y_f} w_f x'^2 + f_{y_f} w_f (h_s + 2h_w) x' - 2(M - F_2 y_2) = 0$$

This quadratic was solved for x' whence $x = h_w + x'$.

(c) Vierendeel Bending

The Vierendeel moment to be resisted is :

$M = V c$ in total, but for the top tee only,

$$M = \frac{1}{2} V c$$

The general way in which the force, V , is derived from the Vierendeel bending resistance of the tee section given by:

$$M = \frac{Vc}{2} = F_1 y_1 + F_2 y_2 + + F_n y_n$$
$$\therefore V = \frac{2}{c} (F_1 y_1 + F_2 y_2 + + F_n y_n)$$

Decision-making chart

Figure 3.17 sets out the decision-making process required to deal with the various stress distributions that can develop in the tees. (Figures 3.13 to 3.16)

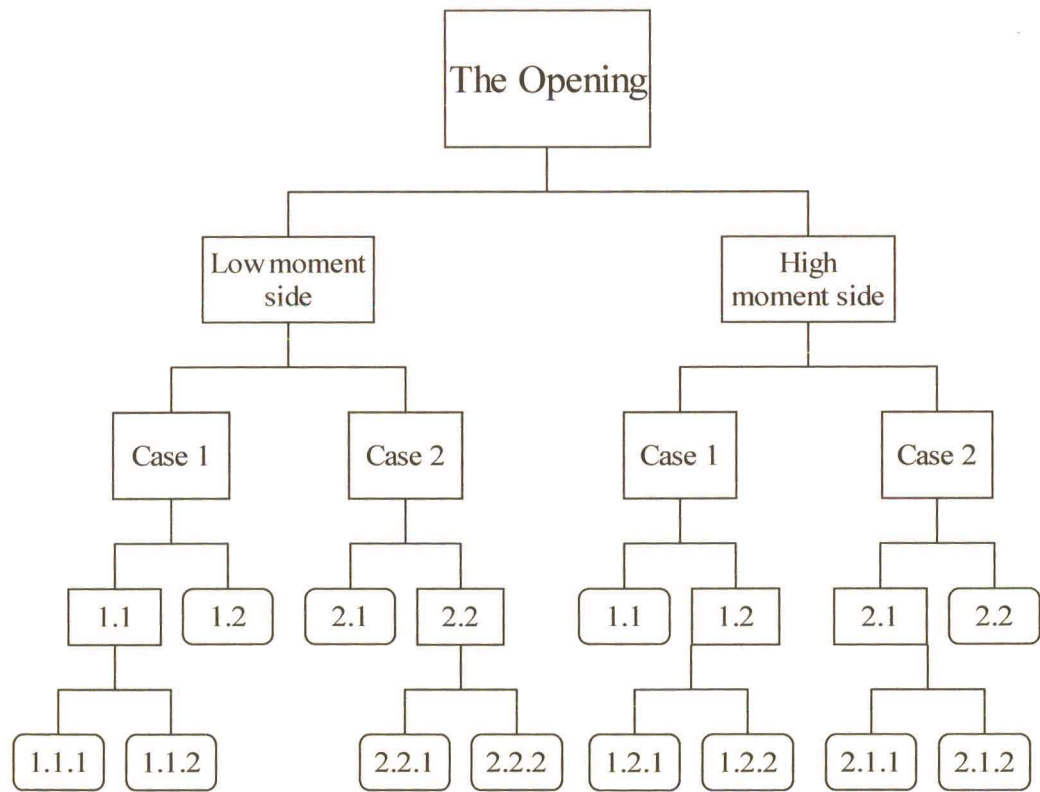


Figure 3.17 : Decision-making chart for Vierendeel stress adjustments

Low moment side of opening

Case 1 : Only Flange stressed by the primary moment (Figure 3.18)

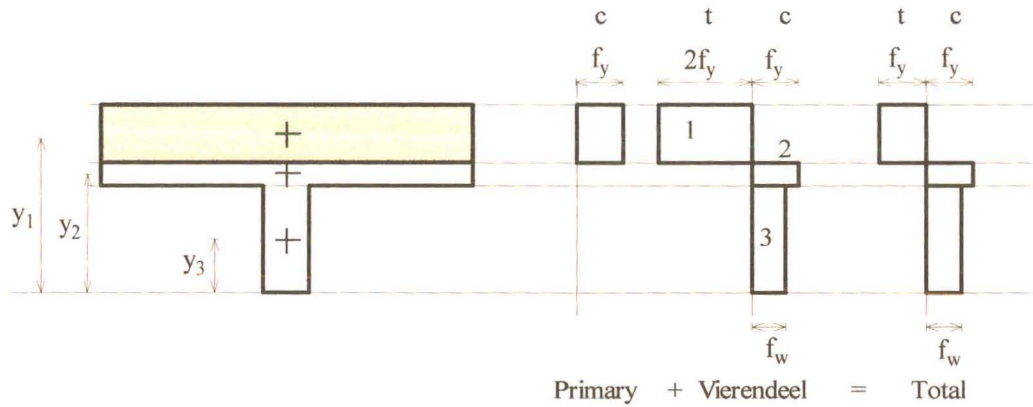


Figure 3.18 : Low moment side, Case 1

$$\begin{aligned}
 (t) \quad F_1 &= 2f_{yf} \times w_f & y_1 &= \frac{x}{2} \\
 (c) \quad F_2 &= f_{yf} (t_f - x) w_f & y_2 &= \frac{x + t_f}{2} \\
 (c) \quad F_3 &= f_w h_w t_w & y_3 &= t_f + \frac{h_w}{2}
 \end{aligned}$$

It is necessary to adjust the forces, F_1, F_2, F_3 so that horizontal equilibrium is maintained, i.e. tension equals compression.

1.1 Tension < Compression (ie: $F_1 < F_2 + F_3$)

In this case, the available compression is in excess of requirements, and F_2 (and where necessary, F_3) becomes partly or wholly tensile. There are two possibilities, viz.

1.1.1 F_2 is large enough to offset the excess compression.

i.e. $F_2 \geq (F_2 + F_3 - F_1)/2$

$\therefore F_2 \geq F_3 - F_1$

In this case F_2 becomes partly or wholly tensile. (Figure 3.19)

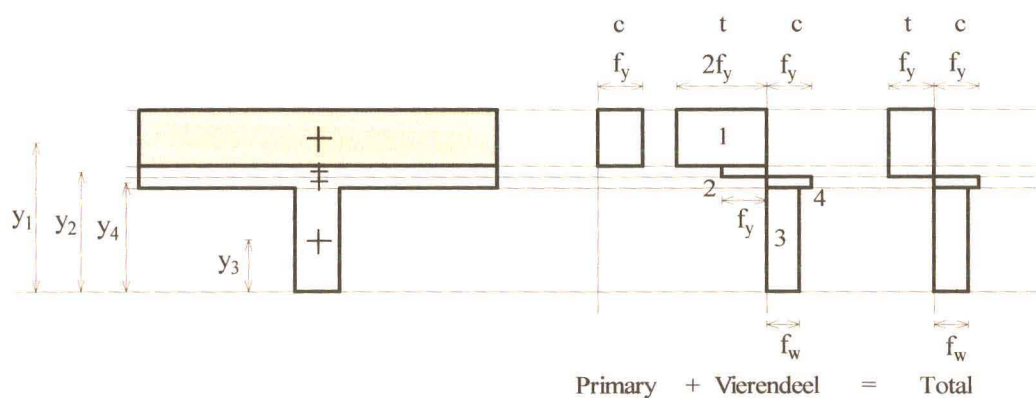


Figure 3.19 : Low moment side, Case 1.1.1

1.1.2 $F_2 < F_3 - F_1$, in which case F_2 becomes wholly tensile, and F_3 partly tensile. (Figure 3.20)

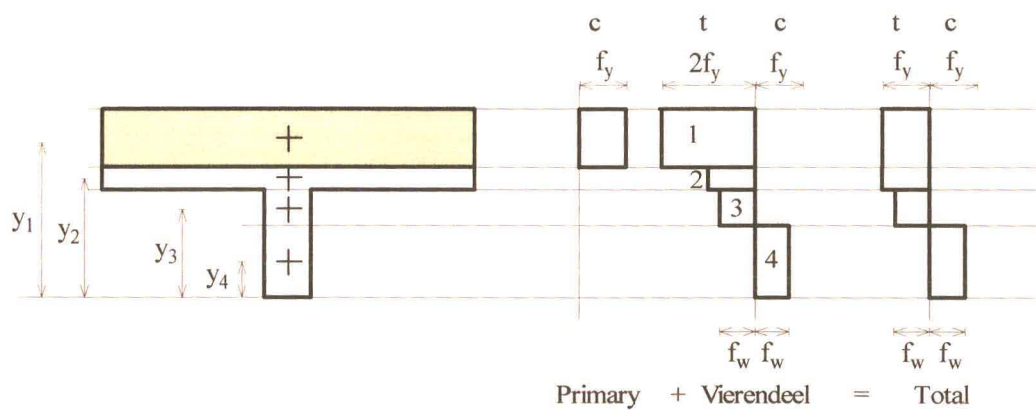


Figure 3.20 : Low moment side, Case 1.1.2

1.2 Tension > Compression (ie: $F_1 > F_2 + F_3$)

In this case, there is insufficient compression available to develop F_1 fully, and this force reduces accordingly. This is effected by reducing the depth of the stress block from the underside of the flange, thus maximising the lever arm. (Figure 3.21)

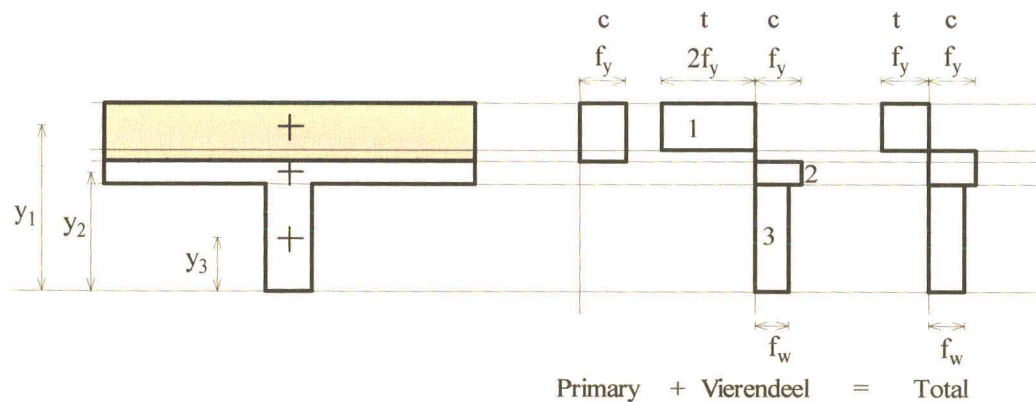


Figure 3.21 : Low moment side, Case 1.1.2

Case 2 : Flange and web stressed by primary moment (Figure 3.22)

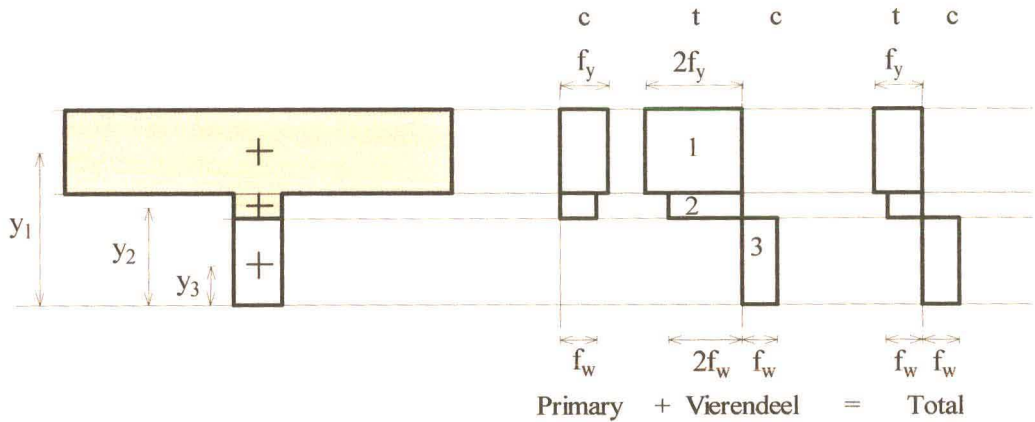


Figure 3.22 : Low moment side, Case 2

$$\begin{aligned}
 (t) \quad F_1 &= 2f_y t_f w_f & y_1 &= \frac{t_f}{2} \\
 (t) \quad F_2 &= 2f_w (x - t_f) t_w & y_2 &= \frac{x + t_f}{2} \\
 (c) \quad F_3 &= f_w (h_t - x) t_w & y_3 &= \frac{x + h_t}{2}
 \end{aligned}$$

It is necessary to adjust the forces, F_1, F_2, F_3 so that horizontal equilibrium is maintained, i.e. tension equals compression.

2.1 Compression > Tension (ie $F_3 > F_1 + F_2$)

In this case, the available compression is in excess of the requirements, and the force F_3 becomes partly tensile. (Figure 3.23)

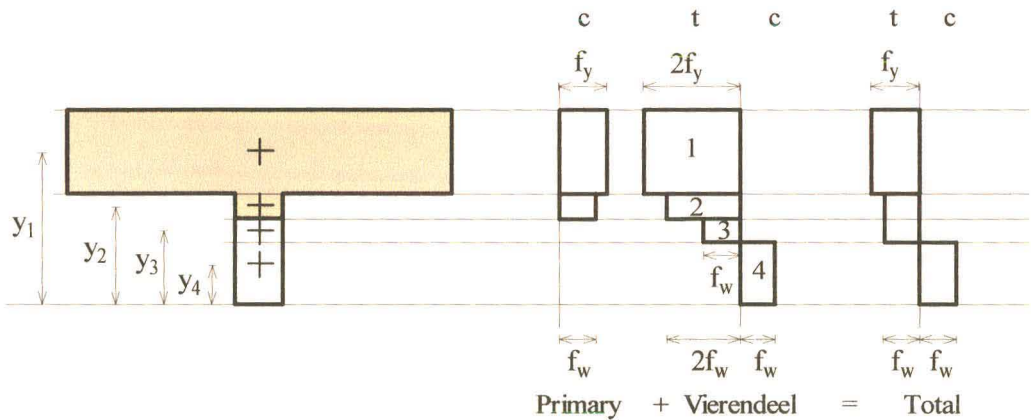


Figure 3.23 : Low moment side, Case 2.1

2.2 Compression < Tension (ie $F_3 < F_1 + F_2$)

In this case, the available tension is in excess of requirements and the value of F_2 (and where necessary, F_1) is reduced accordingly. There are two possibilities, viz.

2.2.1 F_2 is large enough to offset the excess tension.

i.e. $F_2 \geq F_1 + F_2 - F_3$

$\therefore F_3 \geq F_1$

In this case F_2 is reduced accordingly. (Figure 3.24)

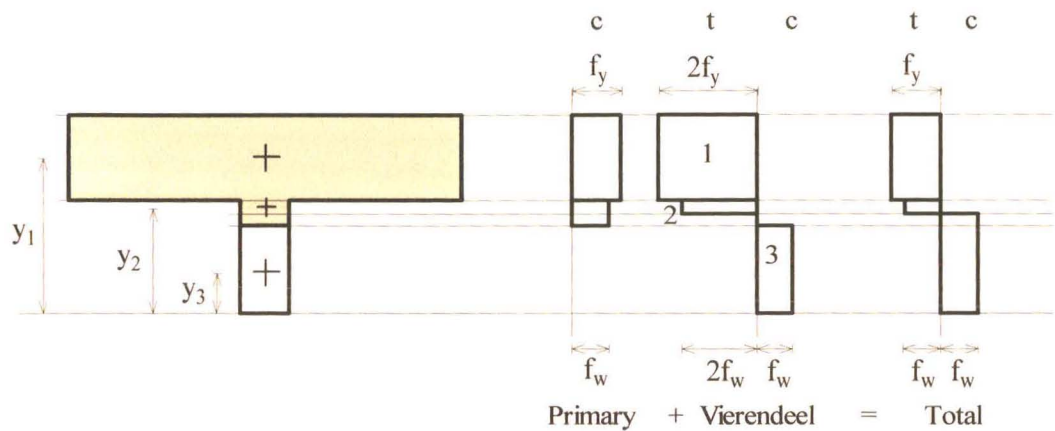


Figure 3.24 : Low moment side, Case 2.2.1

2.2.2 $F_3 < F_1$, in which case F_2 falls away and F_1 is reduced accordingly. (Figure 3.25)

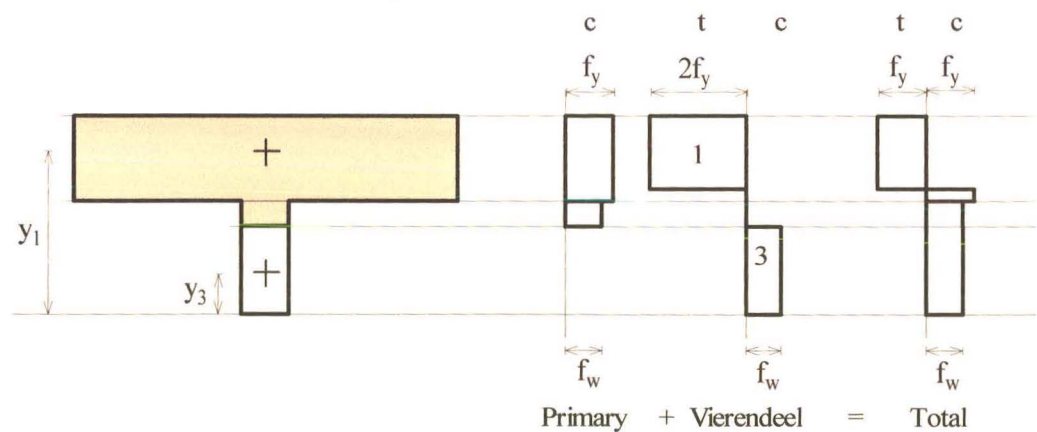


Figure 3.25 : Low moment side, Case 2.2.2

High moment side of the opening:

Case 1 : Only web stressed by primary moment. (Figure 3.26)

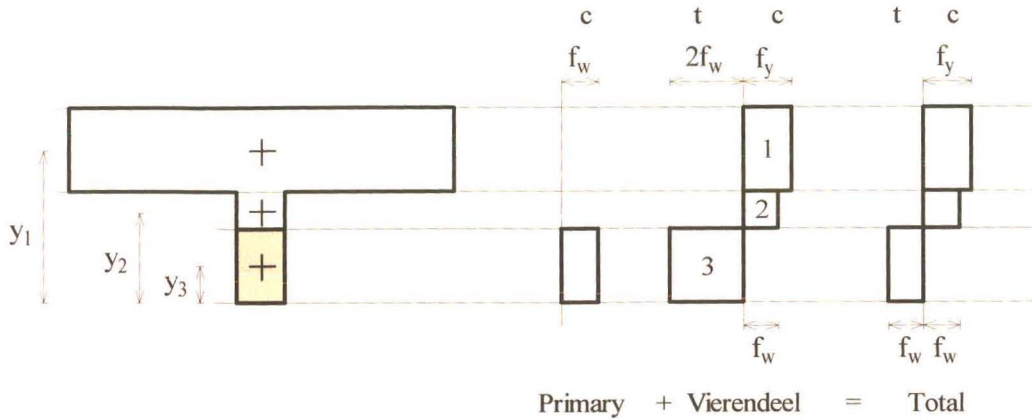


Figure 3.26 : High moment side, Case 1

$$\begin{aligned}
 (c) \quad F_1 &= f_{y_f} t_f w_f & y_1 &= \frac{t_f}{2} \\
 (c) \quad F_2 &= f_w (h_w - x) t_w & y_2 &= t_f + \frac{h_w - x}{2} \\
 (t) \quad F_3 &= 2f_w x t_w & y_3 &= h_t - \frac{x}{2}
 \end{aligned}$$

It is necessary to adjust the forces F_1 , F_2 , F_3 to maintain horizontal equilibrium, i.e. tension equals compression.

1.1 Tension > Compression ($F_3 > F_1 + F_2$)

In this case the available tension is in excess of requirements and the value of F_3 is reduced accordingly. (Figure 3.27)

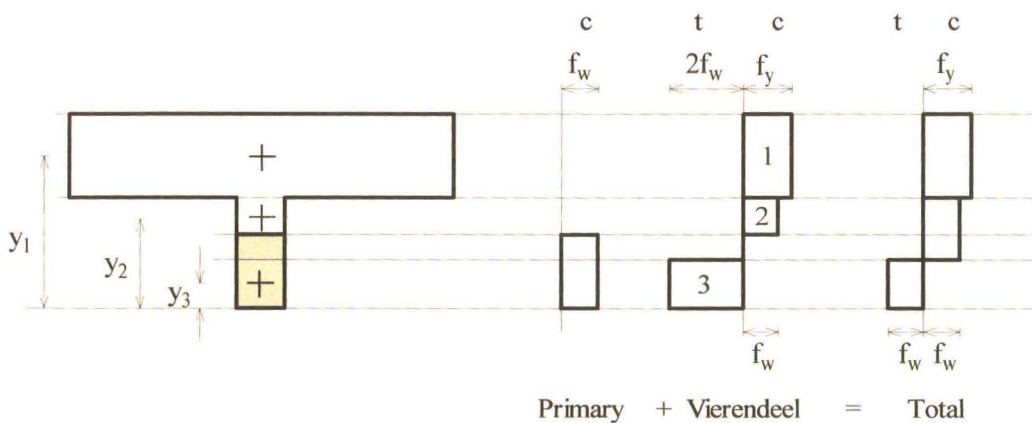


Figure 3.27 : High moment side, Case 1.1

1.2 Tension < Compression ($F_3 < F_1 + F_2$)

In this case, the available compression is in excess of requirements and F_2 (and where necessary F_1) becomes partly or wholly tensile. There are two possibilities, viz.

1.2.1 F_2 is large enough to offset the excess compression.

i.e. $F_2 \geq (F_1 + F_2 - F_3)/2$

$\therefore F_2 \geq F_1 - F_3$

In this case F_2 becomes partly or wholly tensile. (Figure 3.28)

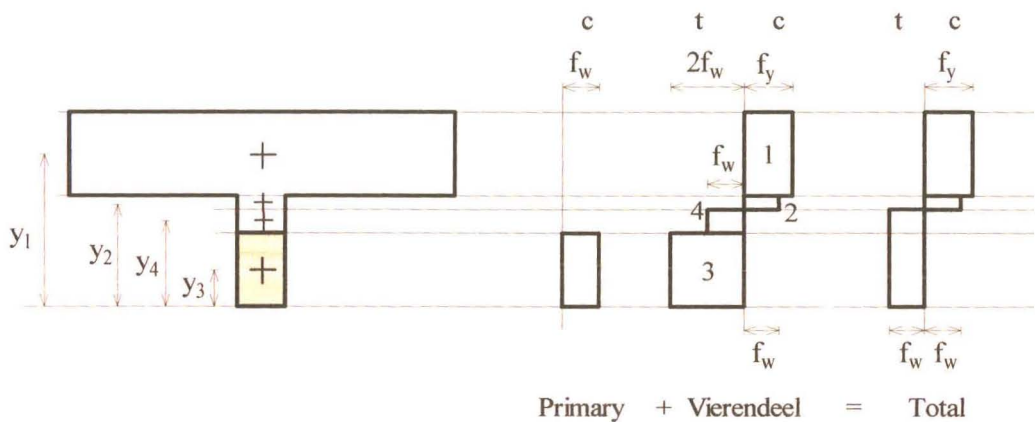


Figure 3.28 : High moment side, Case 1.2.1

1.2.2 $F_2 < F_1 - F_3$, in this case F_2 becomes wholly tensile and F_1 becomes partly tensile. (Figure 3.29)

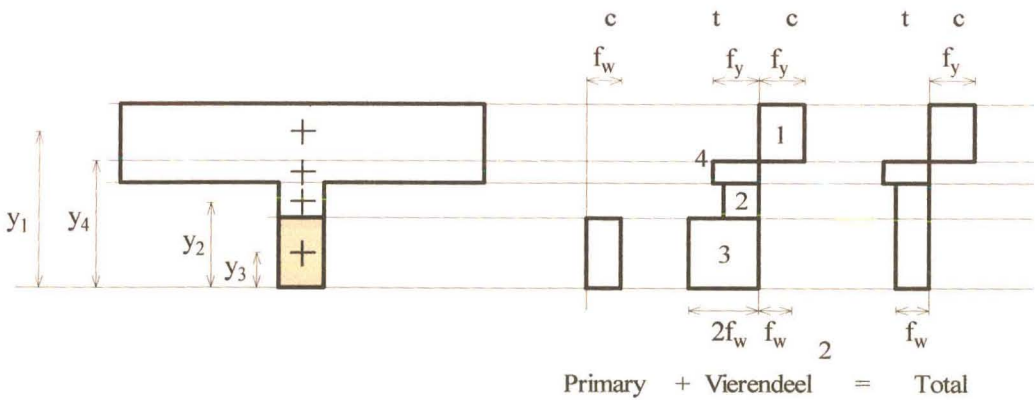


Figure 3.29 : High moment side, Case 1.2.2

Case 2 Web and flange stressed by primary moment. (Figure 3.30)

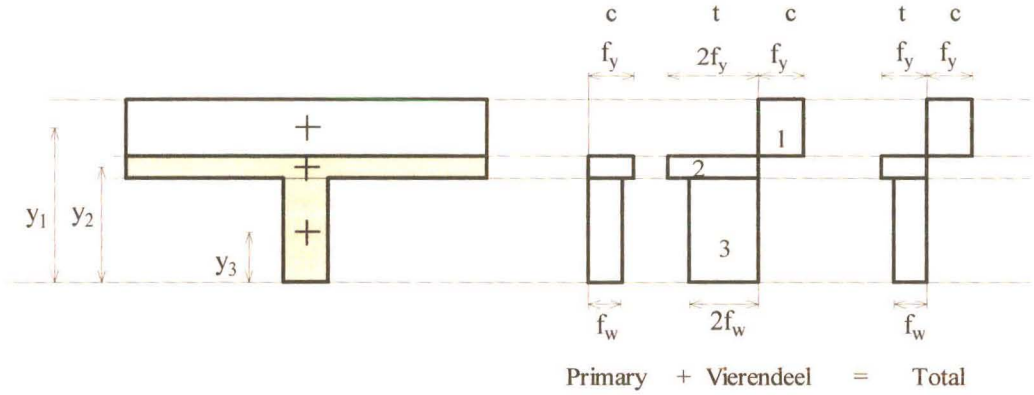


Figure 3.30 : High moment side, Case 2

$$\begin{aligned}
 (c) \quad F_1 &= f_{y_f} (h_t - x) w_f & y_1 &= \frac{h_t - x}{2} \\
 (t) \quad F_2 &= 2f_{y_f} (x - h_w) w_f & y_2 &= h_t - \frac{x + h_w}{2} \\
 (t) \quad F_3 &= 2f_w h_w t_w & y_3 &= h_t - \frac{h_w}{2}
 \end{aligned}$$

It is necessary to adjust the forces F_1 , F_2 , F_3 to maintain horizontal equilibrium, i.e. tension equals compression.

2.1 Compression < Tension ($F_1 < F_2 + F_3$)

The available tension is in excess of the requirements and the value of F_2 (and where necessary F_3) is reduced accordingly. There are two possibilities, viz.

2.1.1 F_2 large enough to offset the excess tension.

i.e. $F_2 \geq (F_2 + F_3 - F_1)$

$\therefore F_1 \geq F_3$

In this case F_2 falls away and, F_3 is reduced accordingly. (Figure 3.31)

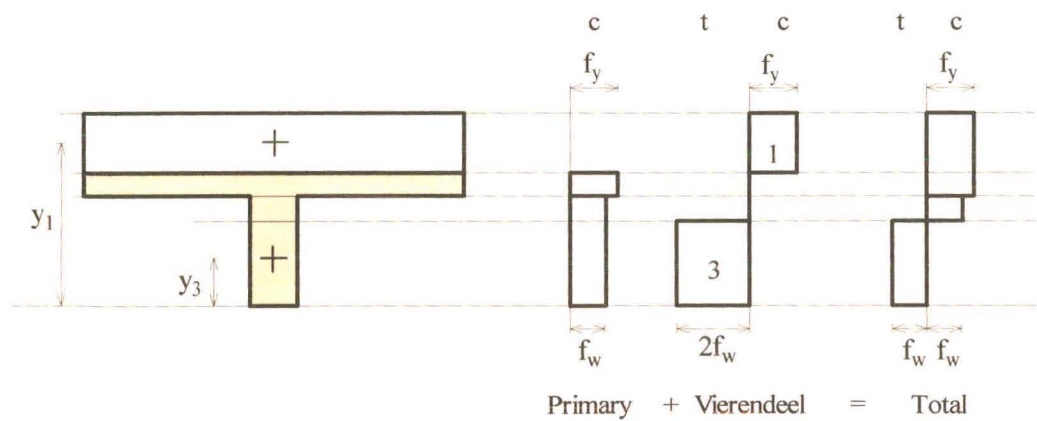


Figure 3.31 : High moment side, Case 2.1.1

2.1.2 $F_1 < F_3$, in which case F_2 is partly reduced. (Figure 3.32)

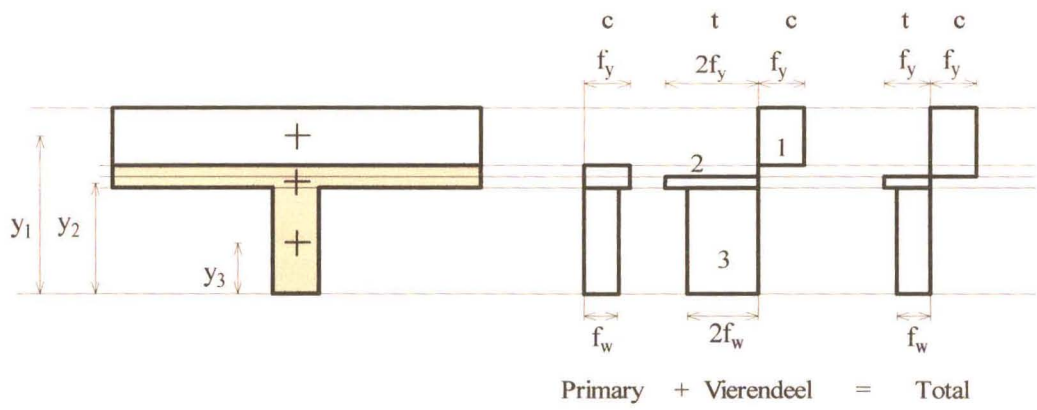


Figure 3.32 : High moment side, Case 2.1.2

2.2 Compression > Tension ($F_1 > F_2 + F_3$)

In this case the available compression is in excess of requirements and F_1 becomes partly tensile. (Figure 3.33)

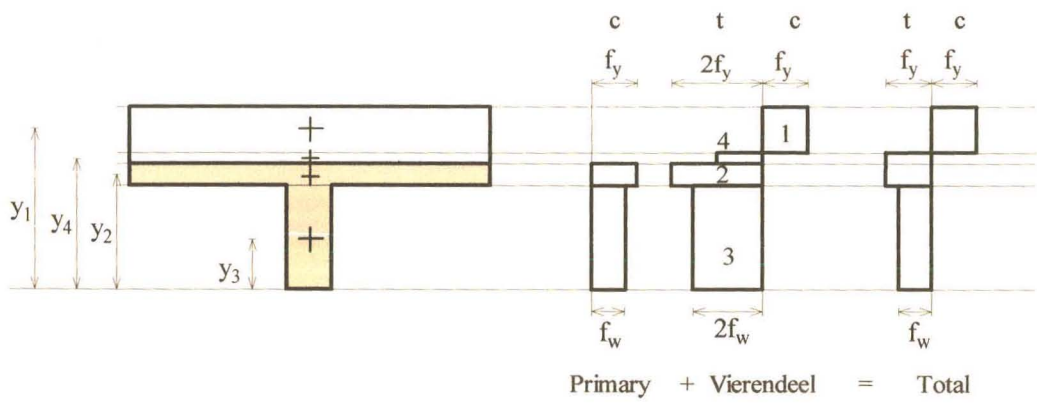


Figure 3.33 : High moment side, Case 2.2

How the Computer Program Works

A section of the program was written for each of the three Vierendeel components, primary shear, primary bending and Vierendeel bending, which were then combined.

The analytical part of the program works in an iterative manner with a root-finding exercise at the end. An initial input force is used to calculate the shear and primary bending stresses in the beam. The residual stress capacity available to resist the Vierendeel bending is then calculated, from which the force required to produce these Vierendeel stresses can be derived. This force is the output force for the current iteration. The input and output forces are then compared. If the output force is smaller than the input force then the input force is incremented and a further iteration is performed. If the output force is larger than the input force then the iterations are halted and the program moves on to the root-finding procedure.

A force equal to the ultimate shear capacity of the tees divided by 100 is used as the initial input force and is incremented by the same value. The upper limit for the input force was taken as the smallest of the following three values:

- (i) Ultimate shear capacity of the beam i.e.: the force the beam can resist assuming the entire stress capacity of the perforated section is used in shear.
- (ii) Ultimate bending capacity of the beam i.e.: the force the beam can resist assuming the entire capacity of the perforated section is used in primary bending.
- (iii) Horizontal web shear capacity.

Iterations are performed until the output force is greater than the input force or until the upper limit has been reached.

The root-finding technique employed was a simple straight line approximation, the abscissa being the input force and the ordinate being the output force. It can be seen from Figure 3.34 that any curve can be closely approximated by assuming a straight-line variation between adjacent points. The intersection of the approximated curve with the line $\text{Output} = \text{Input}$ gave the ultimate force, V .

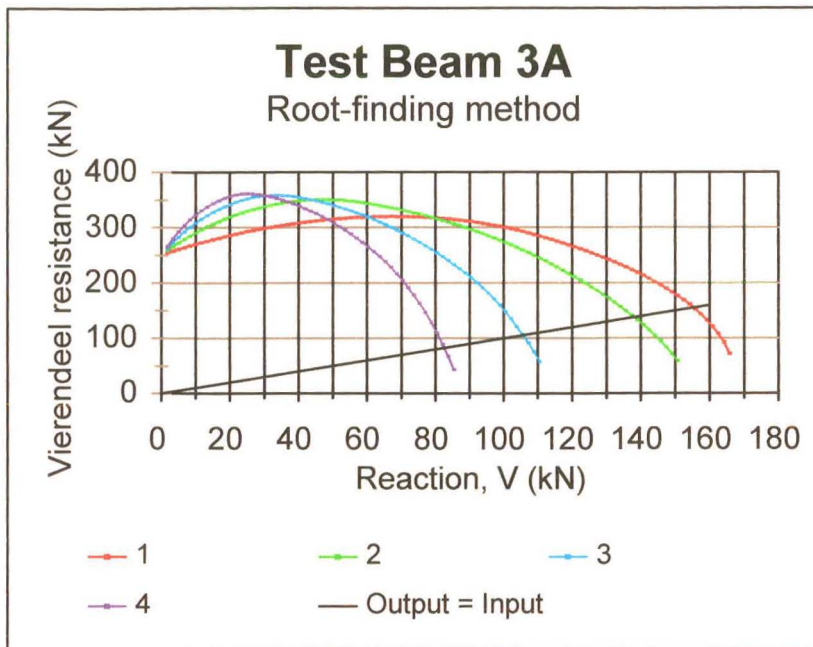


Figure 3.34 : Root-finding for the program analysis

The beam considered for this demonstration was Test Beam 3A. A graph of the output force versus the input force for each iteration was plotted. The four numbered curves in the graph correspond to four openings in the beam. Curve one represents the opening closest to the end of the beam with the successive openings being progressively further away from the end of the beam. The line labelled Output = Input is the line along which the output force is equal to the input force. The position where the Output = Input line intersects with a curve is a possible solution for the load at which a Vierendeel mechanism could form in the corresponding opening. The actual solution occurs at the intersection point closest to the origin, as this is the smallest force and hence the force at which the beam will fail.

The computer program was used to develop the design charts referred to in section 3.4.1.3. The theoretical failure loads for the test beams are given in that section.

3.4.1.2 The Spreadsheet

Theory

The spreadsheet uses the same theory as the program, with one adjustment. In the computer program the circular opening is approximated as an equivalent rectangle with a width of 0,3 times the diameter. The corners of the rectangle are assumed to be the critical positions where plastic hinges form and failure takes place. In the spreadsheet, no assumptions were made about the equivalent rectangle width. The resistances of the tees to Vierendeel bending at various positions across the opening (Figure 3.35) were calculated and the critical position was that giving the minimum ultimate load V.

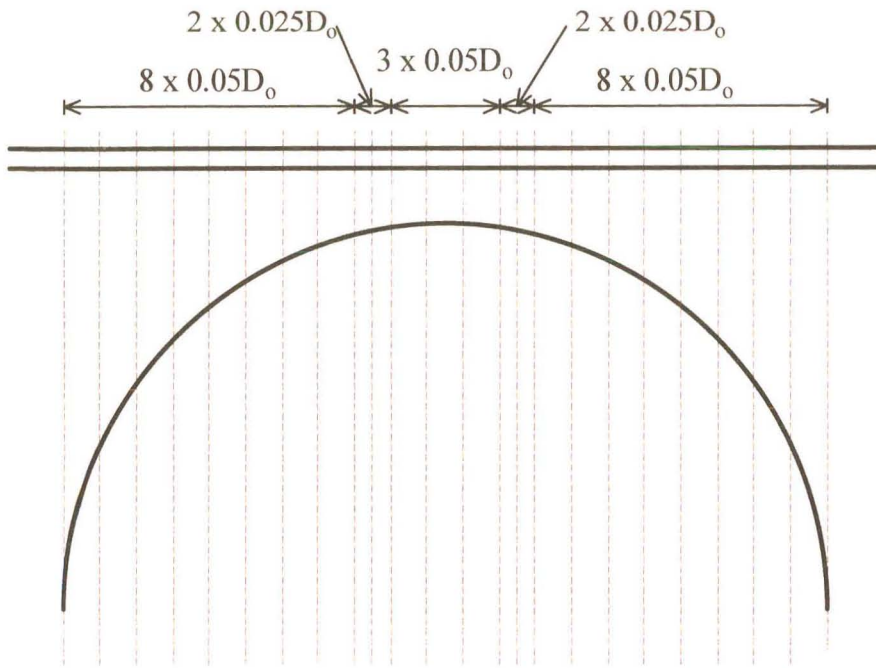


Figure 3.35 : Positions considered for failure with spreadsheet.

Application of the Theory

The general method used in the spreadsheet is the same as that for the program. The reaction force, V , produces a primary moment and shear in the tee section. Stresses in the tee caused by these primary forces are calculated. The remaining stress capacity of the tee is determined and from this the Vierendeel moment which can be resisted is calculated. The reaction needed to produce this Vierendeel moment is calculated and compared with the initial reaction.

Calculations of the moments and stresses are carried out using stress blocks, forces, and lever arms in the same way as the program, except that the calculations are carried out for all positions shown in Figure 3.35.

An advantage of using a spreadsheet is that the applicable case, force and lever arm values can be seen and checked. An applied load is entered, from which the reaction is determined. The Vierendeel moment which can be resisted by the section is calculated and the applied load which would cause this moment is found for each position across the opening. The built-in “solver” function was used to determine the force at which the applied load was equal to the Vierendeel load. The “solver” alters the applied load until it equals the minimum Vierendeel load. This load is taken as the failure load for Vierendeel bending, as represented graphically in Figure 3.36.

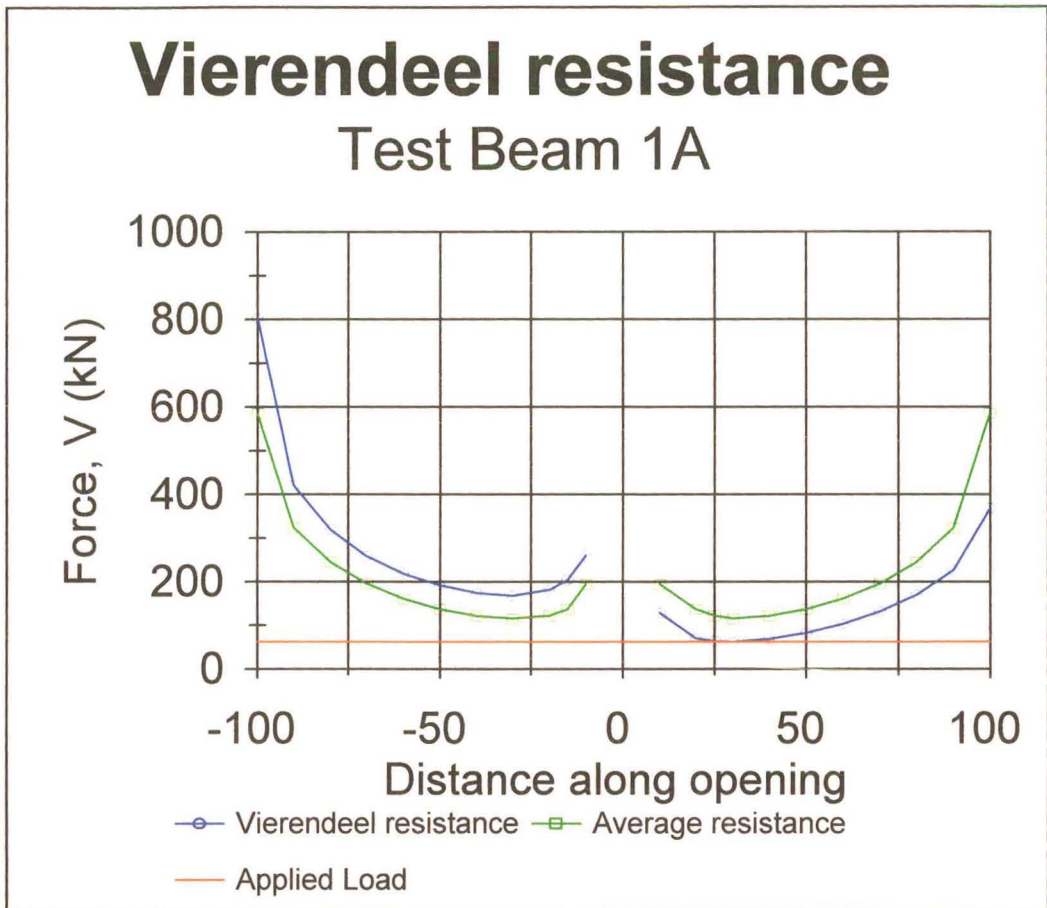


Figure 3.36 : Cellular beam spreadsheet graph

The straight line in the figure is the applied load, which is constant across the opening; the curves represent the Vierendeel load that can be resisted by each side of the opening (where the left hand and right hand curve represent respectively the low moment and the high moment side of the opening).

The curves labeled “Vierendeel resistance” represent the individual resistances of each side of the opening, while the curves labeled “Average resistance” give the average resistance of both sides of the opening. (The difference between the results from the separate curves and those from the average curves are discussed further under “Results”.)

When the Vierendeel force curve touches the applied load straight line, the section is at its maximum stress capacity and failure will occur. The position across the opening at which the curves touch is the position at which the plastic hinge will occur. This can be seen clearly from Figure 3.37, which was plotted for a castellated beam.

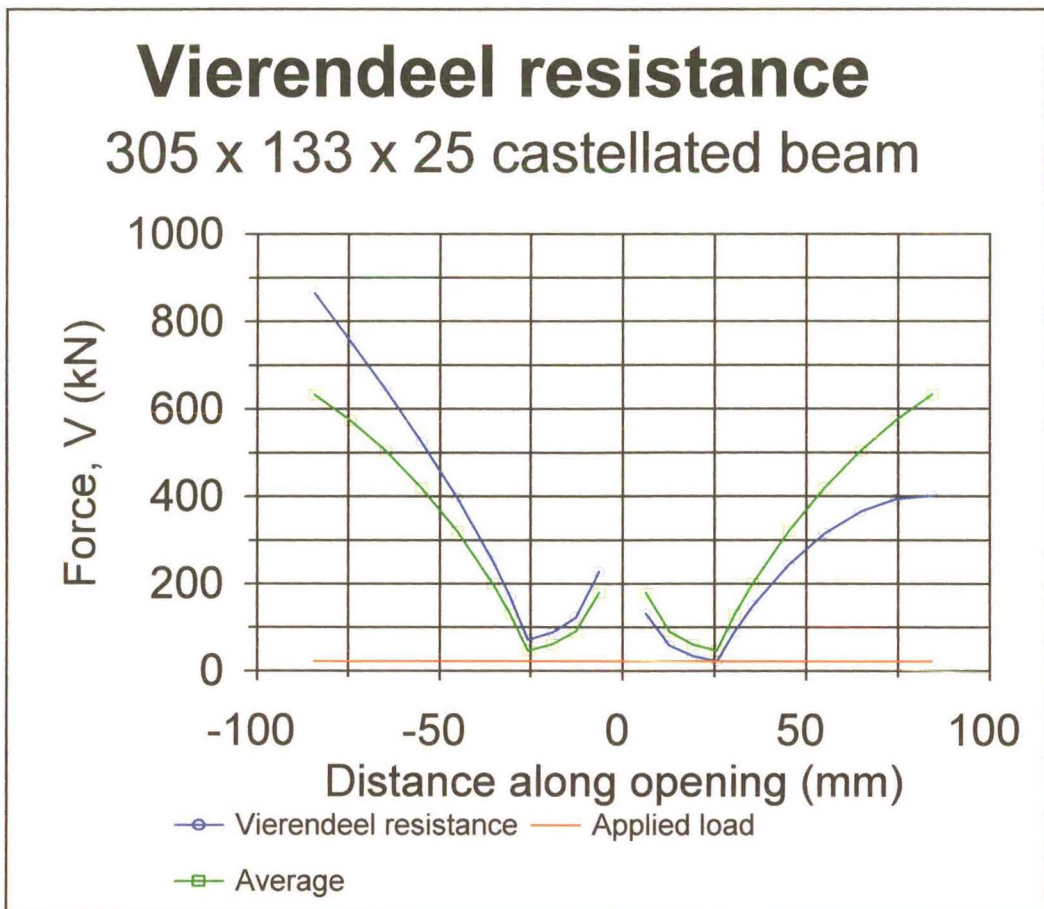


Figure 3.37 : Castellated beam spreadsheet graph

The point in the Vierendeel curve where the graph changes direction corresponds to the position of the corner of the hexagonal opening.

Figures 3.36 and 3.37 underline the relative difficulty in determining the position of the plastic hinge in cellular beams.

The spreadsheet can be modified to model any opening shape as long as the relationship between the distance along the opening and the height of the opening is known.

As with the computer program, checks are carried out for horizontal shear failure of the web posts, primary bending and vertical shear failure. Beams loaded at the third points are checked for failure in pure bending in the constant moment, zero shear zone in the middle of the beam.

Limitations

The spreadsheet design is restricted to the two loading systems applied to the test beams, viz.

- (i) a beam carrying a concentrated load at midspan
- (ii) a beam carrying two equal concentrated loads placed symmetrically about the midspan.

Results

The output from the spreadsheet is the failure load and mode. The spreadsheet has two options for finding the failure load, viz. solving for the minimum load or the average load.

The minimum load is the load at which the Vierendeel resistance for one side of the opening equals the applied load, i.e. when the curve “Vierendeel resistance” curve touches the applied load straight line. (Figure 3.36) This typically happens on the high moment side of the opening, indicating that yielding first occurs on that side.

The average load solution simply takes the average Vierendeel resistances from the high and the low moment sides and determines when this equals the applied load. This assumes some redistribution of stress which is likely to occur in practice. The average value was taken as the failure load for the plastic vierendeel spreadsheet method.

The percentage difference between the minimum value and the average value for all the beams was small and varied between 0,6% and 2,2 %. (These comments do not apply to the beams loaded at the third points, since they were predicted to fail in pure bending in the central third of the span.)

For all beams loaded at the midspan, Vierendeel failure was predicted at the openings either side of the load, viz. the openings subject to maximum combined shear and moment. The failure loads from the spreadsheet are compared with the experimental values in Figure 3.38:

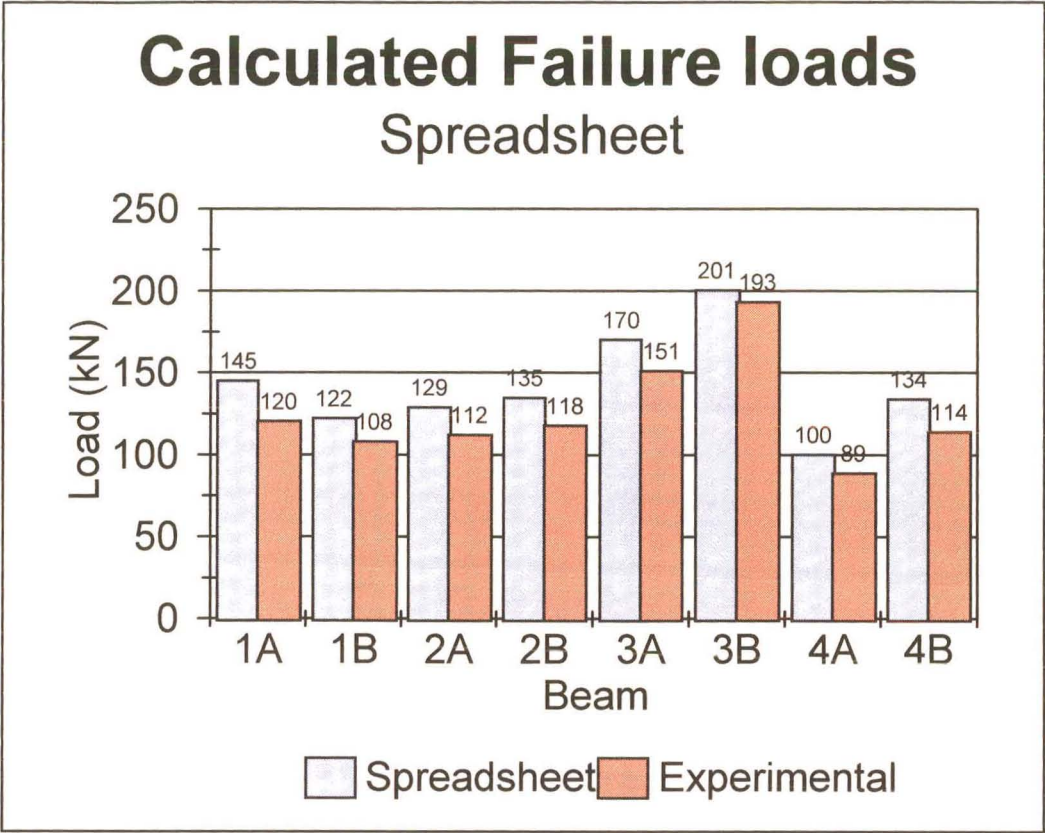


Figure 3.38 : Calculated and experimental failure loads, spreadsheet

The spreadsheet values are all slightly higher than the experimental values. The ratios of theoretical values to experimental values are given in Table 3.3:

Table 3.3 : Failure load ratios, Spreadsheet

Beam	Failure load ratio
1A	1,21
1B	1,13
2A	1,15
2B	1,14
3A	1,13
3B	1,04
4A	1,13
4B	1,18
Mean	1,14

It is evident that the spreadsheet approach gives results that, though unconservative are sufficiently accurate for practical design.

3.4.1.3 Design charts

Introduction

The computer program analysis is confined to the load case illustrated in Figure 3.12. This is a rather limited scenario and will not cover the many load cases that can occur in practice.

If design charts could be developed that related the shear force and bending moment causing plastic failure along a beam, they would cater for a far wider range of load cases than does the program analysis. Thus the ability to create design charts was built into the program. It must be noted that the design charts are a plastic bending analysis tool only, and do not identify problems associated with localised effects of concentrated loads.

Development of Design Charts

The design chart assumes an equivalent rectangular opening width of 0,3 times the opening diameter and a depth equal to the diameter of the opening. (Figure 3.39)

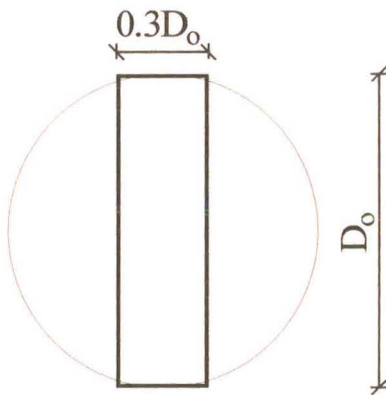


Figure 3.39 : Equivalent rectangular opening for design charts.

The beam properties of any point along the beam are assumed to be those of the minimum section. These are both conservative assumptions.

The design chart checks only for pure bending, Vierendeel mechanism and horizontal shear of the web post. The other possible failure mechanisms are buckling of the web post and lateral-torsional buckling of the entire beam, but these must be considered separately.

A typical design chart is shown in Figure 3.42. The vertical axis relates the actual bending m at a section to the ultimate bending moment that the section can develop M . The horizontal axis relates the actual shear force q in a section to the ultimate shear force that the section can develop Q . The ultimate shear force is that which can be resisted if the entire stress capacity of the perforated section is used to resist shear. Similarly the ultimate bending moment is that which can be resisted if the entire stress capacity of the

perforated section is used to resist bending.

The calculation of the values for the data points used in plotting the chart works in an iterative manner similar to that used in the program analysis. Each design chart has eighty data points. The shear force q was used as the fixed value for each data point and from this the bending moment m that could be resisted was determined. The shear force was incremented by the ultimate shear force divided by eighty for each successive data point. Figure 3.40 is a flow chart showing how the calculations were done.

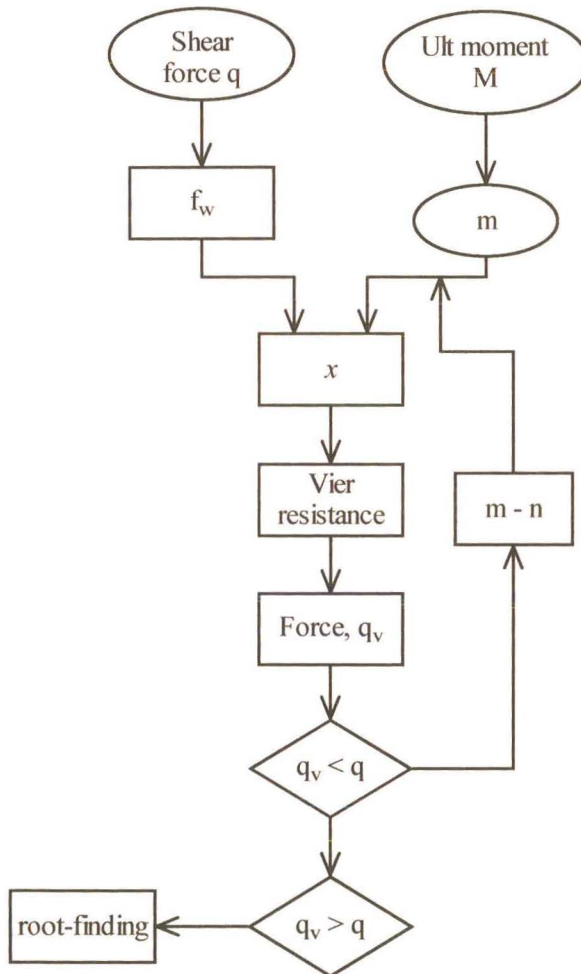


Figure 3.40 : Calculations for design charts

The shear force q was used to calculate the reduction in yield stress. An iterative procedure determined the bending moment that can be resisted. The initial input moment m for the iterations was the ultimate bending moment M . From this the depth of beam, x , resisting the primary bending moment was calculated. The shear force that could be resisted in Vierendeel bending was determined, q_v . If q_v was less than q then the input moment was reduced by a small fixed amount, n , and another iteration carried out. Otherwise the iterations were halted and the program moved on to the root-finding procedure. (Figure 3.41) This cycle was repeated for each of the eighty data points.

Root-finding technique

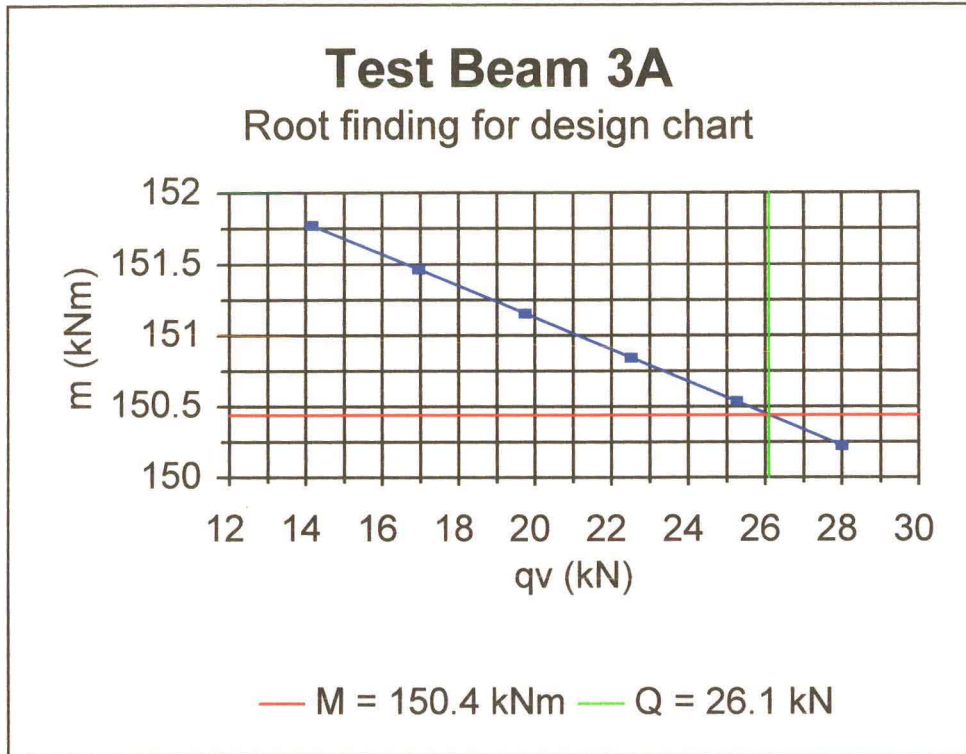


Figure 3.41 : Root-finding for the design charts

The root-finding technique employed here is the same straight line approximation used in the analysis part of the program. The root-finding procedure is carried out for each data point. Figure 3.41 shows a graph which was plotted for the twelfth data point for the design chart for Test Beam 3A.. The shear force for this data point is 26,1kN. The values of the input moment for the iterations, m , are plotted on the abscissa and the values of q_v are the ordinates of the graph. The markers identify the points where q_v was compared to q . It can be clearly seen from the graph that assuming a straight line between the markers is a reasonable approximation to the curve. The values of the abscissa and the ordinate of each of the two points either side of the shear force are known, as well as the value of the shear force, q , and a simple straight line interpolation is carried out to find the moment, m , which corresponds to the shear force, q .

Interpretation of Design Charts (Figure 3.42)

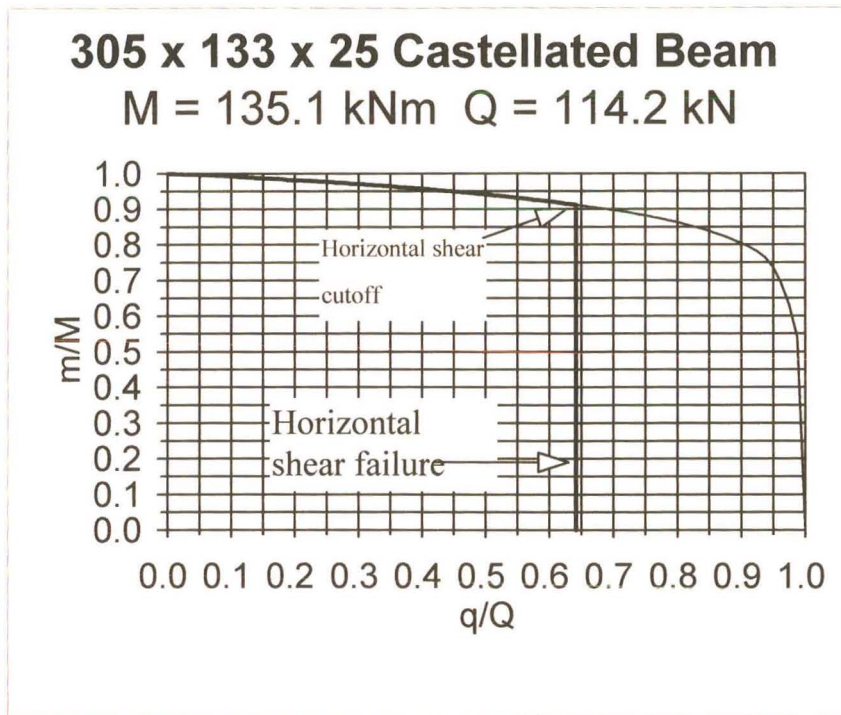


Figure 3.42 : Features of the design chart

The only part of the design chart where the stresses in the beam can safely fall is that enclosed by the line from $m/M = 1$ to the horizontal shear cutoff, and by the horizontal shear failure line.

The dominant force in the beam in the first stage of the design chart, from $m/M = 1$ to the horizontal shear cutoff, is the bending moment. Small changes in the ratio of the shear forces have very little effect on the bending capacity of the beam; however, small changes in the bending moment have large effects on the shear capacity of the beam.

At the horizontal shear cutoff the web post adjacent to the weld will fail due to the horizontal shear induced by the vertical shear force. This failure of the web post causes the two openings on either side of the weld to act as one and fail in Vierendeel bending. Until this double Vierendeel failure has occurred the beam is not considered to have failed, thus the ratio of shear forces in the beam may be greater than indicated by the horizontal shear cutoff. But for design purposes it is undesirable that any part of the beam should fail, thus the horizontal shear cutoff is appropriate.

Use of design charts

The shear forces and bending moments along the beam due to self weight and imposed load were calculated and divided by the ultimate shear force and bending moment. The curve of the ratios of shear forces against the ratios of bending moment was plotted on the design chart. This curve will be referred to as the *beam curve*. The imposed load was adjusted until the beam curve touched the design curve. The corresponding load

was taken as the failure load.

The failure mode can be determined from the design chart by the point at which the beam curve touches the design curve. If the beam curve touches the design curve in the first stage of the design curve from $m/M = 1$ to the horizontal cut off then the failure will be a Vierendeel type of failure with both shear and moment involved. The beam will fail by horizontal shearing of the web post if the beam curve touches the horizontal shear failure line. A pure bending failure will occur if the beam curve touches the design curve at the point where $m/M = 1$. (Figure 3.43)

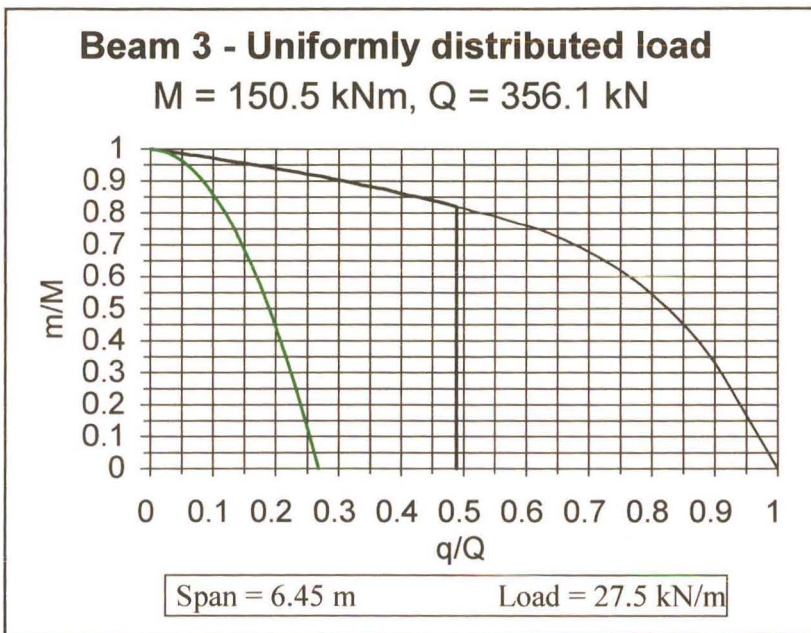


Figure 3.43 : Pure bending failure design chart

The chart thus illustrates the case of a beam failing in pure bending at mid-span. This will generally only occur with a uniformly distributed load.

Results

The design charts for all the test beams are given in Figures 3.44 to 3.51.

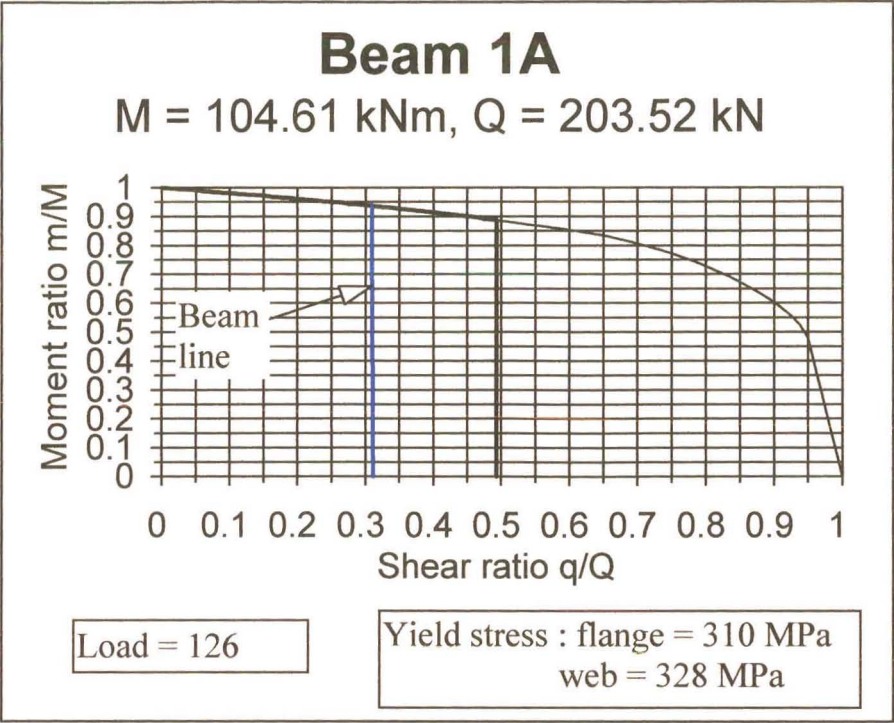


Figure 3.44 : Design chart for Beam 1A, midpoint loading

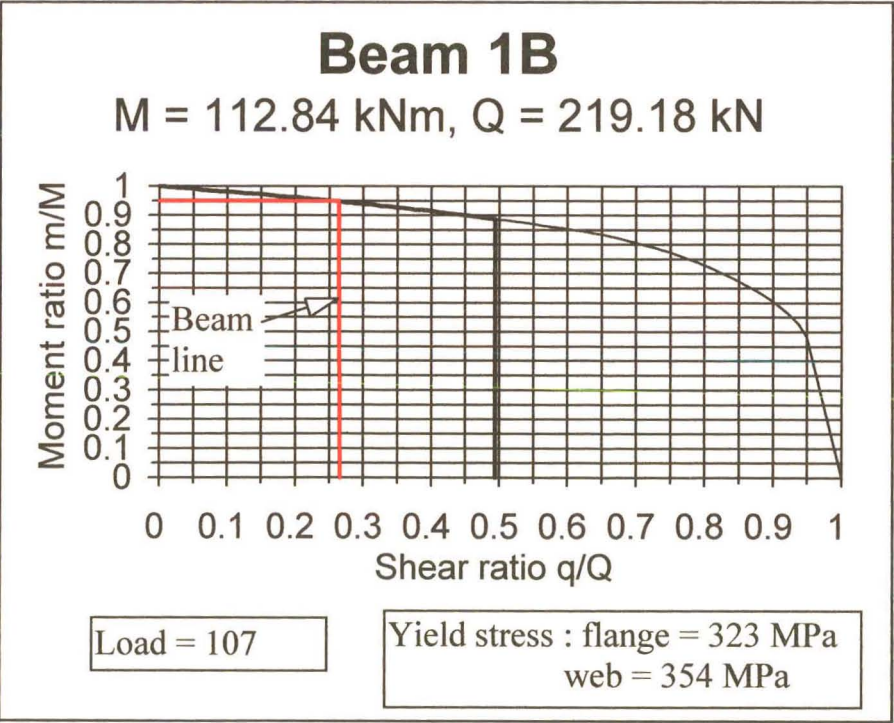


Figure 3.45 : Design chart for Beam 1B, third point loading

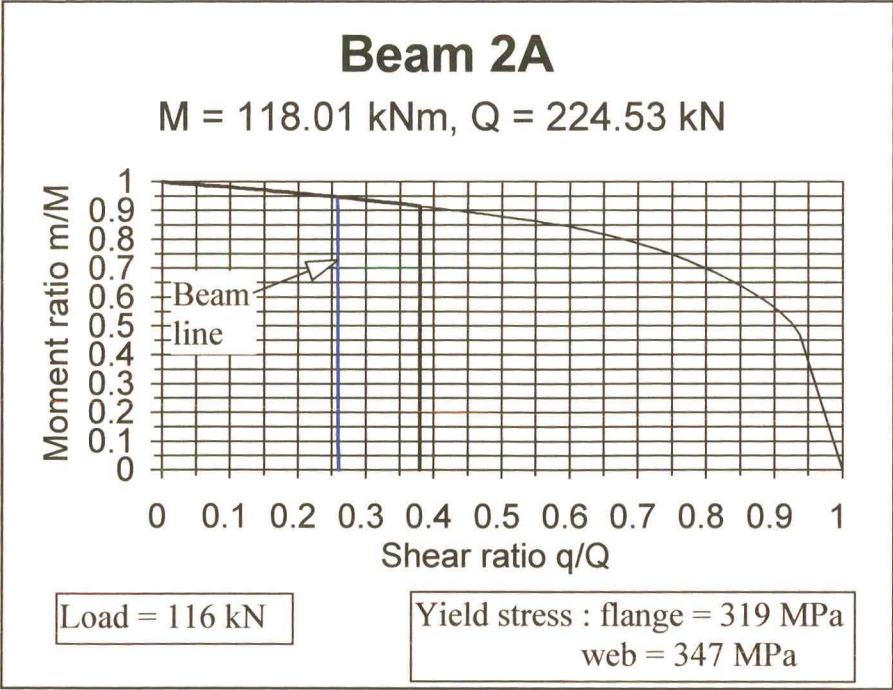


Figure 3.46 : Design chart for Beam 2A, midpoint loading

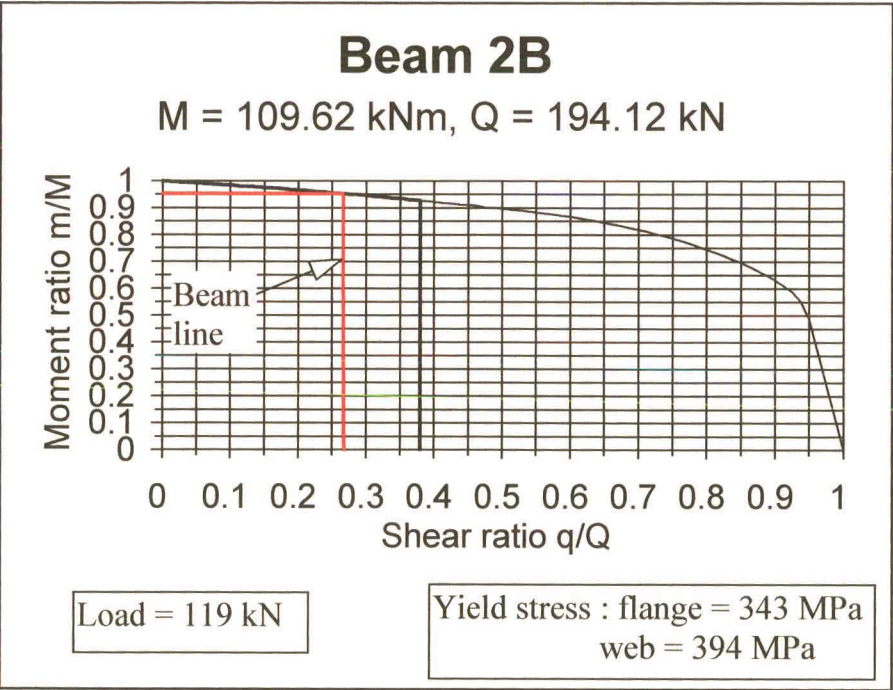


Figure 3.47 : Design chart for Beam 2B, third point loading

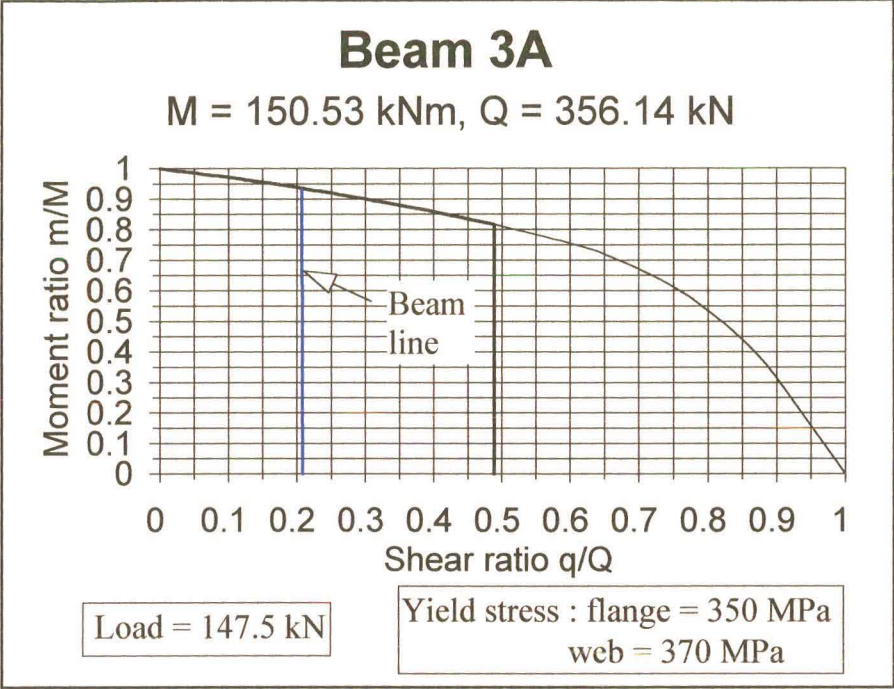


Figure 3.48 : Design chart for Beam 3A, midpoint loading

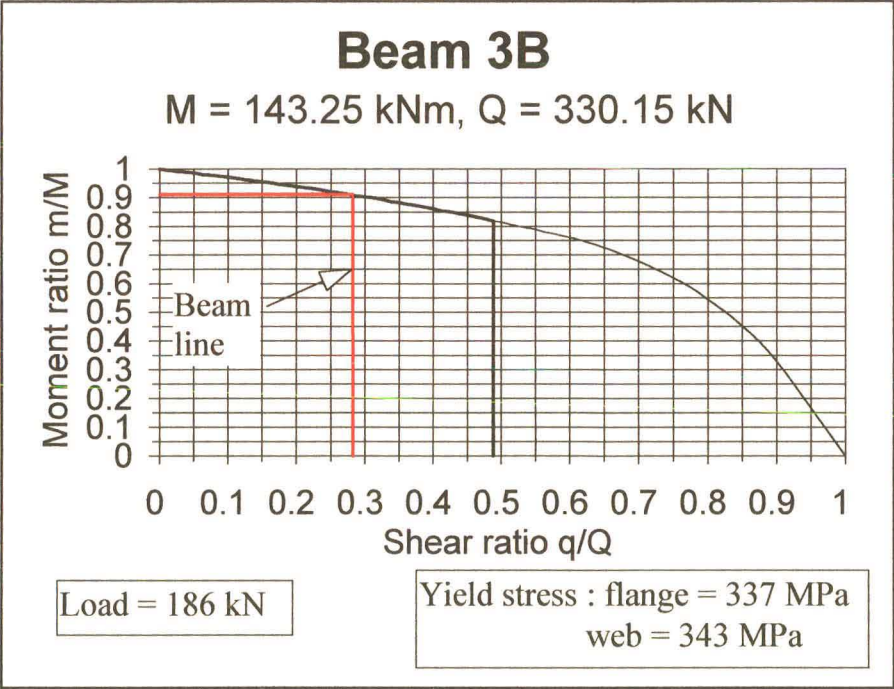


Figure 3.49 : Design chart for Beam 3B, third point loading

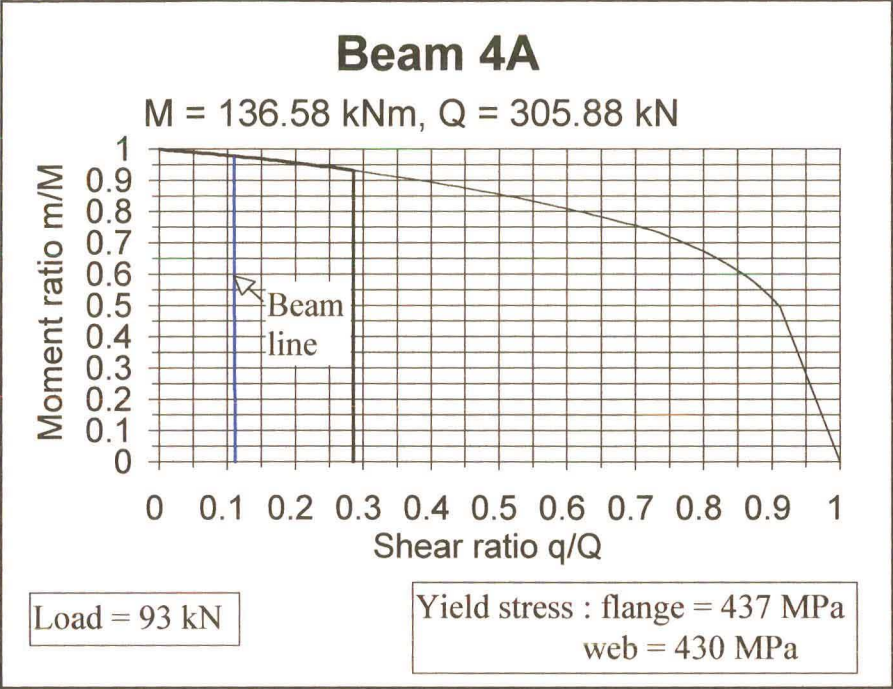


Figure 3.50 : Design chart for Beam 4A, midpoint loading

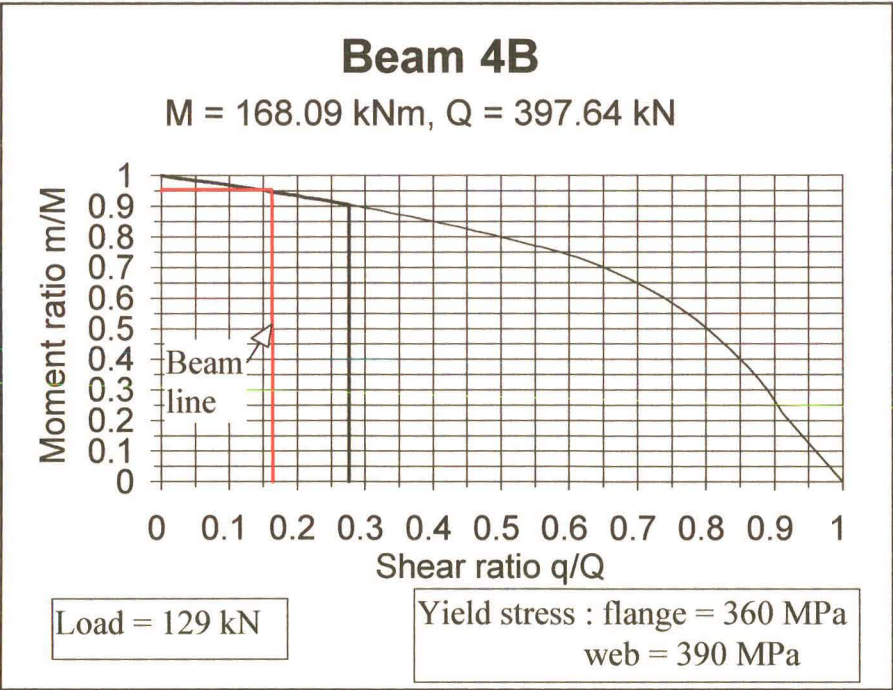


Figure 3.51 : Design chart for Beam 4B. third point loading

Vierendeel failure was predicted for all the beams at the openings with the maximum combined shear and moment. These are the central openings for beams loaded at the midpoint, and the opening on the support side of the load for beams loaded at the third points.

This is in contrast to the spreadsheet results for beams loaded at the third points, where pure bending failure was predicted in the middle third of the beam. The depth of the rectangular approximation to the circular opening for the chart (the diameter of the opening) is greater than that for the spreadsheet, thus the tee sections considered for the chart will be shallower, and have a lower strength, than those considered for the spreadsheet. The method of plotting the beam line on the chart, i.e. assuming that each position on the beam is the centre of an opening, is a conservative method. Vierendeel failure is predicted at a lower load than pure bending failure because of this.

The theoretical failure load values are compared to the experimental values in Figure 3.52.

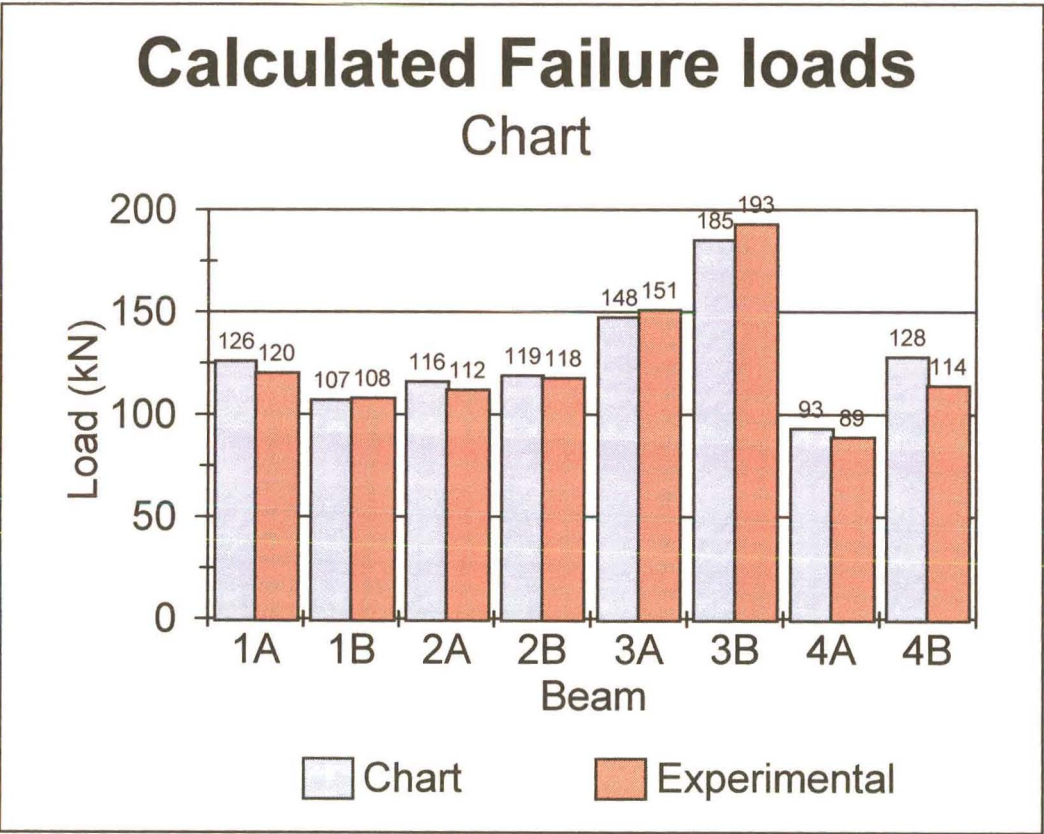


Figure 3.52 : Calculated and experimental failure loads, chart

The ratios between these theoretical values and experimental values are given in Table 3.4.

Table 3.4 : Failure load ratios, chart

Beam	Failure load ratio
1A	1,05
1B	0,99
2A	1,04
2B	1,01
3A	0,98
3B	0,96
4A	1,05
4B	1,12
Mean	1,03

It is evident that the design chart approach provides a very accurate estimate of failure loads.

3.4.2 Finite Element Analysis

The LUSAS program was used for the finite element analysis (FEA). LUSAS is a general purpose finite element analysis program which is capable of handling non-linear static analysis and elasto-plastic materials. A pre-processing and post-processing graphical program, MYSTRO, was used for setting up the models and compiling the results after the analysis.

Modelling

The symmetry of the beams was exploited and only one half of the beam was modelled. To simulate the other half of the beam, the line of symmetry down the center of the beam was restrained against translation in the x direction and against rotation about the y and z axes. (Figure 3.53)

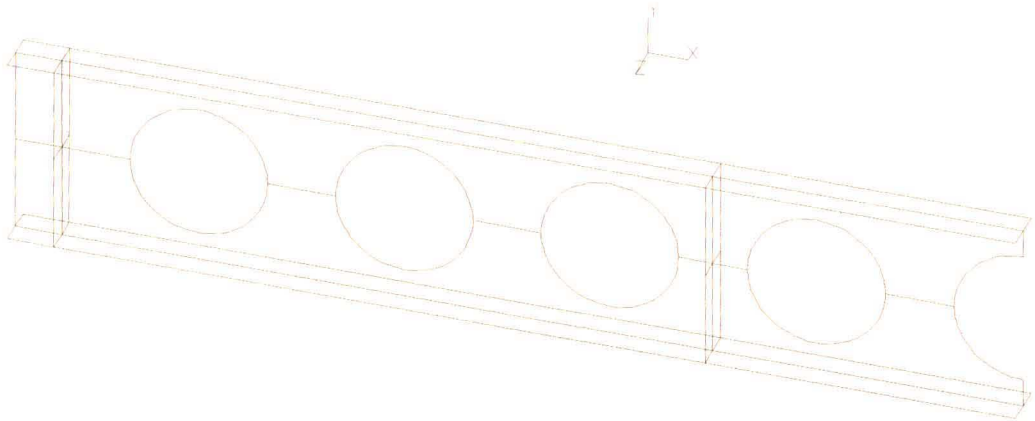


Figure 3.53 : Finite Element Analysis model, Beam 3B

An initial analysis was carried out without the stiffeners and high local stresses developed in the web at the loads and supports. The stiffeners were therefore included as part of the model.

The beam was modelled as a number of surfaces representing the flange, web and stiffeners. These surfaces were given thicknesses corresponding to the thickness of the element they represented. Material types were assigned to each surface. Three material attributes were defined representing the three phases of the material behaviour obtained from a tensile stress test. Figure 3.54 shows a typical stress strain curve for grade 300W steel. The first phase (the elastic phase) has properties: Poisson's ratio (0,3), Young's modulus (200 GPa) and density (7850 kg/m³). The second phase (yielding) was modelled using the Von Mises yield criterion and only the yield stress was specified. Yield stresses used were those derived from the experimental tensile tests on samples taken from each beam, and different values were obtained for flange and web. (The values obtained for the yield stresses are given in section 2.6.) The final phase of the material behaviour, the strain hardening phase, was defined by the strain hardening part of the stress versus total strain curve for grade 300W steel¹. Yield stresses for the steel from the beams tested differed from those in the 300W stress strain curve so the slope of the 300W curve was used together with the yield stresses from the experimental tensile tests. Yielding was assumed to have occurred at the same value of total strain but with the actual yield stress. The stress strain curves used to determine the strain hardening properties are included in Appendix A2.

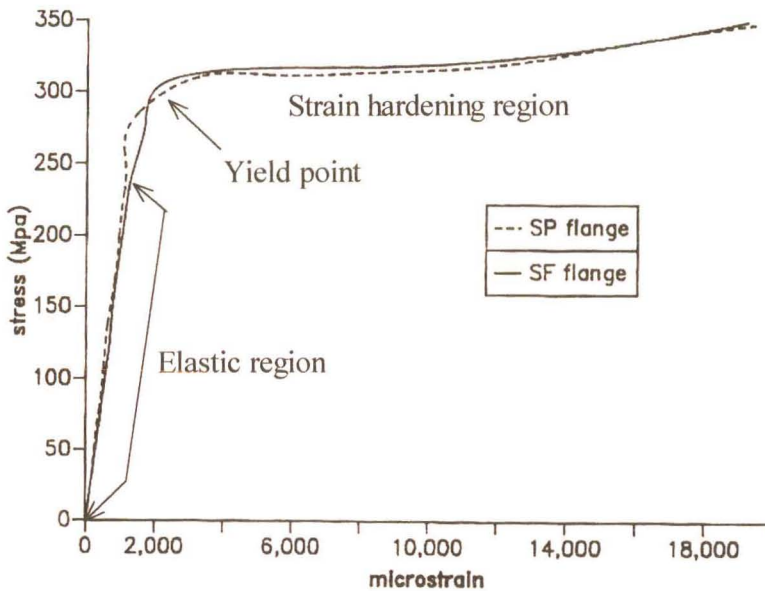


Figure 3.54 : Typical stress strain curve

The element type used was a thick shell element. The attributes of this element type which made it suitable for this analysis are that it is capable of simulating linear and non-linear material behaviour and takes into account flexural and shear deformations.

The support was modelled as a line of restraint in the z direction preventing y-displacements at the end stiffener. Support in the experimental work was provided by a half roller under the end stiffener (Chapter 2, Figure 2.3) which only restrains movement in the y direction. Loading was modelled as a vertical line load along the top of the inner stiffener. In the case of the beams loaded at the third points in the experimental work, the load was applied by a half roller which is modelled very precisely by a line load. Beams loaded at the midpoint were loaded by placing the jack over the central stiffener. This is more like a patch load, but a line load would provide a reasonable approximation.

Analysis

Each beam was analysed linearly and then non-linearly. The initial linear elastic analysis gave a good indication of the load at which the beam was likely to yield. This information was needed in formulating the load increments for the non-linear plastic analysis.

The load incrementation for the plastic analysis was carried out using load factors. The load at which first yield was likely to occur, as determined from the elastic analysis, was allocated a load factor of one. The analysis actually commenced at a load factor less than one so as to provide sufficient data for comparison with the strain gauges and dial gauges. The load factor was incremented typically by 0,15 for each load step.

The program works in an iterative manner using incremental loads. When yielding spreads through the beam, the iterations fail to converge and the program then decreases the load to accurately find the peak load-carrying capacity of the beam. This final load is taken as the failure load for the finite element analysis.

The optimum number of elements for the analysis was investigated using test beam 2A. A number of analyses were carried out using different numbers of elements until the output failure load converged on the solution as shown in Figure 3.55.

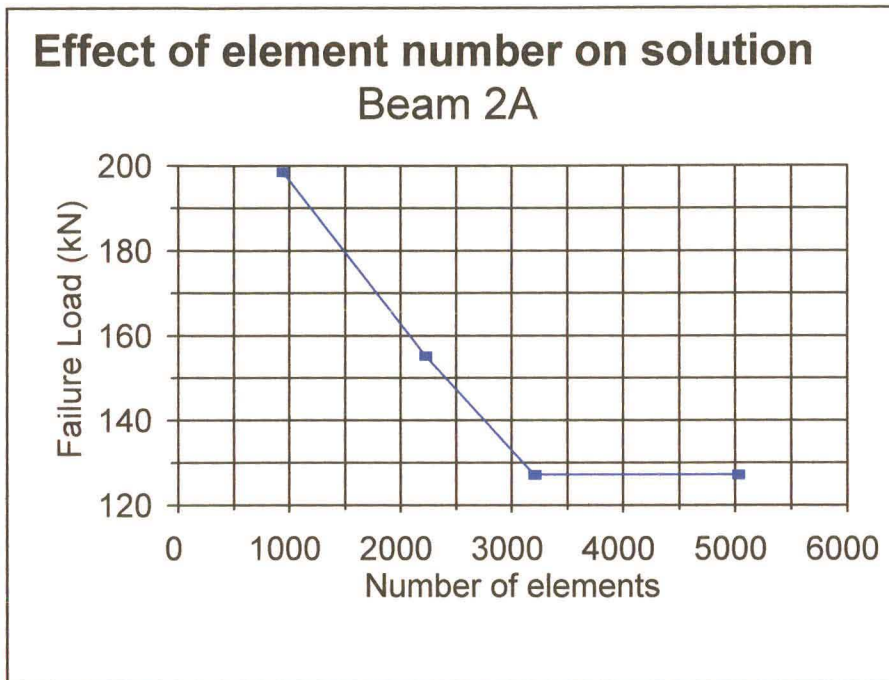


Figure 3.55 : Convergence of FEA solution

This graph was based on nominal yield stresses of 310 MPa and 330 MPa for the flange and web respectively.

The final analysis for this beam was carried out using approximately 5000 elements. The number of elements used for subsequent beams was determined by keeping the same element size as that used for Beam 2A. A triangular mesh of elements was used for the web to fit around the openings and a rectangular mesh was used for the flange and the stiffeners. The mesh was coarser, i.e. bigger elements, towards the end of the beam and more refined nearer the centre where the stresses are higher and where failure ultimately takes place. Time was a consideration because the larger beams took over a week to analyse on a 466 MHz Pentium with 128 MB of RAM, and this time could be reduced by using a coarser mesh in the areas where the stresses were lower and had little effect on the solution. (Figure 3.56, Appendix A2 contains diagrams of the mesh for each beam.)

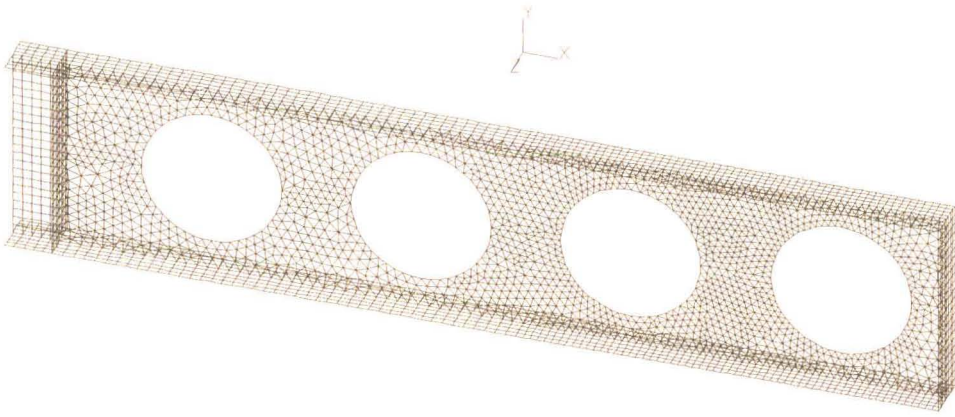


Figure 3.56 : Beam 3A, Finite Element Analysis mesh

Results

The output from the finite element analysis consists of graphical representations of spread of yield, stress contours, principle stress directions and deformed shape of the beam. Numerical results are given for stress and displacement values at each node for each load increment.

The graphical output was used to obtain a feel for the way the stresses were distributed in the beam, and to identify yielded areas which defined the critical positions in the beam. The yield patterns and deformed shapes were compared to the photographs of the yielding and deformation which took place during the experimental tests.

The values of the stresses given at each node point were the major principle stresses. These were compared to the principle stresses obtained from the strain gauge readings. The degree of correlation between the two was used to validate the finite element analysis model and the accuracy of the strain gauges.

The magnitude and direction of the principle strains are given by:

$$\varepsilon_1, \varepsilon_2 = \frac{1}{2} \left[\varepsilon_a + \varepsilon_c \pm \sqrt{2(\varepsilon_a - \varepsilon_b)^2 + 2(\varepsilon_b - \varepsilon_c)^2} \right]$$

$$\tan 2\theta = \frac{2\varepsilon_b - \varepsilon_a - \varepsilon_c}{\varepsilon_c - \varepsilon_a}$$

where ε_a , ε_b and ε_c are the strain readings from the strain gauges.

ε_1 and ε_2 are the maximum (major) and minimum (minor) principle stresses respectively.

θ is the angle between ε_a and the major principle strain. (Figure 3.57)

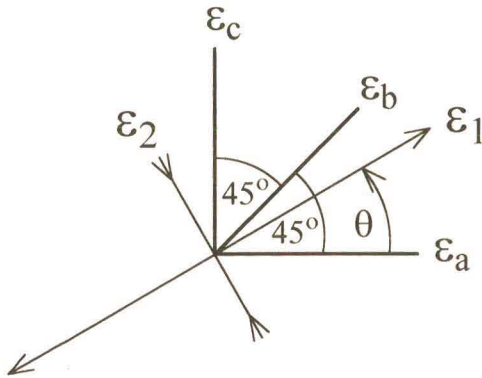


Figure 3.57 : Principle stress directions from strain gauges

Strains were converted into stresses by multiplying by Young's modulus, E , which was taken as 200 GPa for grade 300W steel:

$$E = \frac{\sigma}{\varepsilon} \quad \therefore \sigma = \varepsilon \times E$$

Two examples of comparisons of strain gauge readings with the FEA nodal stress output are given in Figures 3.58 and 3.59. Appendix A2 contains the full set of graphs.

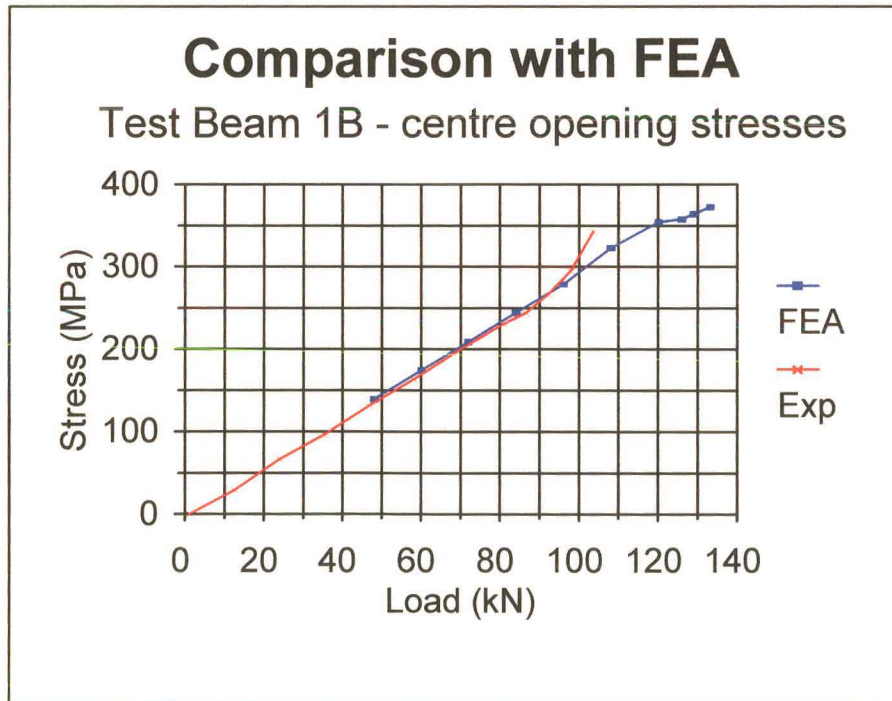


Figure 3.58 : Comparison between FEA and strain gauges, Beam 1B, opening

The increased rate of change of experimental stress at about 280 MPa is due to the occurrence of plastic strain in the vicinity of the strain gauge. As stated previously, the relationship between stress and strain is assumed to be linear and dependant on Young's modulus. When the strains become plastic this no longer holds and an increase in the

rate of change of stress is indicated which has not actually occurred.

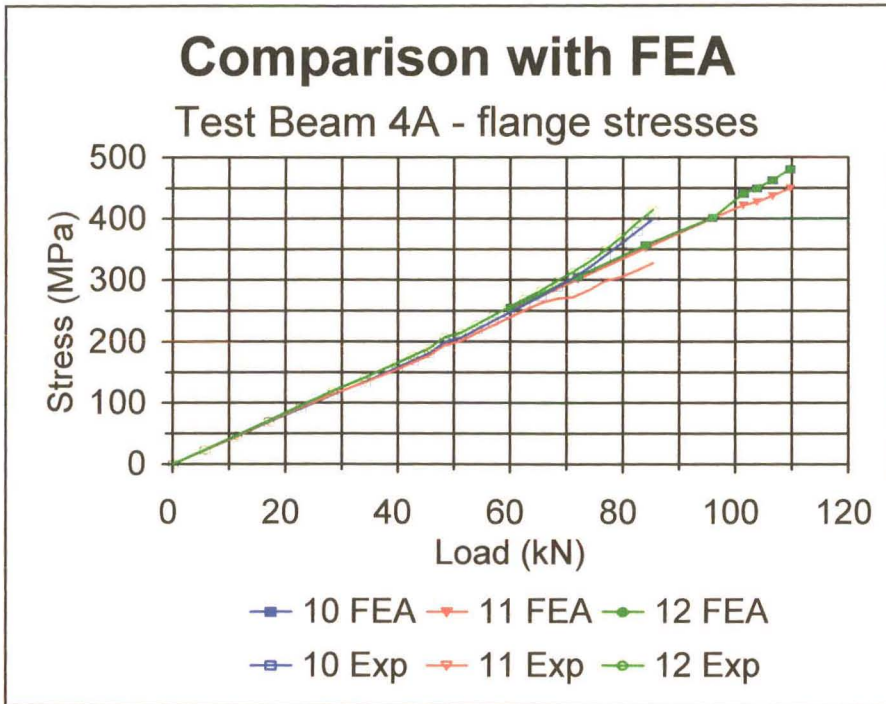


Figure 3.59 : Comparison between FEA and strain gauges, Beam 4A, flange

Figures 3.58 and 3.59 show that the FEA nodal stresses agree closely with the principle stresses obtained from the strain gauge readings. These two graphs are typical of the 48 graphs which were plotted for the comparison between the FEA and strain gauges results.

A comparison of failure loads given by the Finite Element method with the experimental values is given in Figure 3.60.

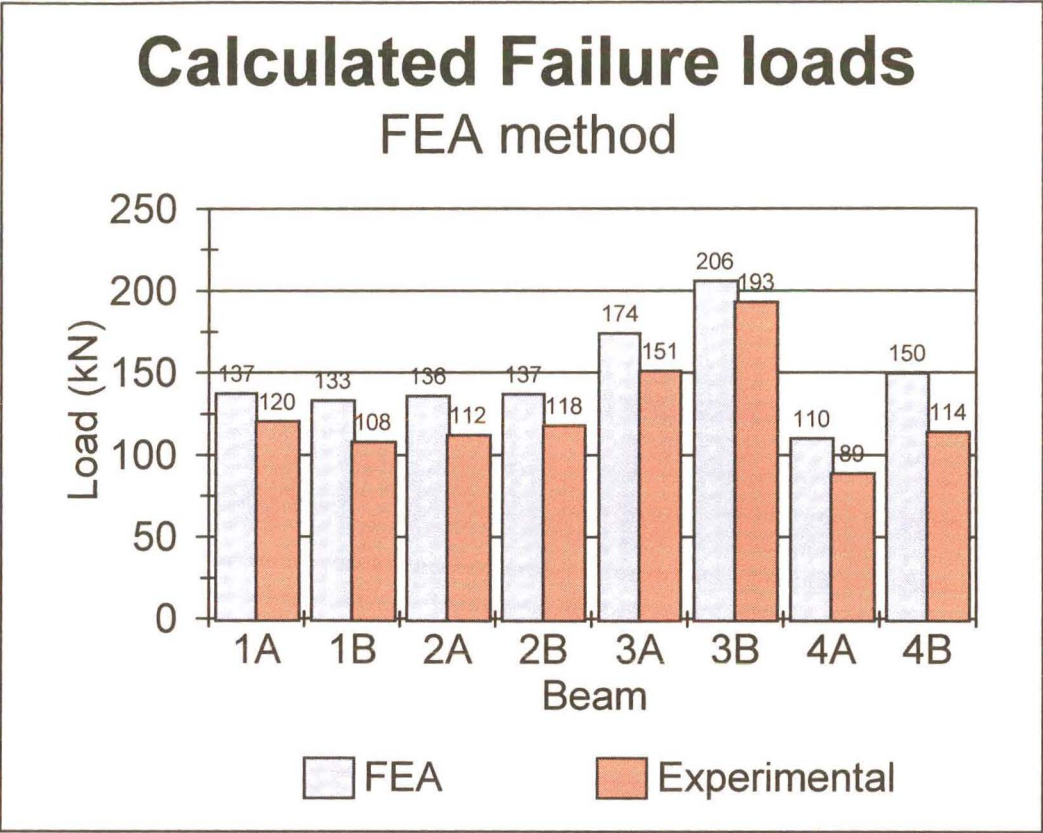


Figure 3.60 : Calculated and experimental failure loads, chart

The failure loads predicted by the FEA method are all significantly greater than the experimental values. It was noted in the FEA models that large plastic deflections occurred before the beam failed, whereas only small plastic deformations were observed in the experimental beams at failure.

The ratios between the FEA failure loads and the experimental values are given in Table 3.5.

Table 3.5 : Failure load ratios, FEA

Beam	Failure load ratio
1A	1,14
1B	1,23
2A	1,21
2B	1,16
3A	1,15
3B	1,07
4A	1,24
4B	1,31
Mean	1,19

3.5 Summary

The failure load ratios (theoretical/experimental) and modes of failure for all the methods considered are given in Table 3.6:

Table 3.6 : Summary of results

Beam	SCI	Spreadsheet	Chart	FEA	Experimental
	Failure load ratio and failure mode	Failure load ratio and failure mode	Failure load ratio and failure mode	Failure load ratio	Failure load (kN) and failure mode
1A	0,74	1,21	1,05	1,14	120
	Vierendeel	Vierendeel	Vierendeel		Vierendeel
1B	0,76	1,13	0,99	1,23	108
	Vierendeel	Pure Bending	Vierendeel		Vierendeel
2A	0,66	1,15	1,04	1,21	112
	Vierendeel	Vierendeel	Vierendeel		Vierendeel
2B	0,73	1,14	1,01	1,16	117
	Vierendeel	Pure Bending	Vierendeel		Vierendeel
3A	0,78	1,13	0,98	1,15	151
	Vierendeel	Vierendeel	Vierendeel		Vierendeel, both openings
3B	0,72	1,04	0,96	1,07	193
	Vierendeel	Pure Bending	Vierendeel		Vierendeel / buckling
4A	0,76	1,13	1,05	1,24	90
	Vierendeel	Vierendeel	Vierendeel		Pure Bending
4B	0,9	1,18	1,12	1,31	108
	Vierendeel	Pure Bending	Vierendeel		Buckling / slight Vierendeel

The mean and standard deviation of the failure load ratios were calculated for each method. The failure load ratio for Beam 4B was noticeably higher for all the methods used. This may be explained by the fact that Beam 4B failed in buckling before plastic failure was fully developed. Two sets of means and standard deviations were calculated, one including Beam 4B and the other excluding it. (Table 3.7)

Table 3.7 : Failure load ratios mean and standard deviation

	SCI	Spreadsheet	Chart	FEA
Including Beam 4B				
Mean	0,76	1,14	1,02	1,19
Standard deviation	0,065	0,045	0,049	0,071
Excluding Beam 4B				
Mean	0,74	1,13	1,01	1,17
Standard deviation	0,037	0,046	0,033	0,057

These values can be represented graphically by drawing normal distribution curves. (Figure 3.61) Ideally the curves would be centered on unity with a small spread. The more “peaked” the curve, the smaller the standard deviation i.e. all the individual ratios are close to unity. If the curve is flatter then it indicates a greater spread of values, and even if it is centered on unity, each individual ratio may not be close to unity. If the curve is centered to the left of unity, i.e. mean of less than unity, then the method is conservative, conversely if the curve is centered to the right of unity, i.e. mean greater than unity, then the method is unconservative.

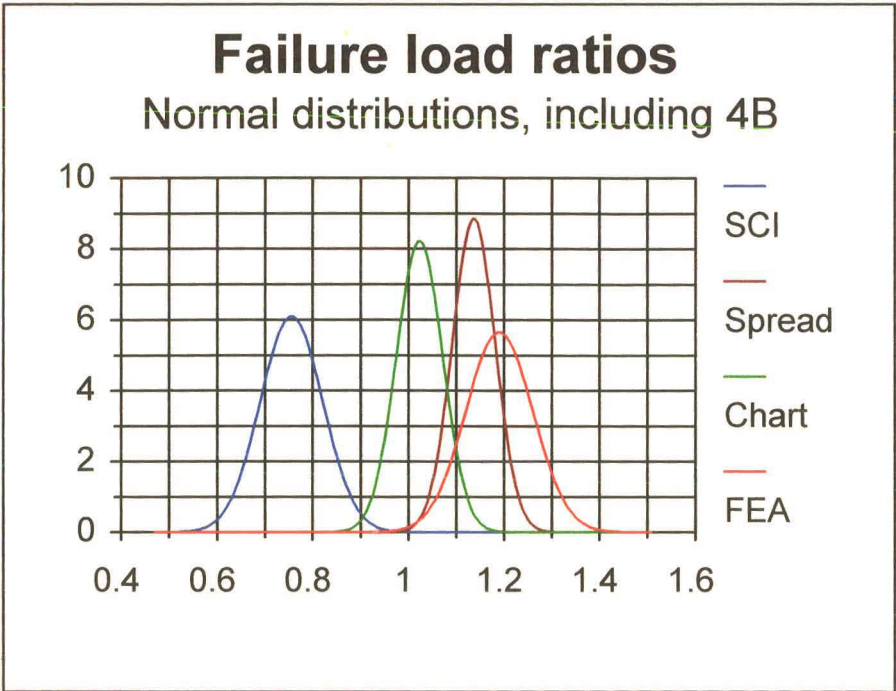


Figure 3.61 : Normal distributions of failure ratios, including Beam 4B

The distributions in Figure 3.61 show that the SCI method is very conservative whereas the plastic vierendeel spreadsheet method and the FEA method are both unconservative. The curve for the design charts is centered very close to unity. These distributions include the ratios from Beam 4B. A similar diagram, excluding the results of Beam 4B, is given in Figure 3.62.

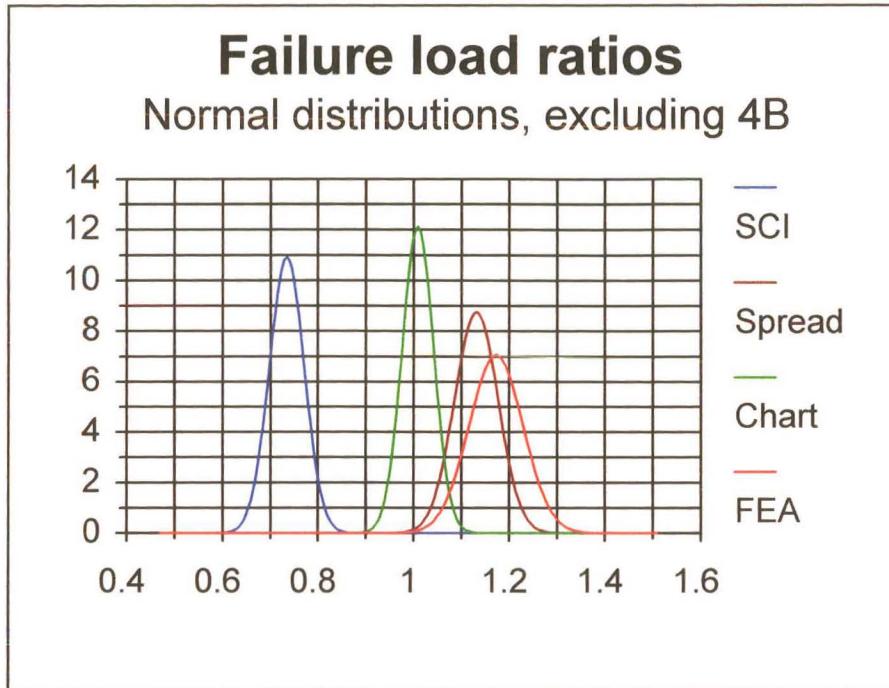


Figure 3.62 : Normal distributions of failure ratios, excluding Beam 4B

The distributions for the SCI, spreadsheet and chart method are more “peaked” when the ratios for Beam 4B are excluded. It can be clearly seen from Figure 3.62 that the plastic vierendeel design chart method is the most accurate. The distribution for the chart is the most “peaked” and it is centered the closest to unity. By applying a factor of $\frac{1}{\text{mean}}$ to all the results from the chart, the mean could be brought to unity. The chart also has the advantage that it is simple to use and would be a viable option for the plastic analysis of cellular beams in practice.

CHAPTER 4

DEFLECTIONS OF CELLULAR BEAMS

4.1 Introduction

Only elastic deflections were investigated, since deflections are a serviceability consideration and service loads fall into the elastic range of deflections.

Shear has a greater effect in cellular beams than in solid-webbed beams because of the effect of Vierendeel deflections across the openings.

The effect of self weight was excluded in the deflection calculations because the zero reading in the experimental tests was taken with the beam in position, already deflected under its self weight.

To simplify comparison between theoretical and experimental deflections, the gradient of the load versus deflection graph was calculated. If the beam is in the elastic region (as is the case here) then the load versus deflection graph is a straight line and the ratio of gradients will be equal to the ratio of deflections.

In addition to the gradient ratios, comparisons were made by plotting the experimental and theoretical deflections. Examples of these plots are given for each deflection method used in this chapter; a full set of plots has been included in Appendix A3.

4.2 Existing Methods of Analysis

4.2.1 British Steel Construction Institute Method¹⁰ (the SCI method)

Theory

The circular opening from the cellular beam is converted into a hexagonal opening as shown in Figure 4.1.

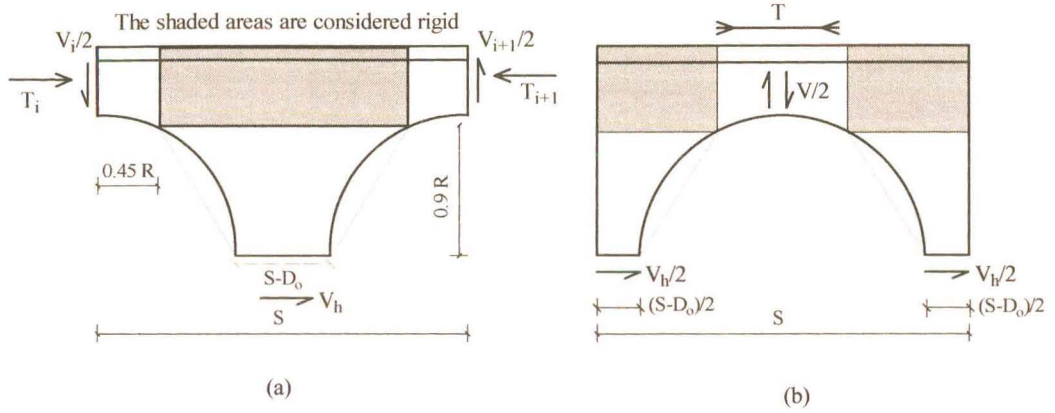


Figure 4.1 : Free body diagrams for SCI deflection calculations

Virtual work forms the basis for the SCI deflection method. The deflection at a point in the beam is found by applying a unit load at that point. The unit load induces the internal forces shown in Figure 4.2:

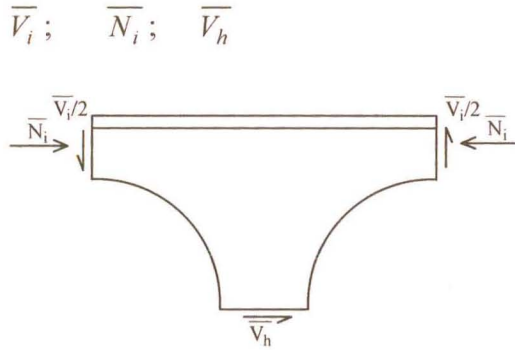


Figure 4.2 : Internal forces due to unit load

This method takes into account five components of deflection:

- (i) Bending in the tee (Vertical shear)

$$y_1 = \frac{4}{EI_{tee}} \int_0^{0.45R} \frac{V_i x}{2} \frac{\overline{V}_i x}{2} dx$$

$$= \frac{0.091R^3}{3EI_{tee}} (V_i \overline{V}_i)$$

(ii) Bending in the web post (Horizontal shear)

$$\begin{aligned}
 y_2 &= \frac{2}{EI_z} \int_0^{0,9R} V_h z \overline{V_h z} dz \\
 &= \frac{13,145}{Et_w} \left[\log_e \left(\frac{S-0,9R}{S-2,0R} \right) + 2 \left(\frac{S-2,0R}{S-0,9R} \right) - \frac{1}{2} \left(\frac{S-2,0R}{S-0,9R} \right)^2 - \frac{3}{2} \right] V_h \overline{V_h}
 \end{aligned}$$

(iii) Axial force in the tee

$$\begin{aligned}
 y_3 &= \frac{4}{EA_{tee}} \int_0^{\frac{S}{2}} T_i \overline{N_i} dx \\
 &= \frac{2S}{EA_{tee}} T_i \overline{N_i}
 \end{aligned}$$

(iv) Shear in the tee (Vertical shear)

$$\begin{aligned}
 y_4 &= \frac{4}{GA_{tee}} \frac{A_{tee}}{A_{tee,web}} \int_0^{0,45R} \frac{V_i \overline{V_i}}{4} dx \\
 &= \frac{0,45R}{GA_{tee,web}} V_i \overline{V_i}
 \end{aligned}$$

(v) Shear in the web post (Horizontal shear)

$$\begin{aligned}
 y_5 &= \frac{2}{GA_z} \chi \int_0^{0,9R} \frac{V_h}{2} \frac{\overline{V_h}}{2} dz \\
 &= \frac{1,636}{Gt_w} \chi \log_e \left(\frac{S-0,9R}{S-2,0R} \right) V_h \overline{V_h}
 \end{aligned}$$

The total deflection due to one opening is the sum of four times the deflection due to one half of the tee and twice the deflection due to one half of the web post. This has been accounted for in the above equations, and the total deflection is found by summing the individual deflections for all openings:

$$\text{i.e. } y_i = \sum y_n$$

The original SCI method of summing the deflections assumed that the forces acting on the free body and causing the deflections were those to the left of the free body (Figure 4.1(a)). (Figure 4.3(a) indicates how the deflections were summed.) The results obtained from this method were considerably smaller than experimental values.

A new method of summing the deflections was therefore developed whereby the forces causing deflections were assumed to be those in the middle of the section (Figure

4.1(b)). (Figure 4.3(b) indicates how the deflections were summed) Deflections calculated in this way were in better agreement with experimental deflections. On average the deflections calculated by the original method were 90% of those calculated using the adjusted method.

If the beam in Figure 4.3 is considered, the original method of summing the deflections gives:

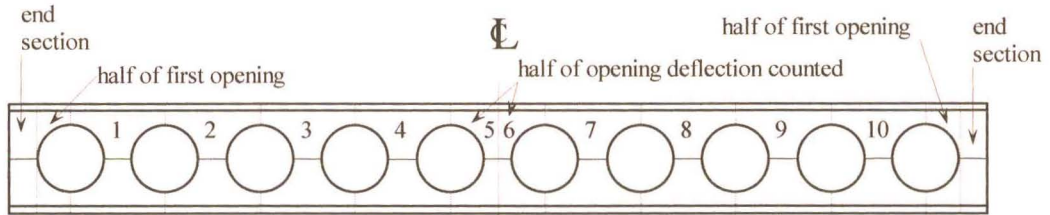
$$\Delta = 2 \times \delta_{\text{end section}} + 2 \times \frac{\delta_{\text{st opening}}}{2} + \delta_1 + \delta_2 + \delta_3 + \delta_4 + \frac{\delta_5}{2} + \frac{\delta_6}{2} + \delta_7 + \delta_8 + \delta_9 + \delta_{10}$$

(Figure 4.3(a)) where Δ is the total deflection and δ is the deflection due to each opening as labeled in Figure 4.3.

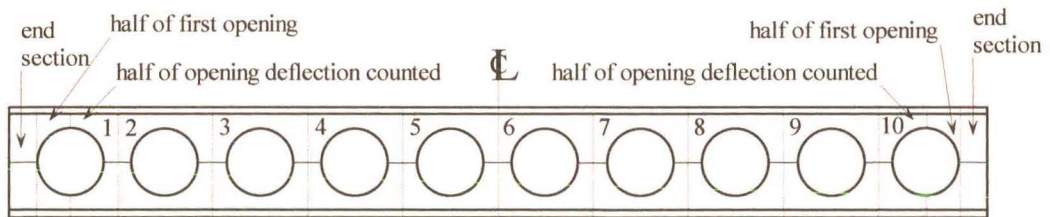
The adjusted method of summing the deflections gives:

$$\Delta = 2 \times \delta_{\text{end section}} + 2 \times \frac{\delta_{\text{st opening}}}{2} + \frac{\delta_1}{2} + \delta_2 + \delta_3 + \delta_4 + \delta_5 + \delta_6 + \delta_7 + \delta_8 + \delta_9 + \frac{\delta_{10}}{2}$$

(Figure 4.3(b))



(a) Original SCI method



(b) Adjusted method

Figure 4.3 : Summing methods for SCI deflection calculations

Results

Deflections were calculated for each load at which dial gauge readings were taken during the experimental work. The results for Test Beams 2A and 3B are shown in Figures 4.4 and 4.5 respectively. The three vertical dial gauges used for each beam were labelled V1, V2 and V3. Diagrams with the positions of each dial gauges are given in Appendix A1.

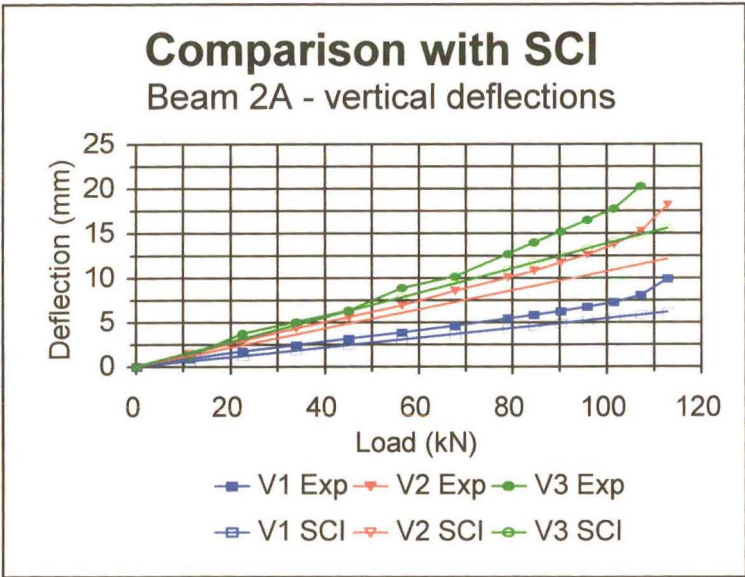


Figure 4.4 : SCI deflections, Beam 2A

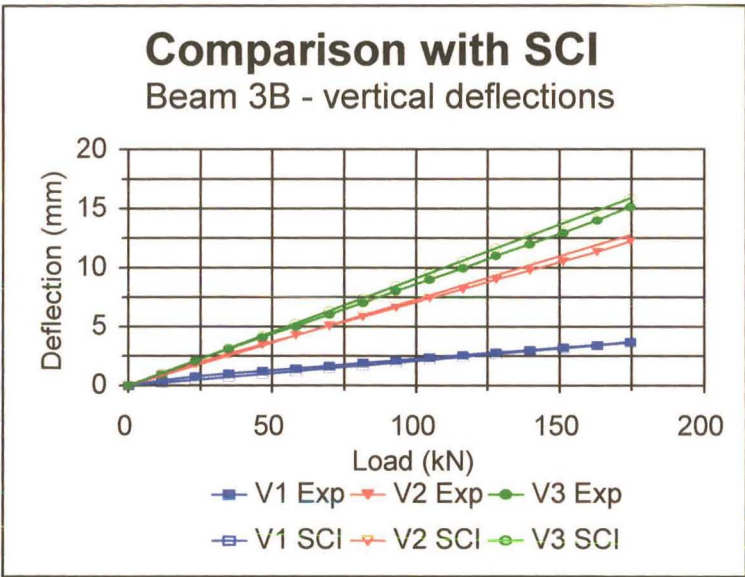


Figure 4.5 : SCI deflections, Beam 3B

There is close agreement between the theoretical and experimental deflection for Beam 3B in Figure 4.5. The results do not agree as well for Beam 2A in Figure 4.4.

As described earlier, the ratios of the gradients of the deflection lines were used as an indication of how well the results from the theoretical method agreed with the experimental results. These ratios were calculated for each of the three positions at which deflections were measured. The mean of the three ratios for each beam was found and these are given in the graph below. The full set of individual ratios are given in Appendix A3.

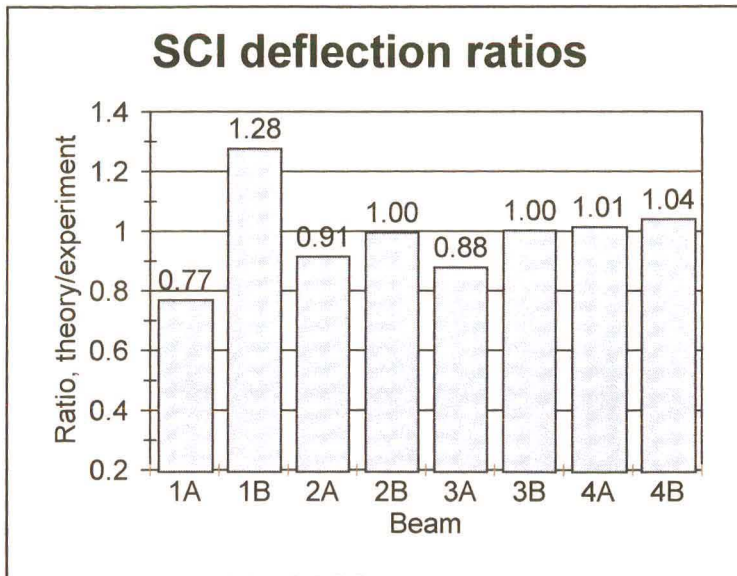


Figure 4.6 : Deflection ratios for SCI method

With the exception of Beams 1A and 1B, the ratios are close to unity indicating that this method is accurate.

4.2.2 Simplified British Steel Construction Institute method

As a simpler alternative, the SCI proposes an approximate method that ignores all shear deflections, but adds 25% to the bending deflections to account for the shear. The moment of inertia is calculated using the perforated section. A criticism of this method is that it applies a blanket factor without considering the shear-to-moment ratio. Deflections in beams with a high shear-to-moment ratio will be underestimated, those in beams with a low shear-to-moment ratio will be overestimated. This is seen to be the case in the comparisons with the experimental data.

Results

Deflections were calculated at each load where readings were taken in the experimental work. The deflection results for Test Beams 2A and 3B are shown in Figures 4.7 and 4.8 respectively, and the deflection ratios for all test beams are shown in Figure 4.9.

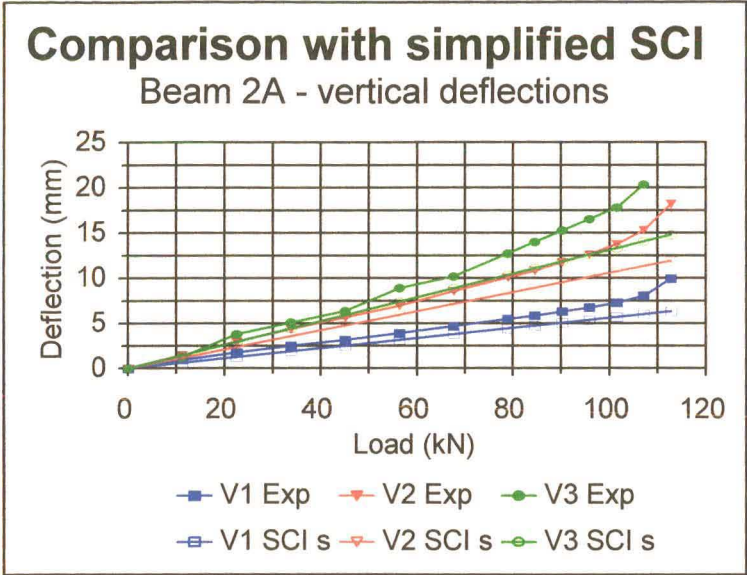


Figure 4.7 : Simplified SCI deflections, Beam 2A

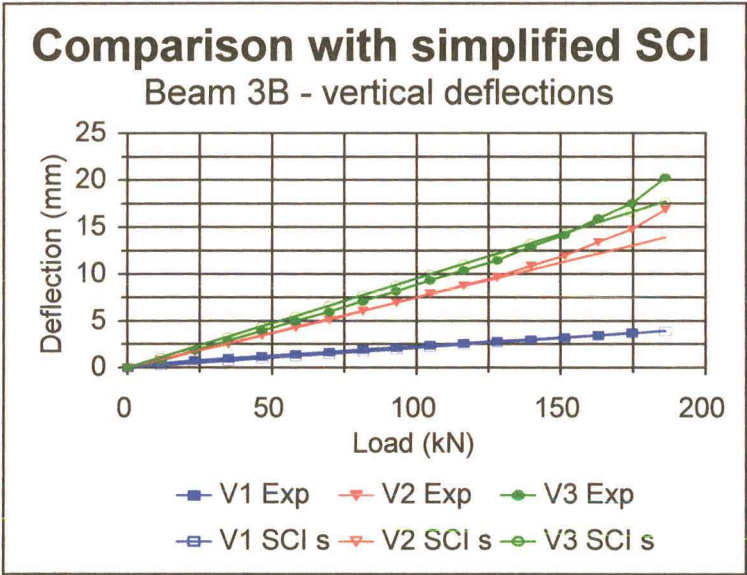


Figure 4.8 : Simplified SCI deflections, Beam 3B

As with the SCI method, there is closer agreement between the theoretical and experimental deflections in Beam 3B than Beam 2A.

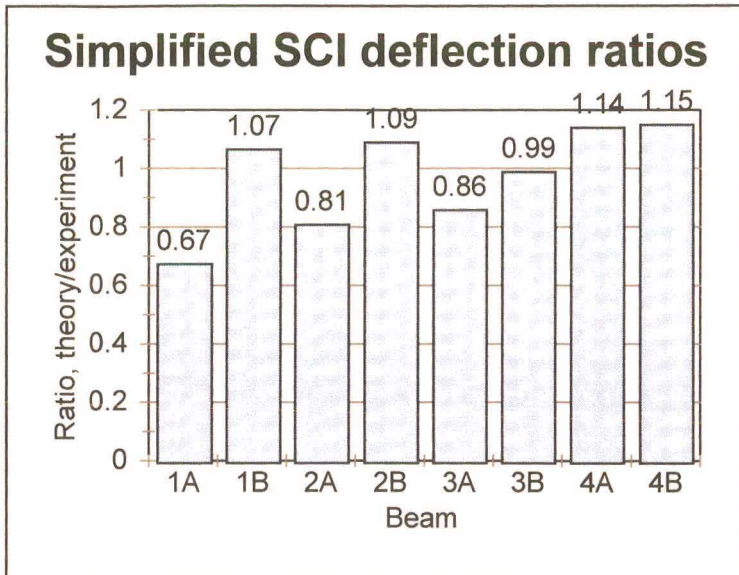


Figure 4.9 : Deflection ratios for simplified SCI method

Beam 3B is the only case where the deflection ratio is close to unity. The remainder of the ratios are either much greater than unity or much smaller than unity.

4.3 Proposed new methods

4.3.1 Vierendeel Method

This method calculates deflections as the sum of two components, viz

- (i) the deflections due to the primary bending
- (ii) the deflections due to the secondary bending effect of the Vierendeel moment.

This secondary bending effect is caused by the shear in the tees.

(i) Primary bending

The primary bending deflections were calculated using the Euler equations. This method ignores any shear deformations and is valid only when the slopes of the deflection curve are small. It also requires the beam to be prismatic, which cellular beams are not. This difficulty was overcome by conservatively taking the moment of inertia as that at the centre of an opening.

The deflection for beams loaded at the midpoint is given by :

$$\delta = \frac{Px}{48EI} (3L^2 - 4x^2)$$

where x is the position along the beam where the deflection is being calculated.

The deflection for beams loaded at the third points are given by:

$$\delta = \frac{Px}{6EI} \left(\frac{2L^2}{3} - x^2 \right) \quad 0 \leq x \leq \frac{L}{3}$$

$$\delta = \frac{PL}{18EI} \left(3Lx - 3x^2 - \frac{L^2}{9} \right) \quad \frac{L}{3} \leq x \leq \frac{L}{2}$$

(ii) Secondary Bending

One quarter of an opening is considered in calculating the Vierendeel deflection. This comprises the tee section spanning half the opening, and one quarter of the adjacent web post, which form a cantilevered section that can be approximated as a stepped tee (Figure 4.10).

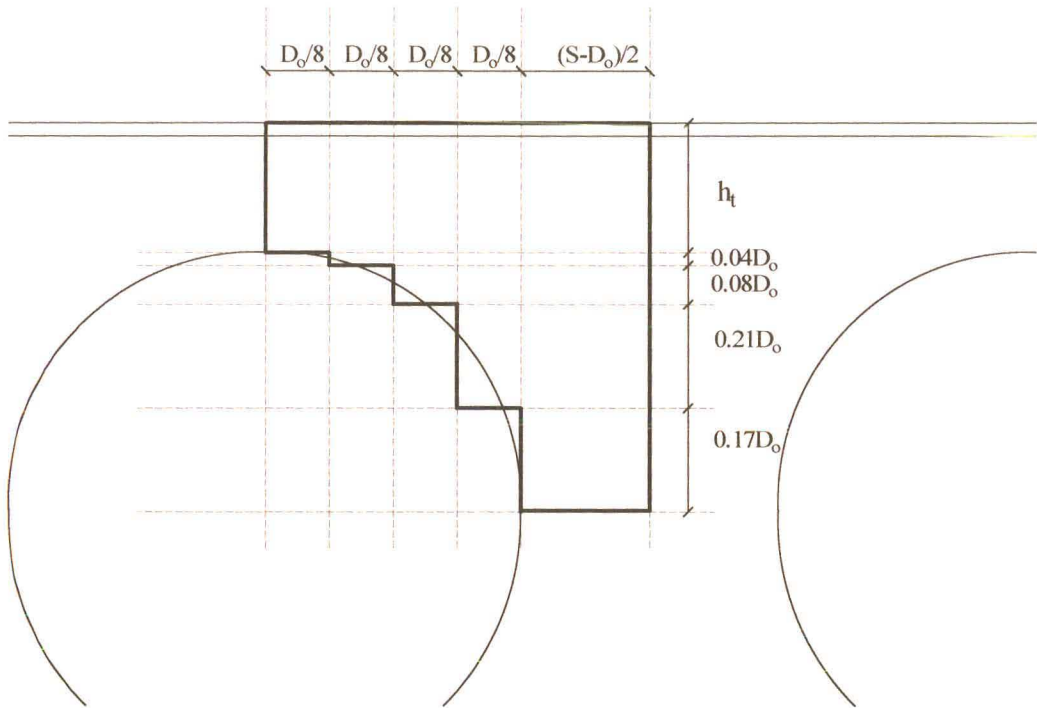


Figure 4.10 : Cantilever section for Vierendeel deflections

The moment-area method was a convenient means of calculating the deflection of each cantilever.

Results

Each cantilever comprises one quarter of an opening. The total Vierendeel deflection was the sum of the Vierendeel deflections at all openings between the support and the position at which the deflection was calculated. The total deflection was the sum of the primary bending deflection and the Vierendeel deflection.

Deflections were calculated for each load at which readings were taken in the experimental tests. The results for Test Beams 2A and 3B are shown in Figures 4.11 and 4.12 respectively; and the deflection ratios for all test beams are shown in figure 4.13.

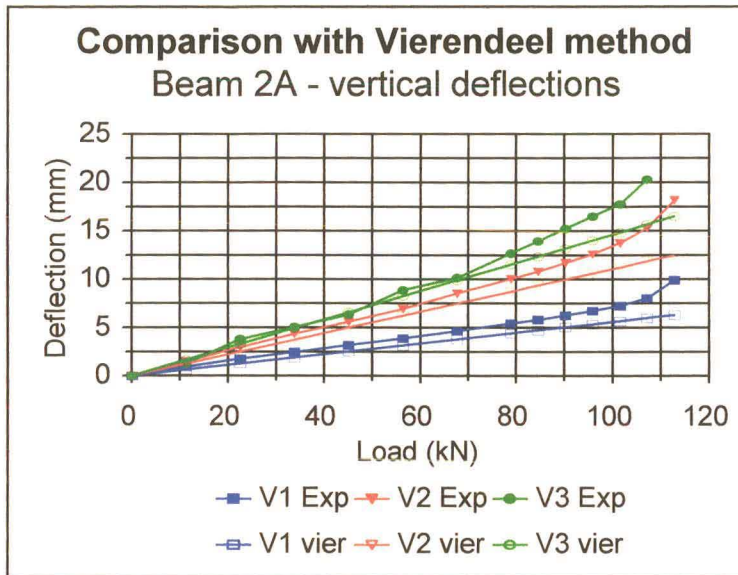


Figure 4.11 : Vierendeel deflections, Beam 2A

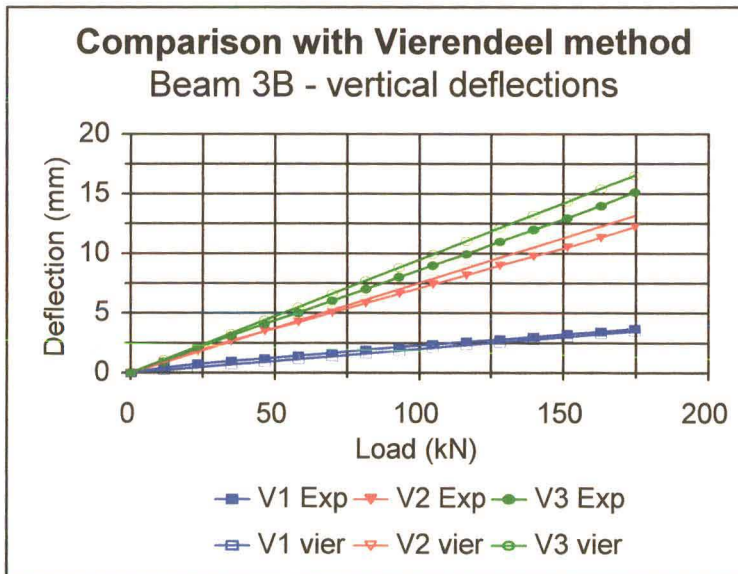


Figure 4.12 : Vierendeel deflections, Beam 3B

The theoretical and experimental deflections agree closely for both beams using this method. This is shown to be true for all the beams, with the exception of Beam 1A, in Figure 4.13.

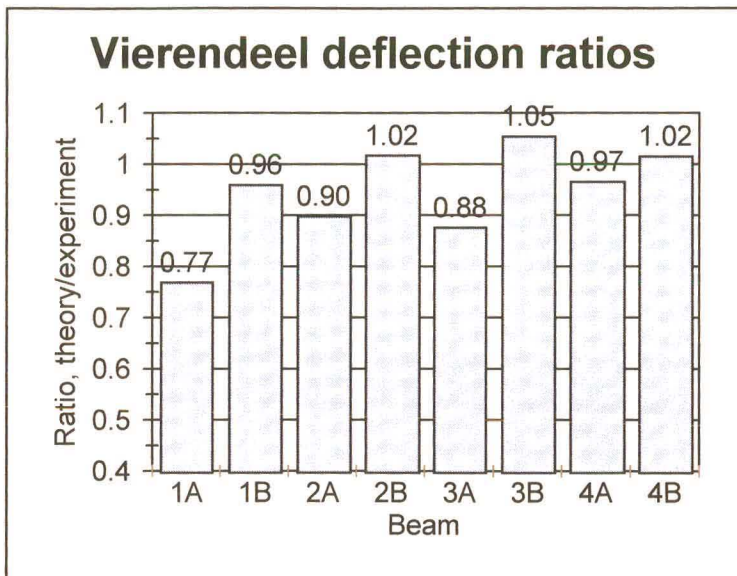


Figure 4.13 : Deflection ratios for Vierendeel method

4.3.2 Finite Element Analysis

One of the outputs from the finite element analysis program is the displacements at each node point. The values are given in the format of a “Comma Separated Values” file which can be read by a spreadsheet. Vertical displacements were read at the node points corresponding to the dial gauge positions.

Elasto-plastic deflections as well as elastic deflections were obtained from the finite element analysis output, but only the elastic deflections were required for comparison with the experimental deflections.

Results

Graphical output from the FEA method included deformed shapes of beams. These can be compared to the photographs of the failed beams.

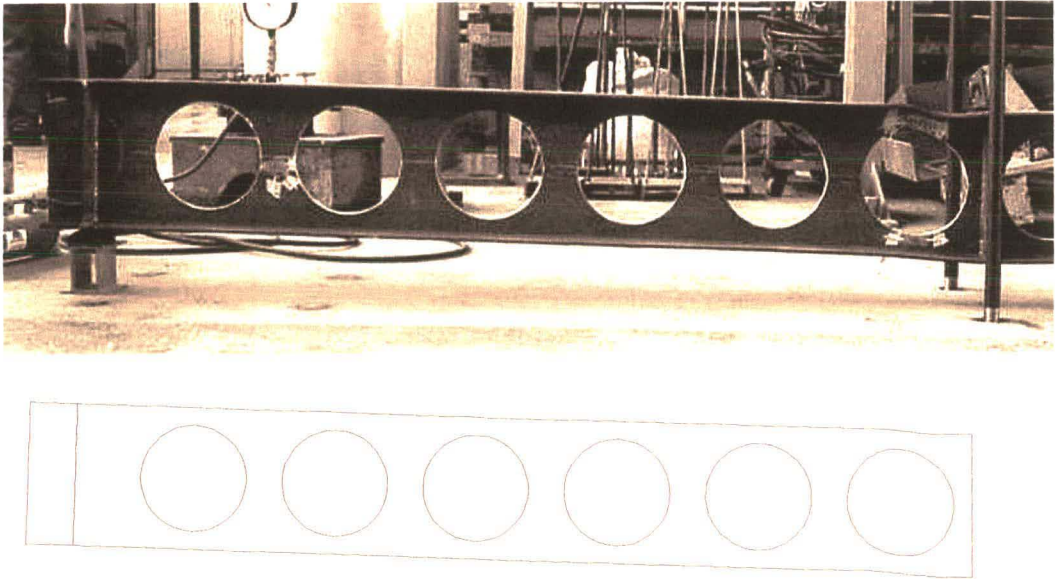


Figure 4.14 : Deformation of Beam 2A

Figure 4.14 compares a photograph of Beam 2A after failure with the deformed shape obtained from the finite element analysis. The deformation of the central opening has the same shape in both diagrams. This is a demonstration of the accuracy with which the FEA method modelled the beam behaviour.

The results for Test Beam 2A and 3B are shown in Figure 4.15 and 4.16 respectively; and the deflection ratios for all test beams are shown in Figure 4.17.

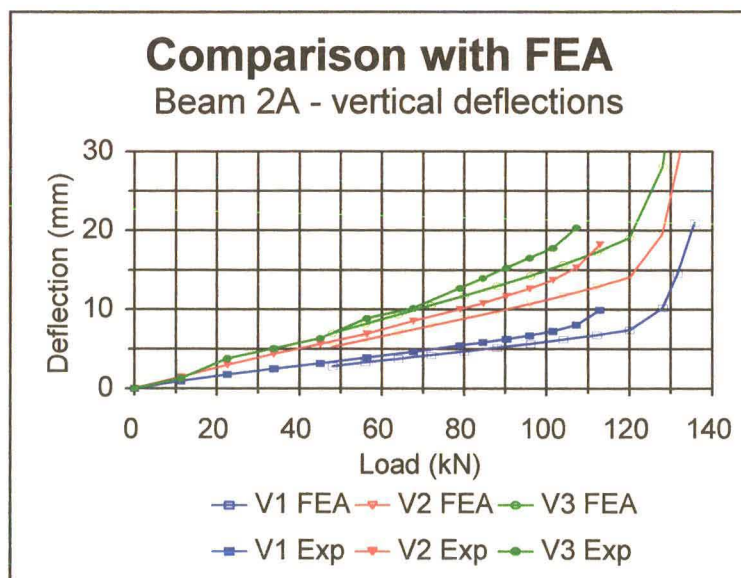


Figure 4.15 : Finite Element deflections, Beam 2A

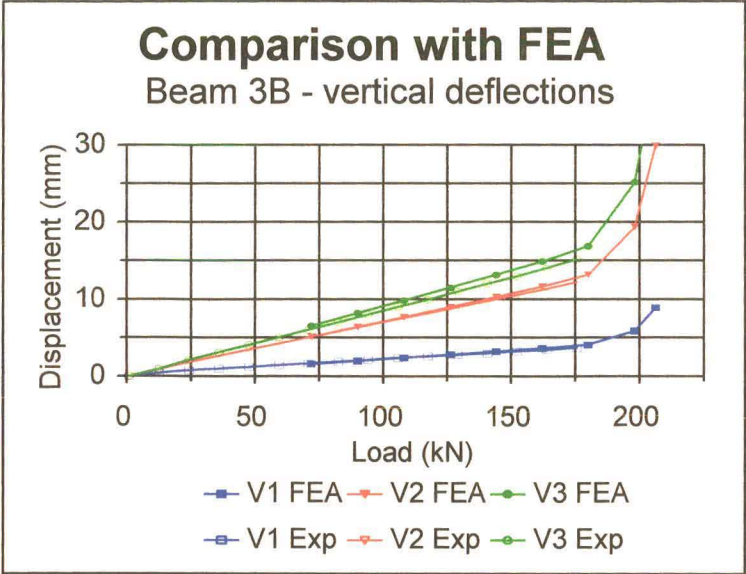


Figure 4.16 : Finite Element deflections, Beam 3B

Considering on the linear parts of the curves, there is a close agreement between the theoretical and experimental deflections for both Beams 2A and 3B. This is seen to be the case for all the beams except Beam 1A and 3A in Figure 4.17.

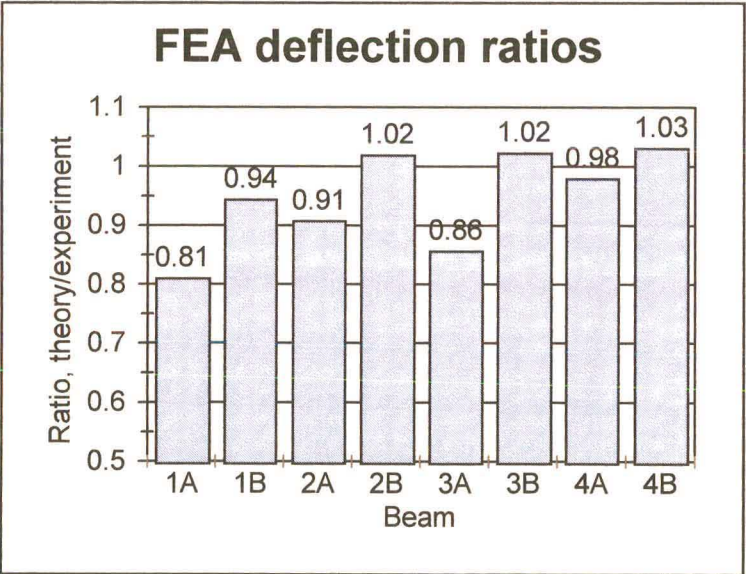


Figure 4.17 : Deflection ratios for Finite Element method

4.4 Summary

A factor which influences the accuracy of the calculated deflections is the shear-to-moment ratio.

The shear-to-moment ratio is the ratio between the average shear stress in the web, τ , to the outside fibre stress in the flange, σ_{\max} , calculated elastically using the properties of the unperforated section.⁴

$$\frac{\tau}{\sigma_{\max}} = \frac{V}{A_w} \frac{2I}{MH}$$

where A_w = area of the web

I = second moment of inertia of the solid section

H = height of the beam

V = shear at the position being considered

M = moment at the position being considered

In order to visualise the effect that the shear-to-moment has on the accuracy of the theoretical deflection calculations, scatter charts (Figures 4.18 to 4.21) were plotted of shear-to-moment ratio against the deflection ratios for each method :

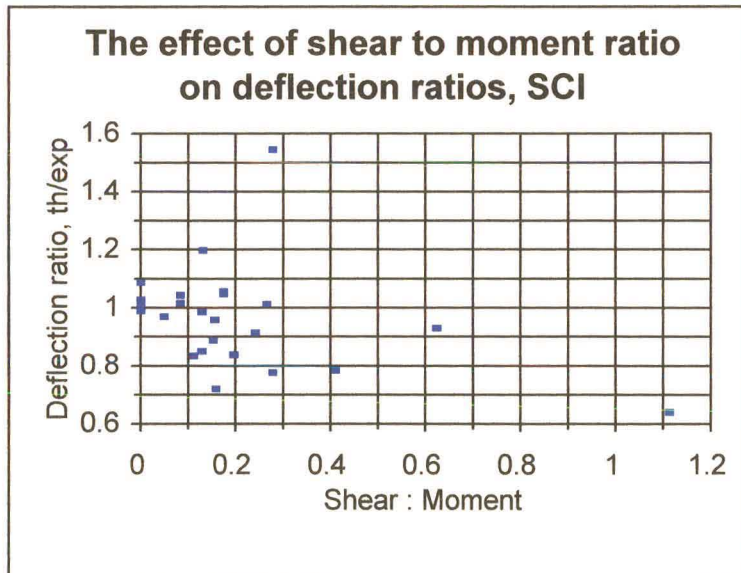


Figure 4.18 : Shear-to-moment and deflection ratios, SCI

Deflections calculated using the SCI method are accurate for zero shear zones in beams. The results are clustered around unity until the shear-to-moment ratio becomes large, when the calculated deflections are considerably less than the experimental values.

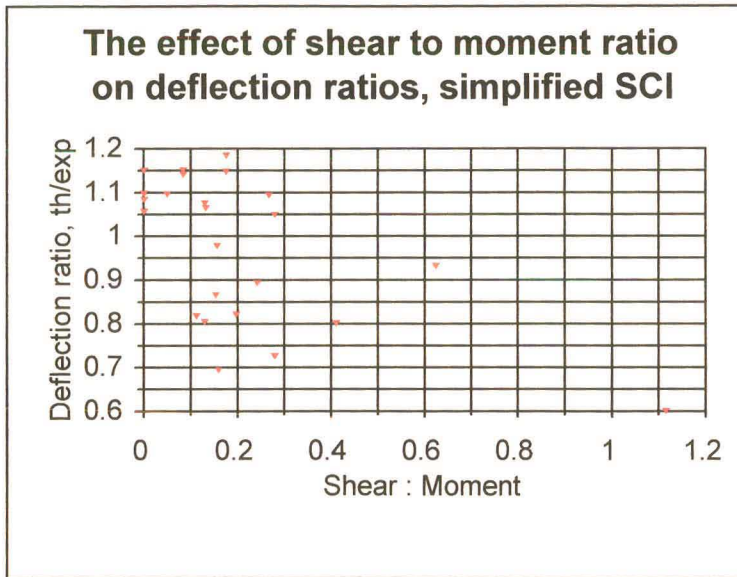


Figure 4.19 : Shear-to-moment and deflection ratios, simplified SCI

The problem with the simplified SCI method is that it applies a blanket factor to allow for shear deformations. Deflections calculated using this method in beams with a small shear-to-moment ratio are greater than the experimental and in beams with a large shear-to-moment ratio are smaller than the experimental, although the average of the deflection ratios is close to unity. This can be seen from the scatter chart by the lack of clustering of deflection ratios around unity. This method does not predict individual deflections accurately.

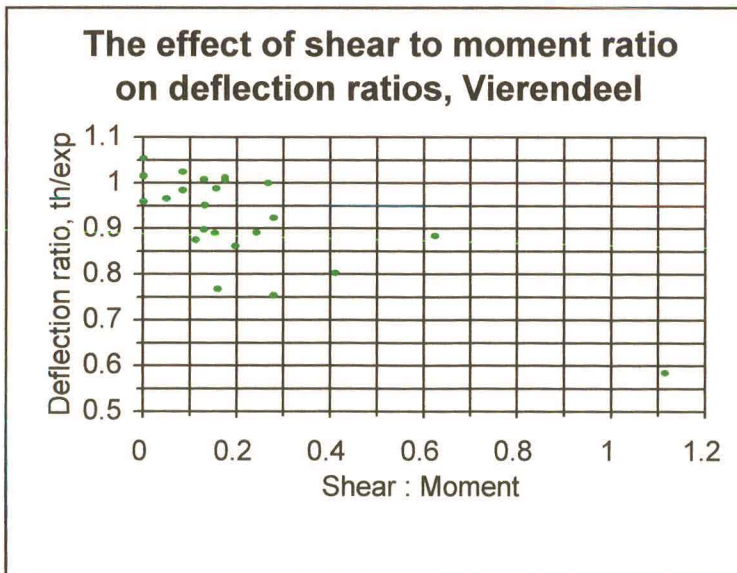


Figure 4.20 : Shear-to-moment and deflection ratios, Vierendeel

The deflection ratios from the Vierendeel method are clustered around unity for the lower shear-to-moment ratios. As with the other methods, the deflection ratios decrease with increasing shear-to-moment ratios, but the agreement between the theoretical and experimental values is good.

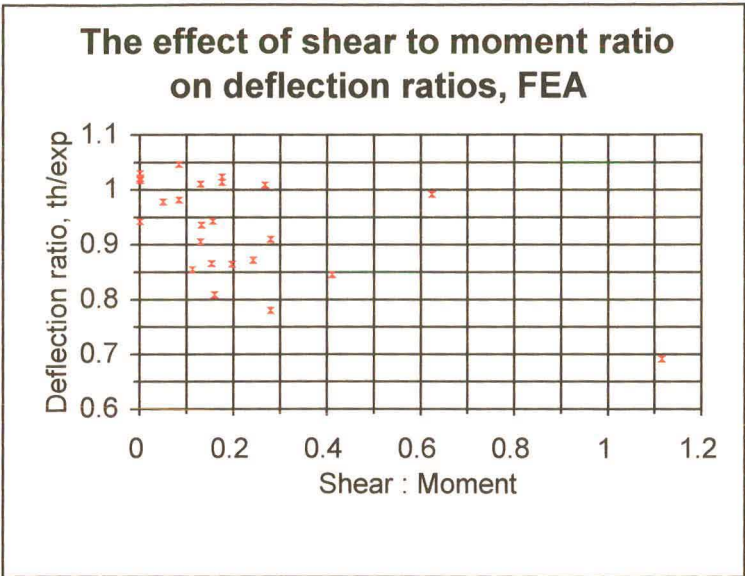


Figure 4.21 : Shear-to-moment and deflection ratios, FEA

Clustering of deflection ratios around unity is seen in this scatter chart, as is a decrease in deflection ratios with an increase in shear-to-moment ratios. As with the Vierendeel method, there is a good agreement between the theoretical and experimental values.

All these observations can be summed up by plotting normal distributions for the deflection ratios. The mean and standard deviation of the deflection ratios was calculated for each theoretical method:

Table 4.1 : Means and standard deviations of deflection ratios

	Mean	Standard deviation
SCI	0,987	0,138
Simplified SCI	0,973	0,163
Vierendeel	0,922	0,099
FEA	0,932	0,087

Ideally the curve would be pointed and centred at unity, which would indicate a small standard deviation and a mean of unity. A flatter curve indicates a large standard deviation.

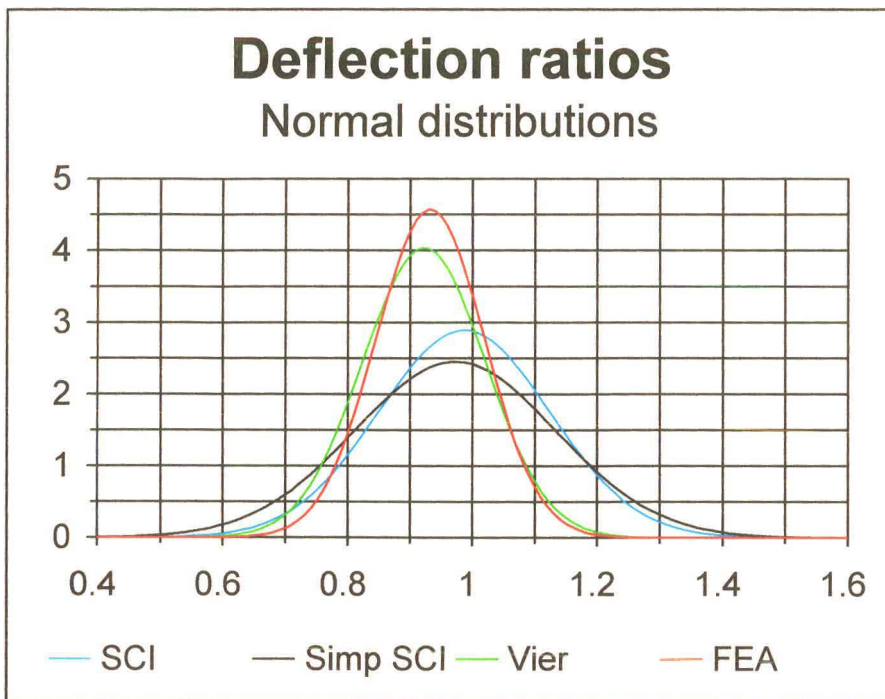


Figure 4.22 : Deflection ratios normal distributions.

As can be seen from Figure 4.22, the SCI and simplified SCI methods have flatter curves centred close to unity, whereas the FEA and Vierendeel methods have more pointed curves which have a mean less than unity.

A large standard deviation indicates that deflections are either being overestimated or underestimated, and that very few are actually correctly calculated, as with the simplified SCI method.

A mean less than unity is an easier problem to correct than a large standard deviation.

A factor of $\frac{1}{\text{mean}}$ could be applied to all the deflections which would bring the mean up to unity.

All the deflection ratios were multiplied by the reciprocal of their mean and the normal distributions replotted, as in Figure 4.23.

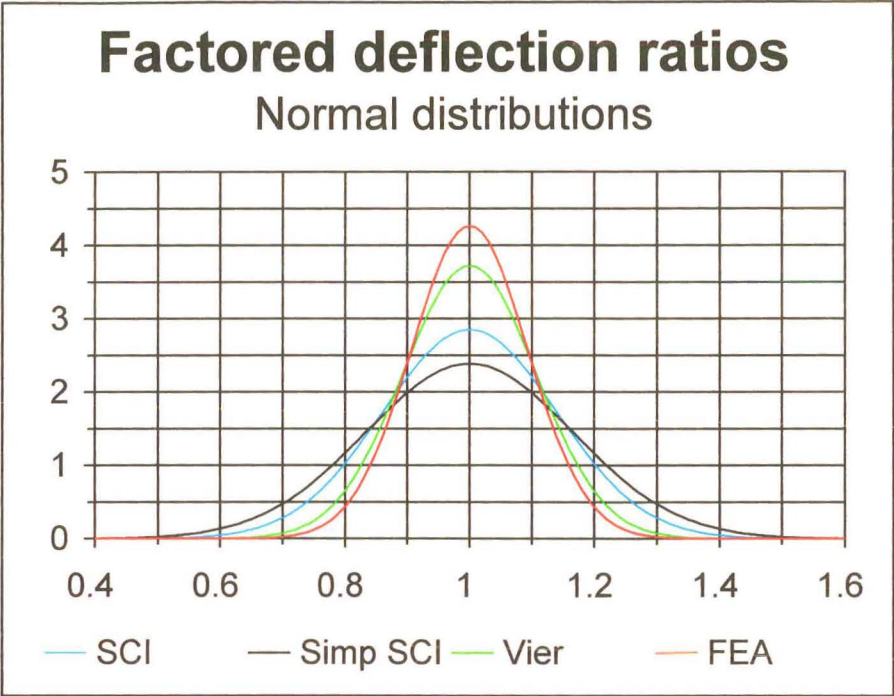


Figure 4.23 : Factored deflection ratios, normal distributions

It can be seen from Figure 4.23 that the finite element method is the most accurate, followed by the Vierendeel method, the SCI method and the simplified SCI method. The finite element method is time consuming and would therefore not be the best method to use in practise. The Vierendeel method is not complicated and it would be a viable option for calculating deflections of cellular beams in practice.

CHAPTER 5

CONCLUSIONS

5.1 Introduction

This investigation set out to find an accurate, practical method of predicting failure loads, failure modes and deflections of cellular beams. Eight full-sized cellular beams were tested to destruction and the results compared with the theory.

Two criteria were used in assessing the suitability of the theoretical method to use in practice:

- (i) Accuracy
- (ii) Practicality for use in a design office.

5.2 Experimental Work

Vierendeel failure occurred in the opening with the highest combined shear and moment for test beams 1, 2 and 3 for both the mid span and third point load cases. Beam 4A (mid span load) failed in pure bending and Beam 4B (third point loads) failed in lateral torsional buckling at a load close to the plastic failure load.

Beams subjected to pure bending are most susceptible to lateral torsional buckling⁵. This explains why buckling tended to be a problem in beams loaded at the third points. It was found that lateral restraints were needed at frequent intervals along the length of the beam.

The failure loads are given in section 2.6.

5.3 Ultimate Load Behaviour

Both the failure loads and failure modes were considered for ultimate load behaviour.

The SCI method is very conservative. It predicted Vierendeel failure for all beams at loads averaging only 76% of the experimental failure loads. This was considered to be over-conservative and as such the SCI method does not meet the accuracy criterion.

The plastic vierendeel spreadsheet method (which was derived from the computer program) was unconservative and as such does not meet the accuracy criterion for the failure loads. Vierendeel failure was predicted for all beams subject to mid span loading and pure bending failure for all beams subjected to third point loading. These predictions were only correct for three beams, viz. beams 1A, 2A and 3A.

The plastic Vierendeel design chart method predicted individual failure loads most accurately. The design charts predicted Vierendeel failure for all test beams, which was correct for beams 1, 2 and 3 for both mid span and third point load cases. Beam 4A failed in a pure bending fashion and from the design charts in section 3.4.1.3, it can be seen that the beam line lies closer to the moment axis than the beam lines for the other test beams. The design charts are quick and simple to use and can be used with any load case, unlike the spreadsheet. The design charts would be a viable option for use in a design office.

The finite element method was also unconservative. Failure modes are not predicted by the finite element method. This method would be impractical for use in the design office as it is very time consuming.

The computer program and the spreadsheet were designed to handle simply supported beams with point loads at mid span or at the third points. The design charts which are also based on the plastic Vierendeel method can be used for any combination of internal shear and bending moment. This enables them to be used for beams with different end conditions, continuous beams or beams with loading other than mid span or third point loads. The finite element analysis can be used for any end conditions and loading.

5.4 Deflections

The SCI method does not predict individual results accurately, although the mean of the deflection ratios (theoretical value to experimental value) is close to unity, it has a large standard deviation.

The simplified method proposed by the SCI has an even greater standard deviation though the mean of the deflection ratios lies close to one. These two methods fail on the accuracy criterion.

The finite element method was the most accurate method but it is not practical to use in a design office due to the length of time taken for an analysis. This method fails on the practicality criterion.

The Vierendeel method of calculating deflections developed for this investigation was the second most accurate method. The Vierendeel method sums the deflections due to the primary bending and the secondary Vierendeel bending. This method is simpler and not as time consuming as either the SCI or finite element methods and therefore is the best method judged by both the accuracy and practicality criteria.

5.5 Summary

A series of experimental tests was carried out and failure loads, failure modes and deflections were obtained for eight test beams.

The plastic Vierendeel design chart method was found to be the most accurate and practical method of calculating failure loads and predicting failure modes.

The Vierendeel deflection method was found to be the most accurate and practical method of calculating deflections.

5.6 Future work

This investigation dealt with plastic failure of straight, non-composite, symmetrical cellular beams. There is scope for further work investigating the behaviour of cellular beams which are curved, composite or asymmetric.

CHAPTER 6

REFERENCES

1. Trinchero, Paolo E. *Serviceability Limit States of Composite Beams*, MSc Thesis, University of the Witwatersrand, Appendix A, pp A.6 - A.7, 1993
2. Neubert, H.K.P., *Strain gauges, Kinds and Uses*, Macmillan, London, 1967.
3. Window, A.L. and Holister, G.S., *Strain Gauge Technology*, Applied Science publishers, London, 1982.
4. Redwood, RG and McCutcheon, JO Beam Tests with Unreinforced Web Openings. *Journal of the Structural Division, Proceedings of the American Society of Civil Engineers*, January 1968, pp1-17.
5. Nethercot, DA and Kerdal, D Lateral-torsional Buckling of Castellated Beams. *The Structural Engineer*, Volume 60B, No 3, September 1982, pp53-61.
6. Maalek, S and Burdekin, FM Weld Quality Requirements for Castellated Beams. *The Structural Engineer*, Volume 69, No 13, 2 July 1991, pp243-254.
7. Hosain, MU and Speirs, WG Experiments on Castellated Steel Beams. *Welding Research Supplement*, August 1973, pp329-342.
8. Okubo, T and Nethercot, DA Web post strength in castellated steel beams. *Procedures of the Institute of Civil Engineers*, Part 2, 1985, 79, September, pp533-557.
9. Westok. Cellular Beams. Information and beam section properties brochure, January 1993
10. Ward, JK. Design of Composite and Non-Composite Cellular Beams. SCI publication 100. The Steel Construction Institute, 1990.
11. Dougherty, B K. Castellated Beams: A state of the art report. *South African Institute of Civil Engineers Journal*, Second Quarter 1993, pp 12-20.
12. Redwood, RG Design of beams with web holes. *Canadian Steel Industries Construction Council, Ontario, Canada*, 1973.
13. Dougherty, BK. Ultimate load tests on beams with rectangular web openings. *Struct Engr*, Vol 58, No 3, Sept 1980.
14. Westok. Cellular Beams. Information and beam section properties brochure, July 1997

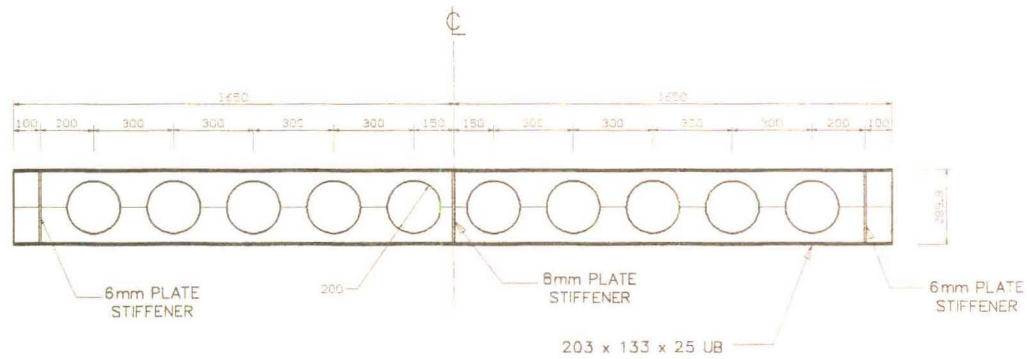
15. Ravinger, J and Laščeková, P. Experimental Verification of Thin-walled Girders with Circular Holes. *Journal of Constructional Steel Research* 0143-974X, 1989, pp301-316

CHAPTER 7

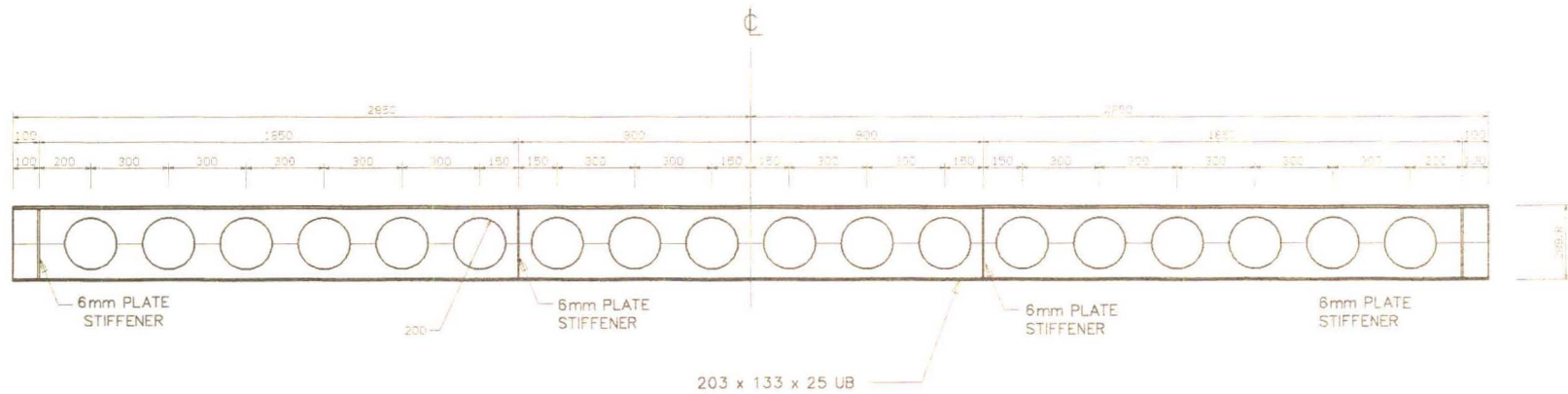
APPENDICES

A1 - Laboratory Tests

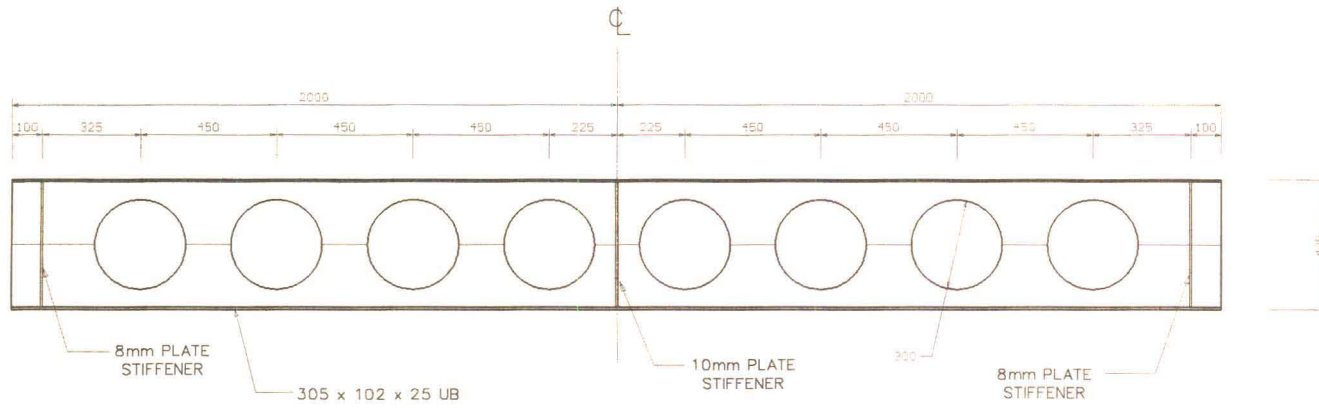
Detailed drawings of the test beams.



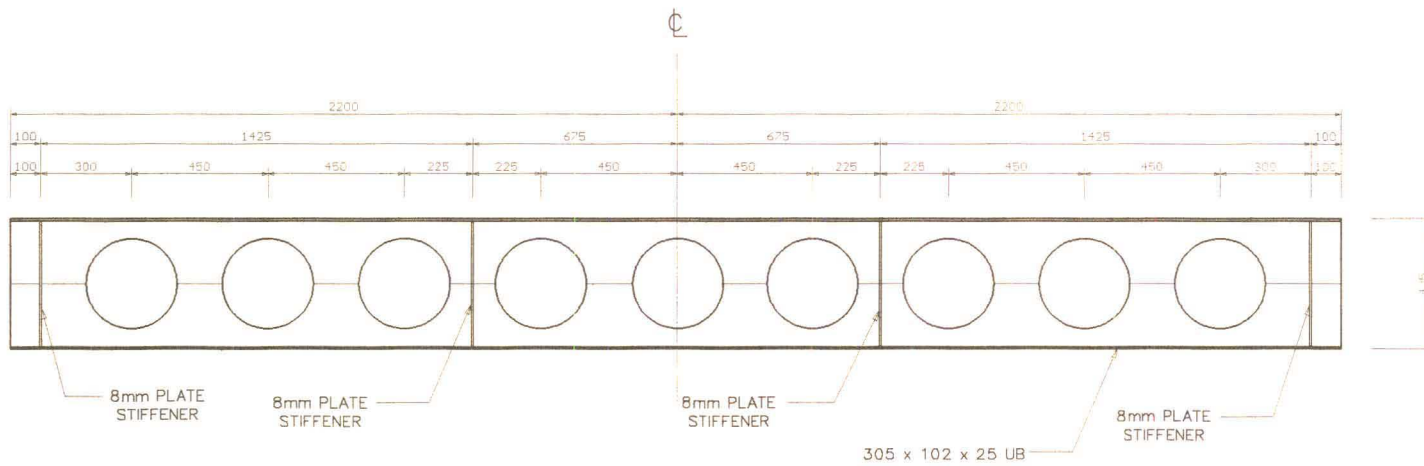
BEAM 1A



BEAM 1B




BEAM 3A





BEAM 3B

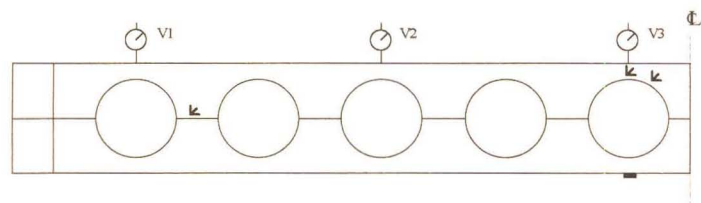
Positions of strain gauges and dial gauges

Key

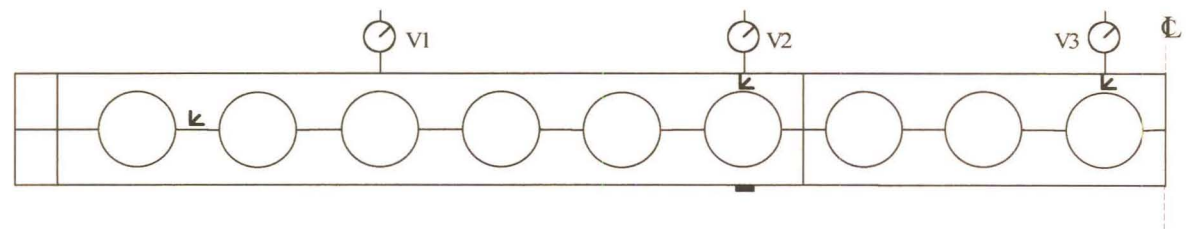
 Strain gauge rosette

 Dial gauge

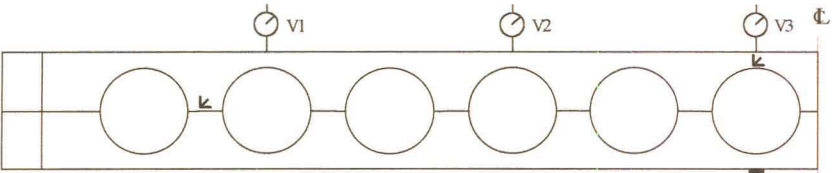
 Three straight strain gauges



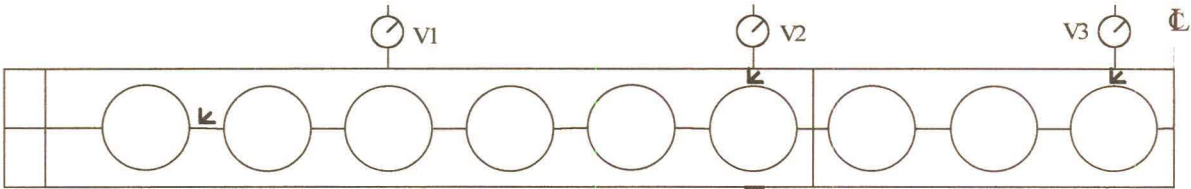
Beam 1A



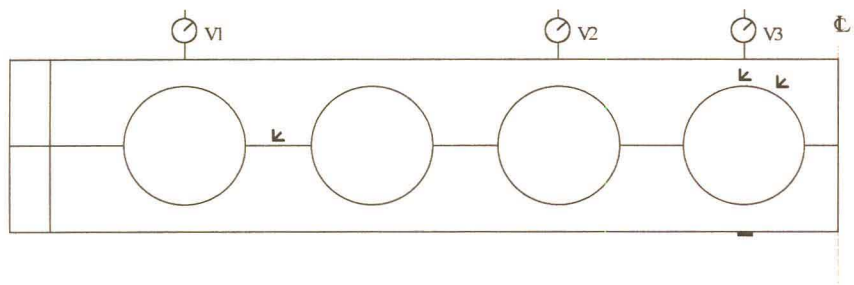
Beam 1B



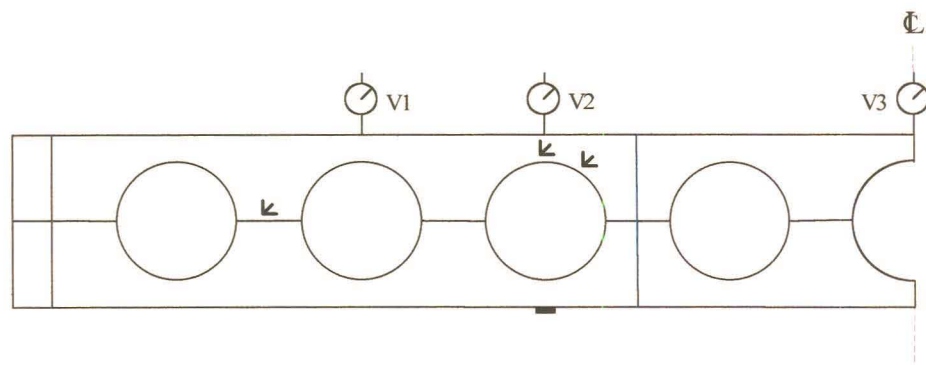
Beam 2A



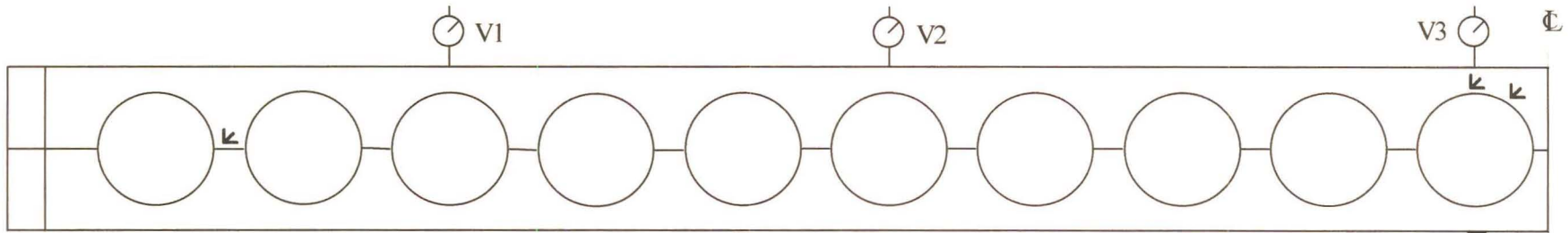
Beam 2B



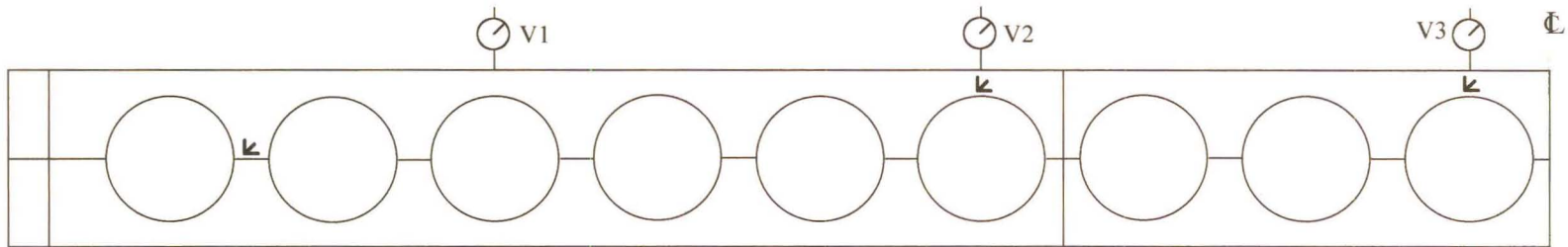
Beam 3A



Beam 3B

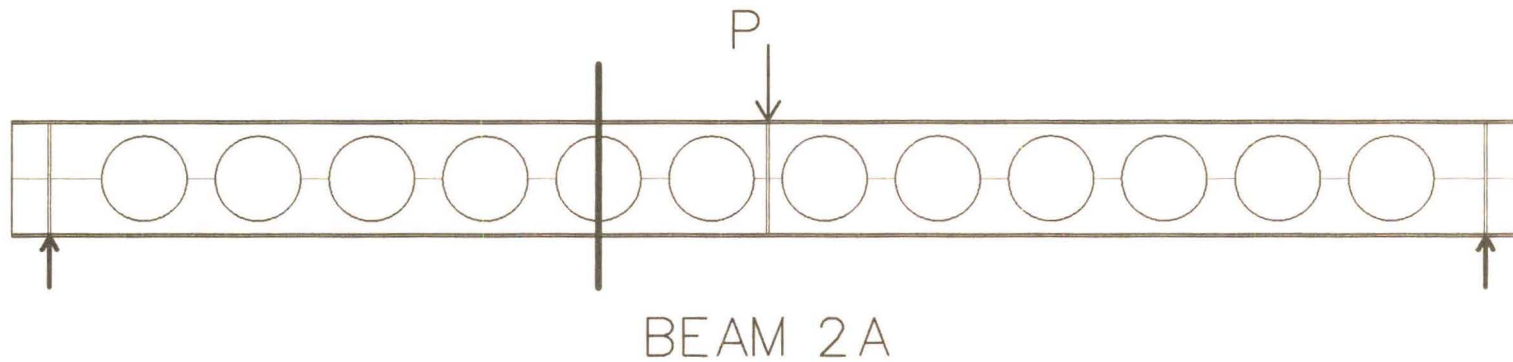
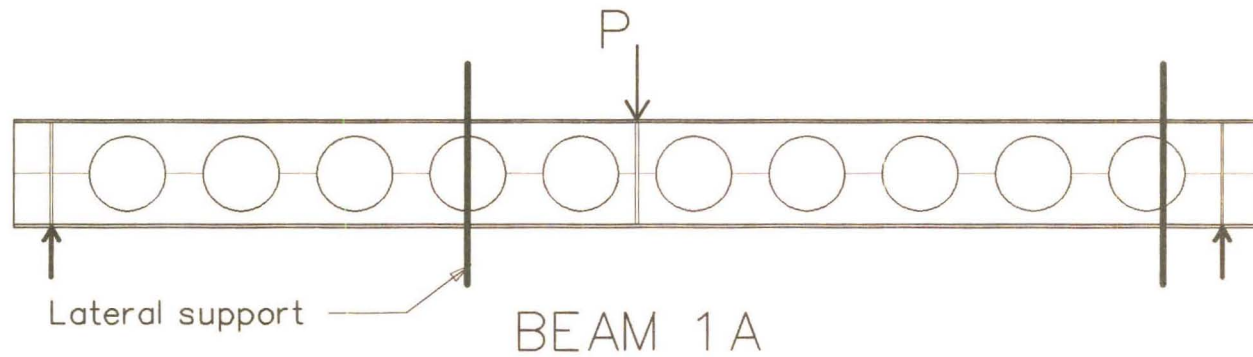


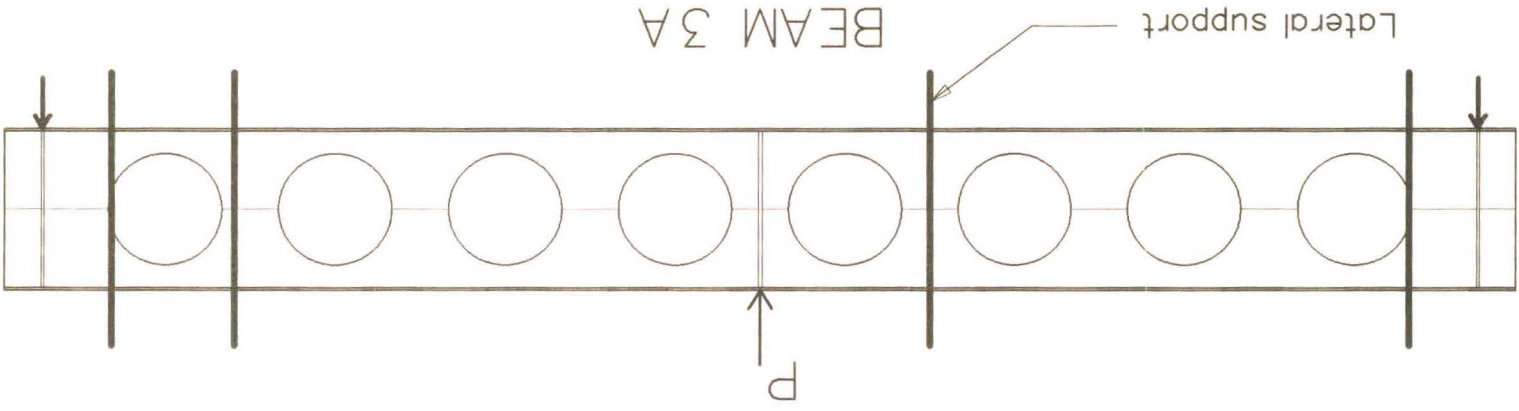
Beam 4A



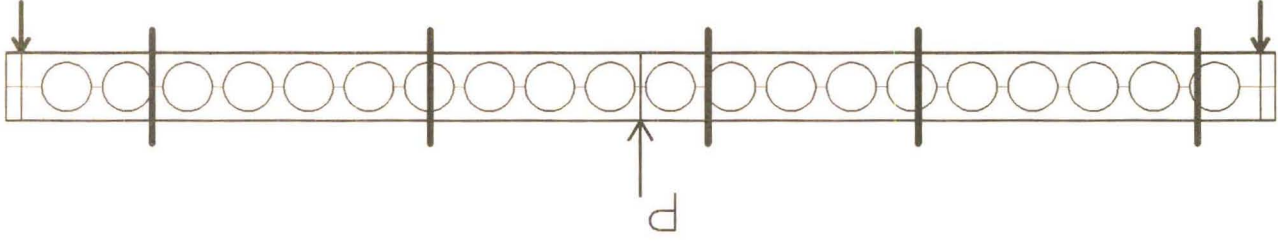
Beam 4B

Loading and lateral support layout
Beams with midpoint loading



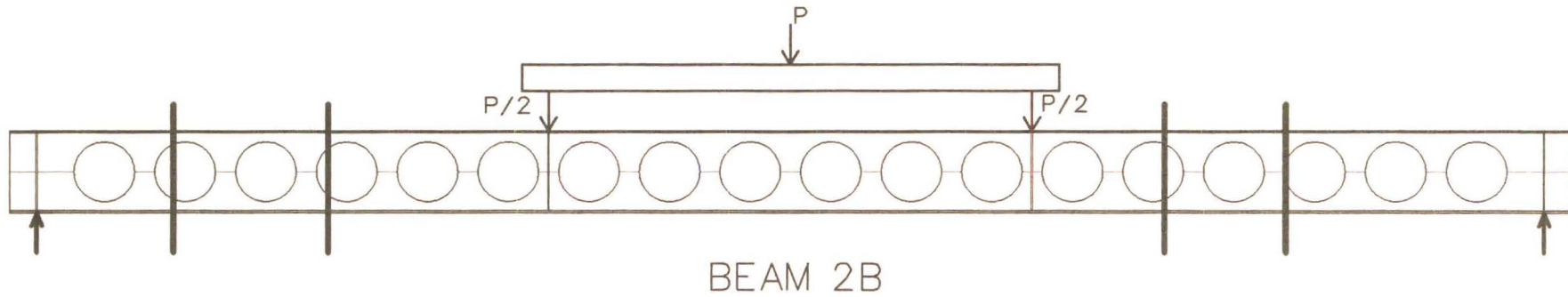
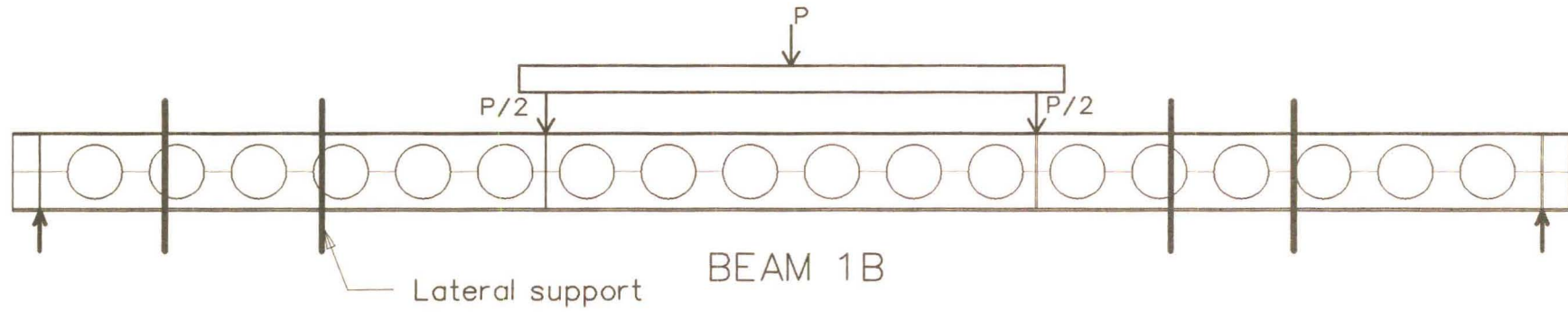


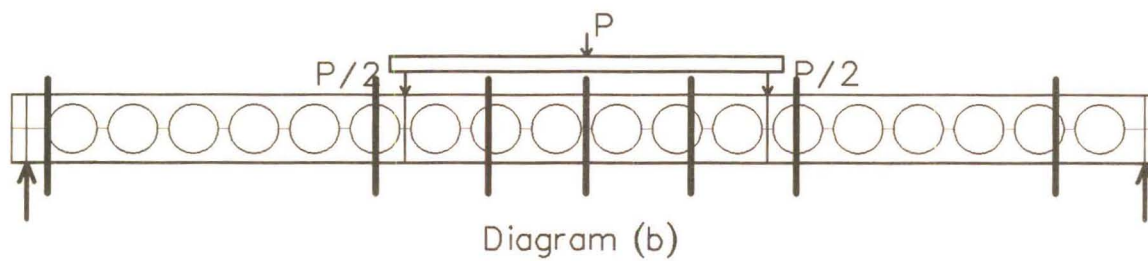
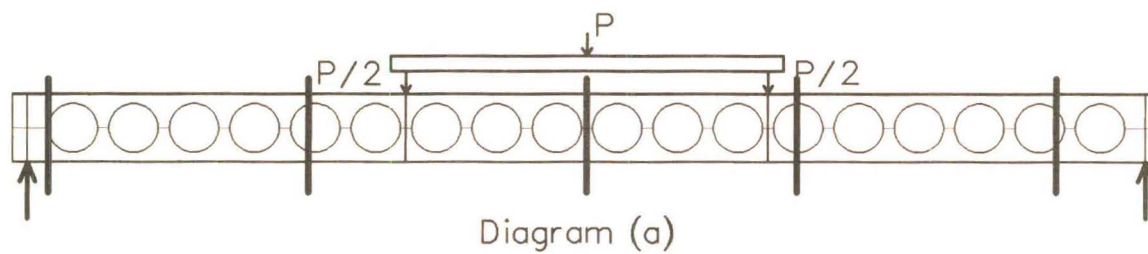
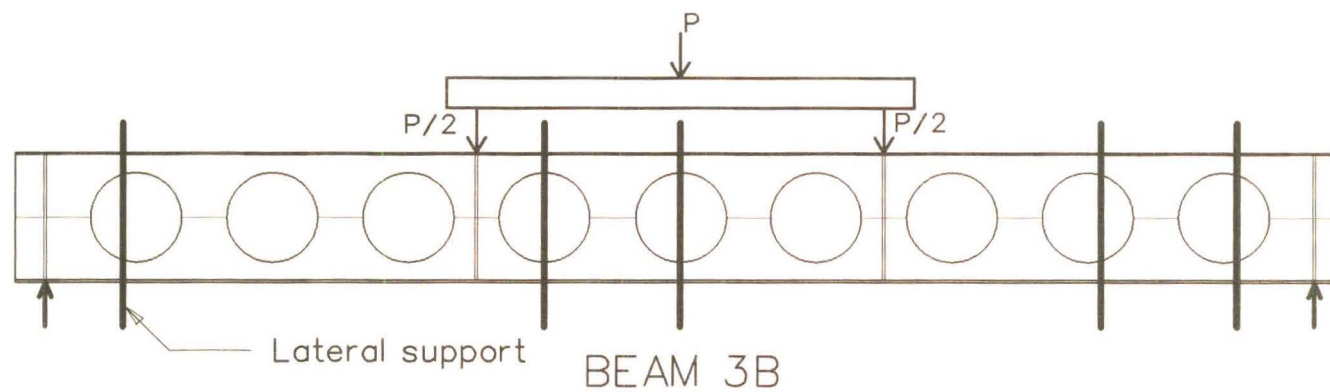
BEAM 3 A



BEAM 4 A

Loading and lateral support layout
Beams with thirdpoint loading





BEAM 4B

Appendix A2 - Ultimate load behaviour

Stress strain curves used for FEA material properties ¹

Steel stress vs strain curves are plotted for SF and SP in Figs.A.3 & A.4.

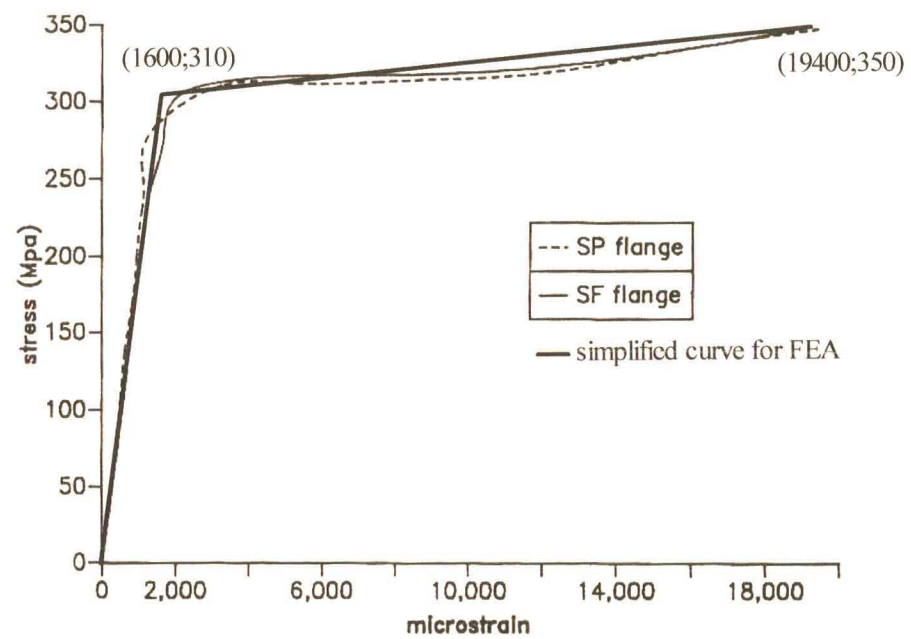


FIG.A.3. - Stress vs strain of flange, specimen SF & SP

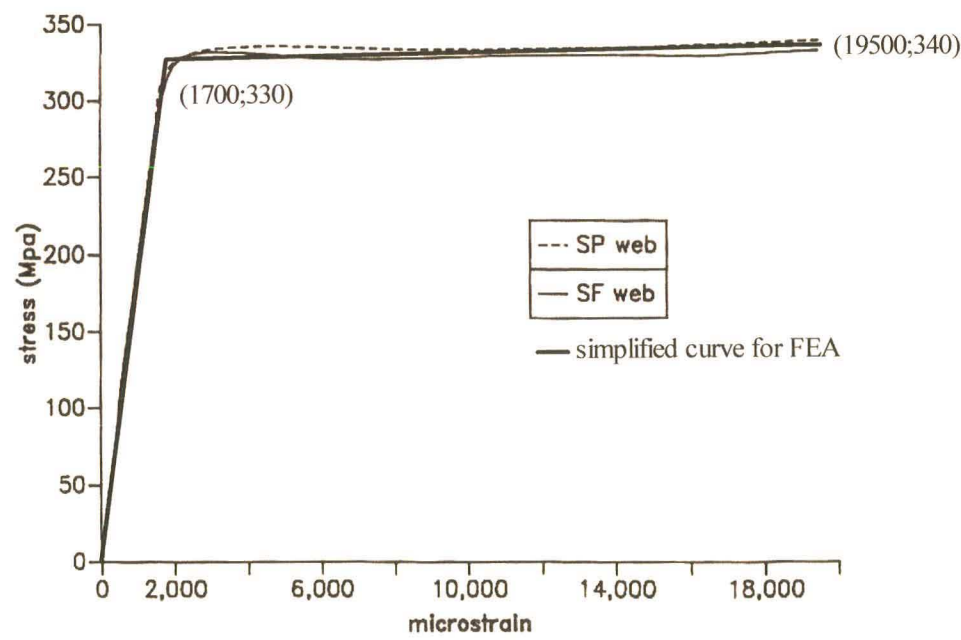
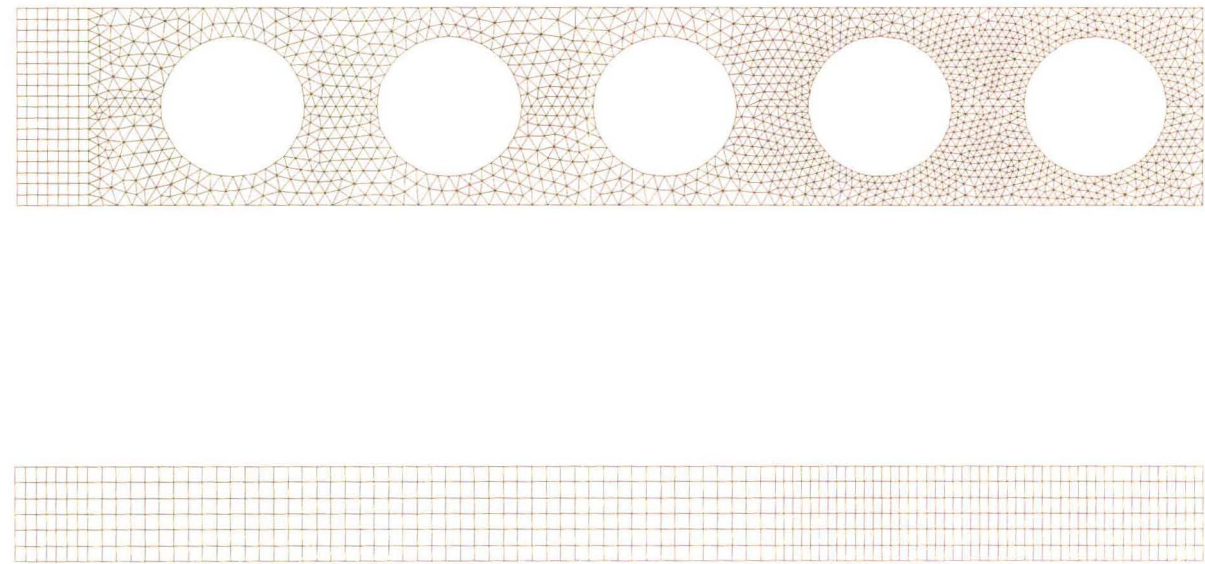
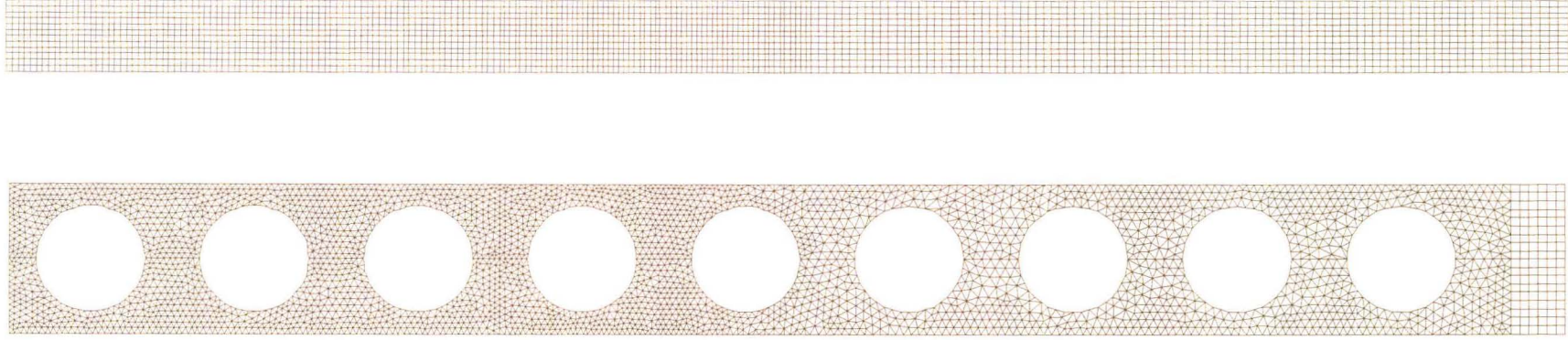


FIG.A.4. - Stress vs strain of web, specimen SF & SP

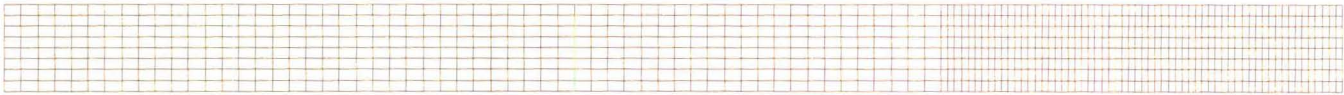
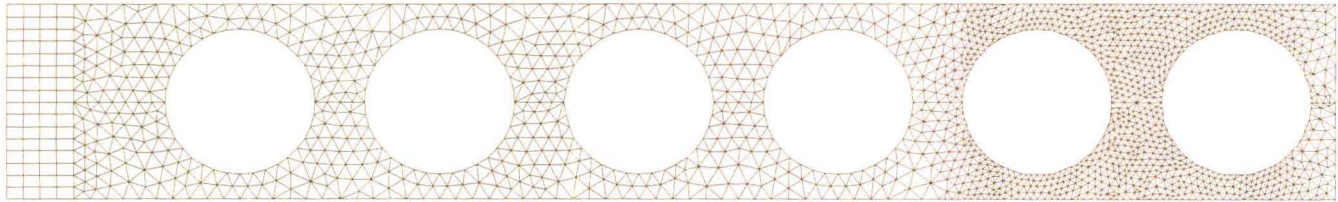
Finite Element Mesh

Beam 1A

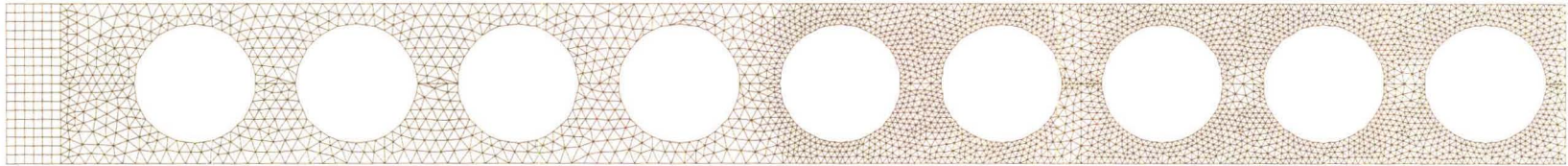




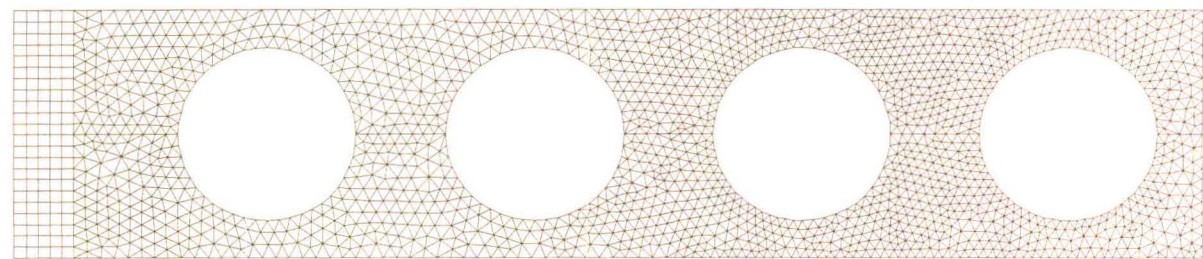
Beam 2A



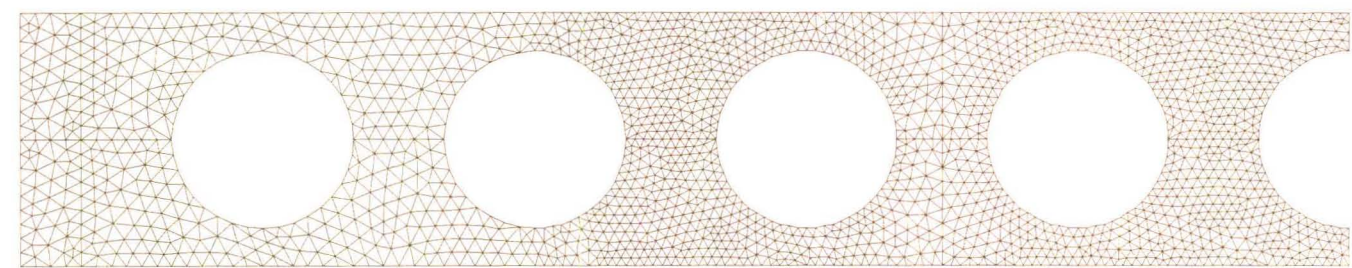
Beam 2B



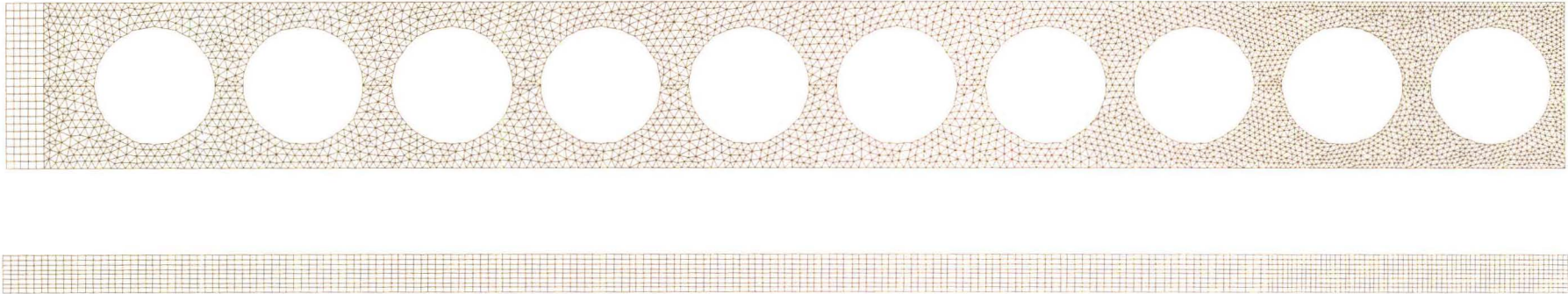
Beam 3A



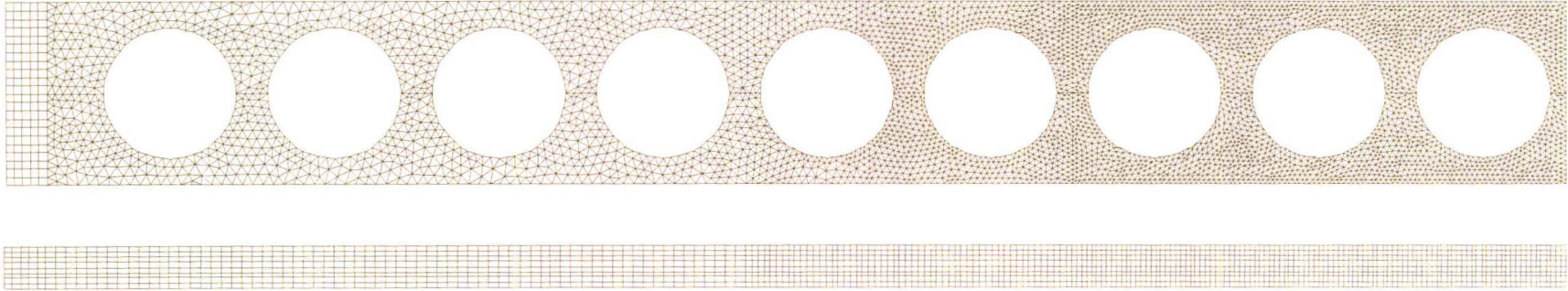
Beam 3B



Beam 4A

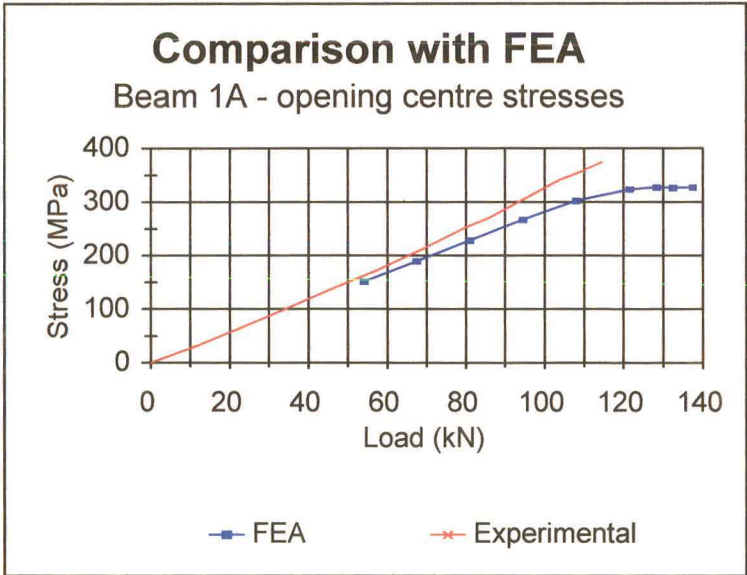
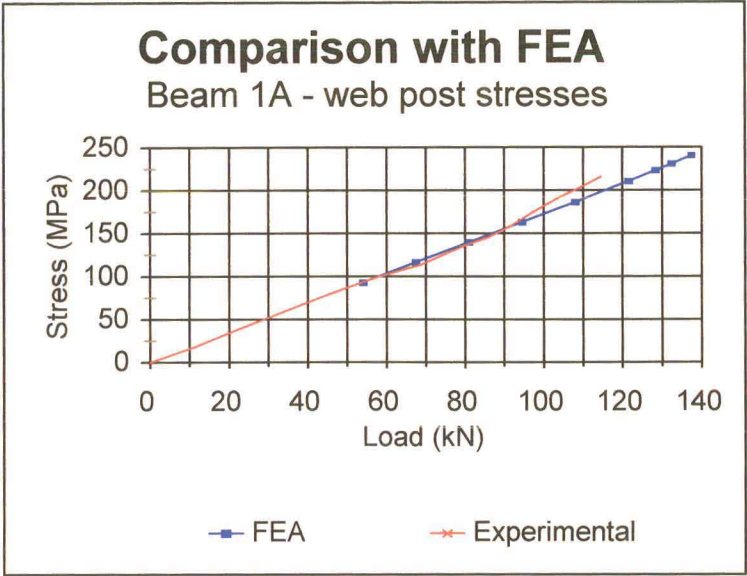


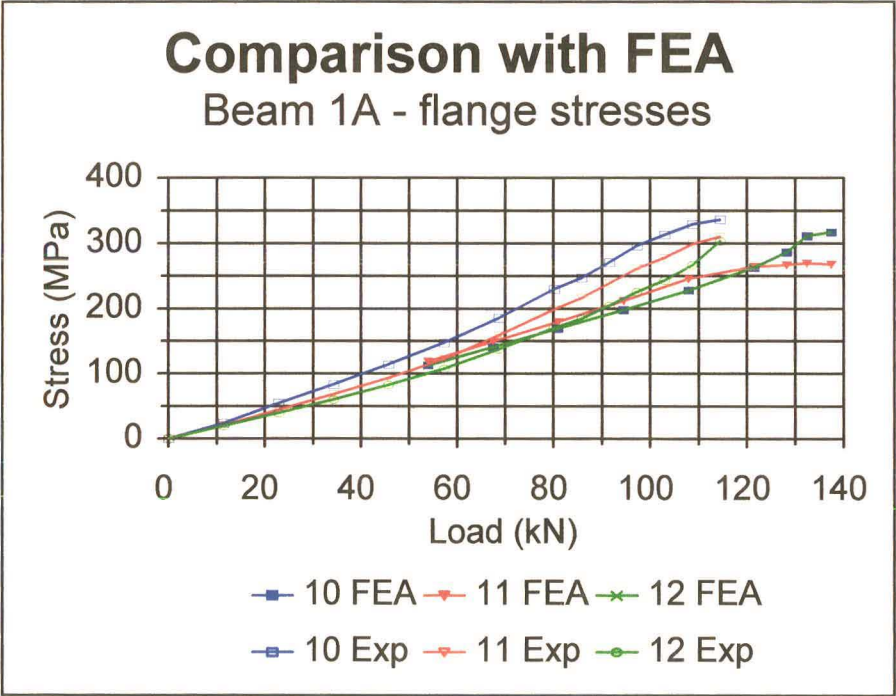
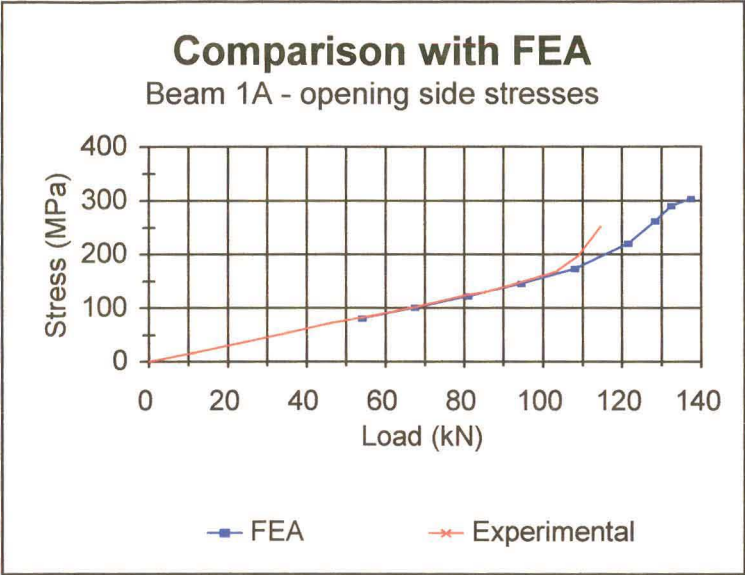
Beam 4B



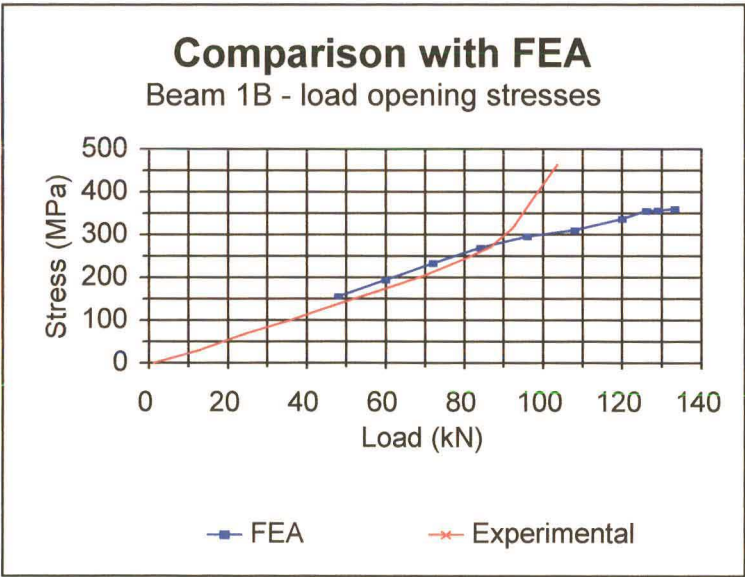
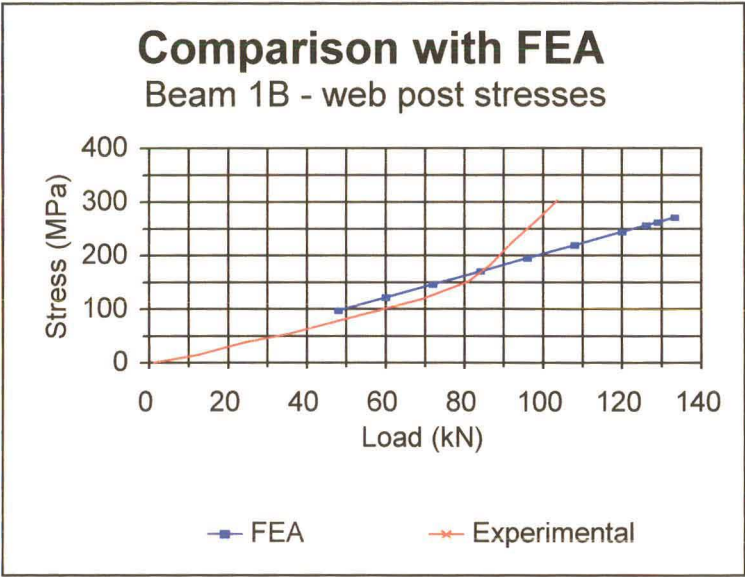
Graphical comparisons between theoretical and experimental stresses

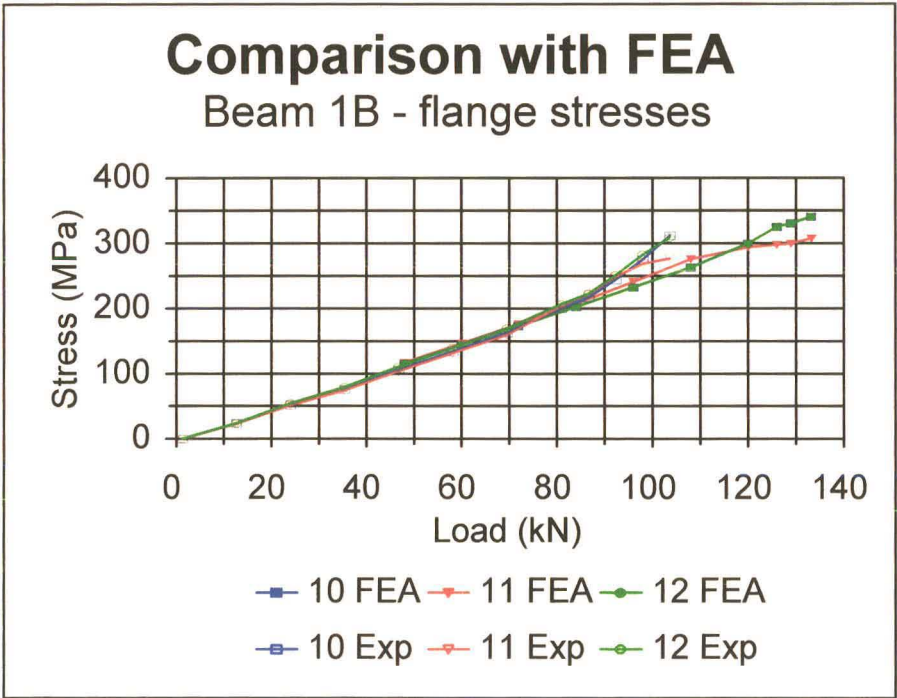
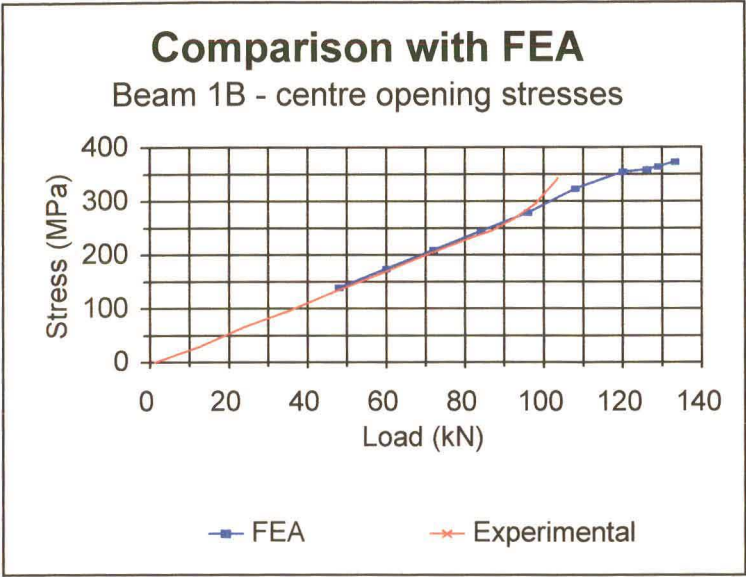
Beam 1A



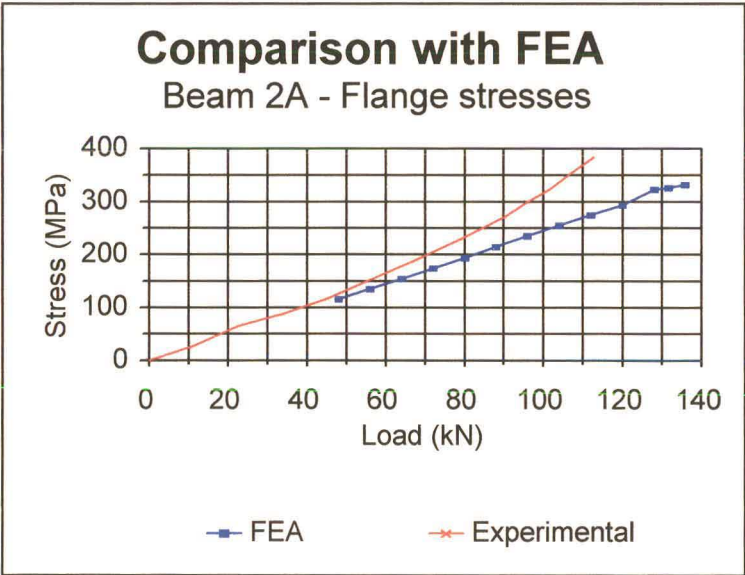
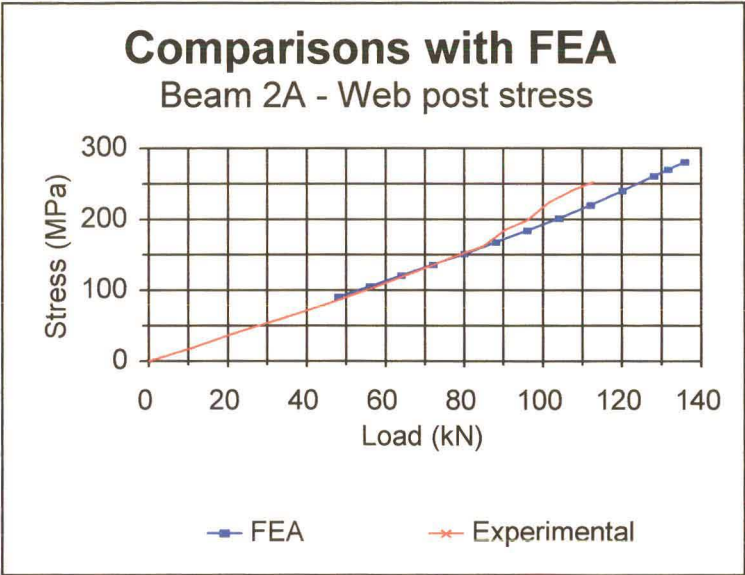


Beam 1B

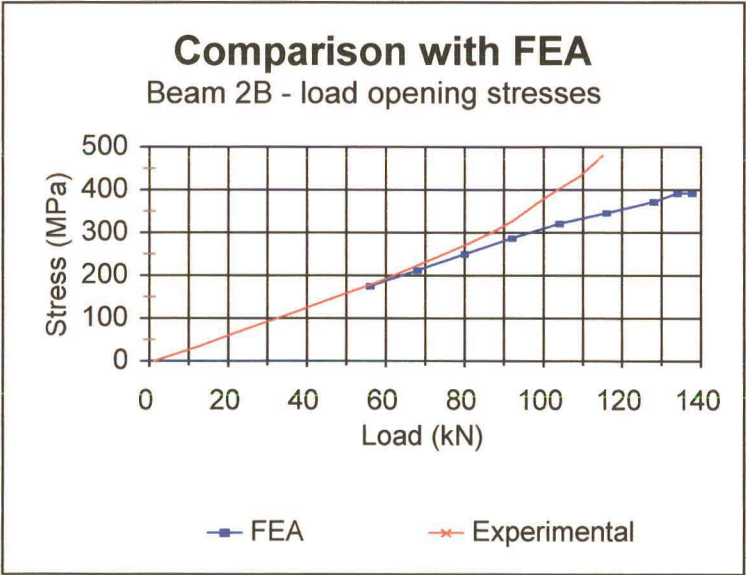
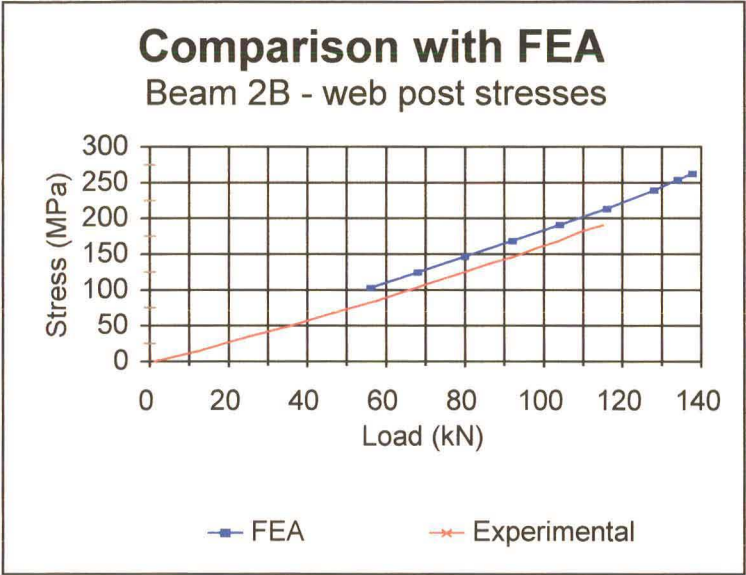


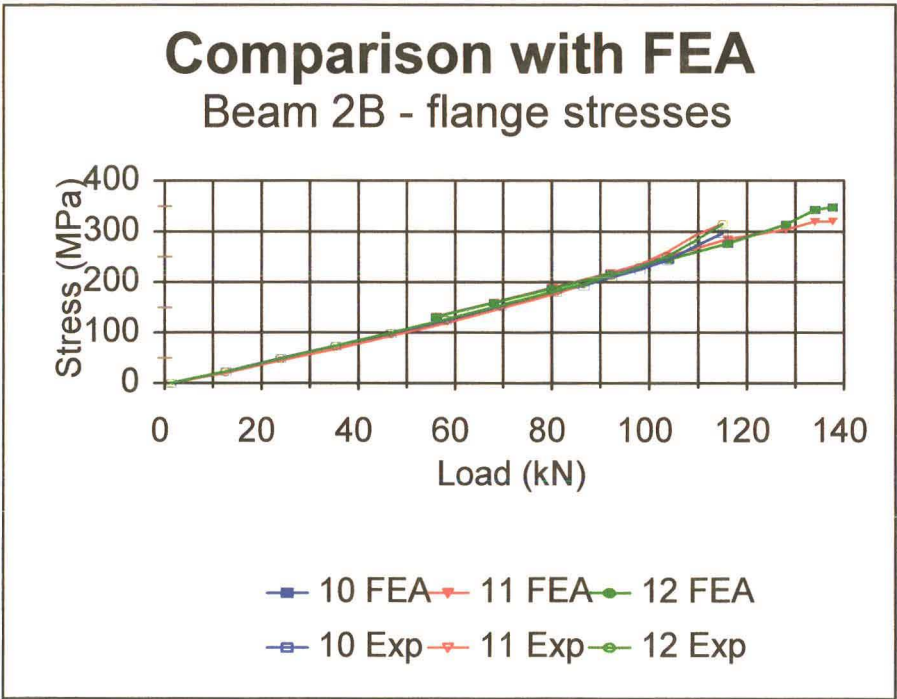
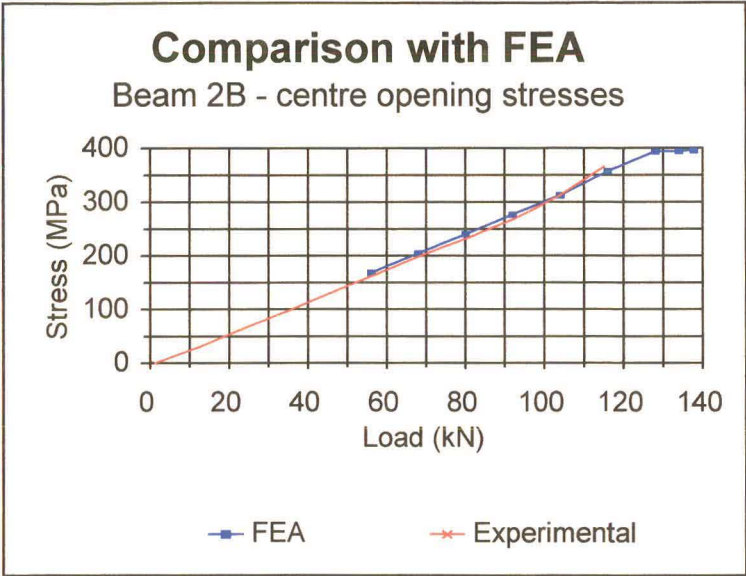


Beam 2A

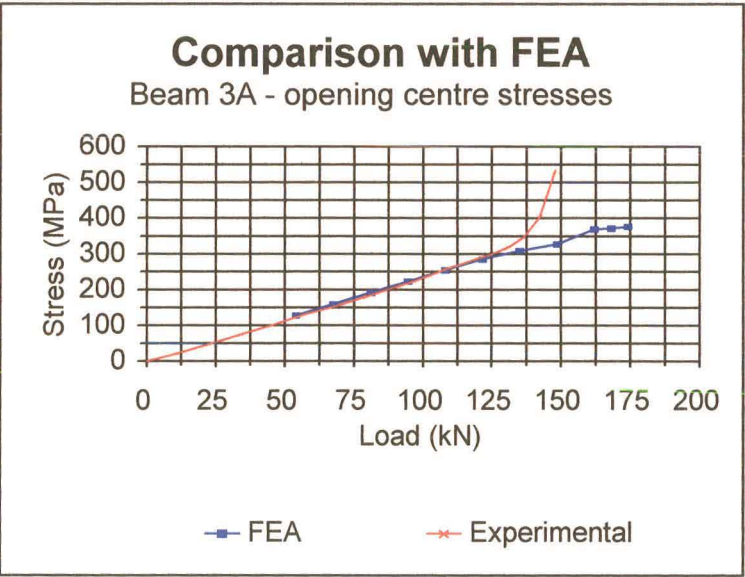
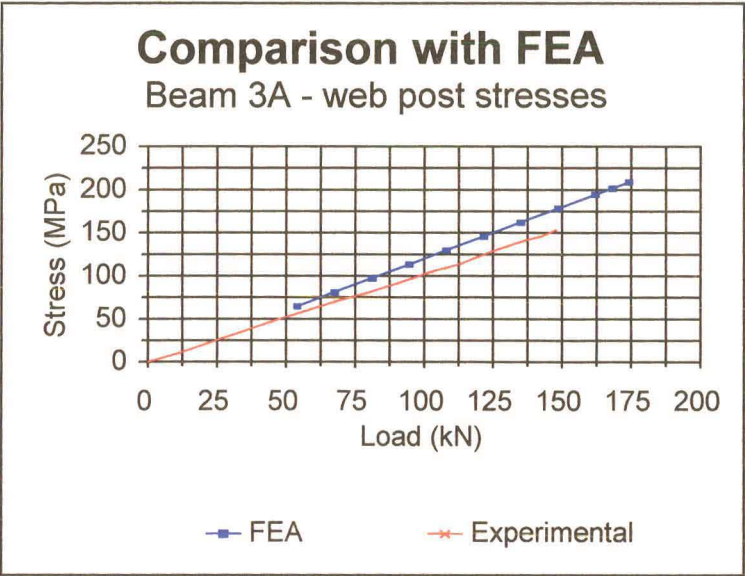


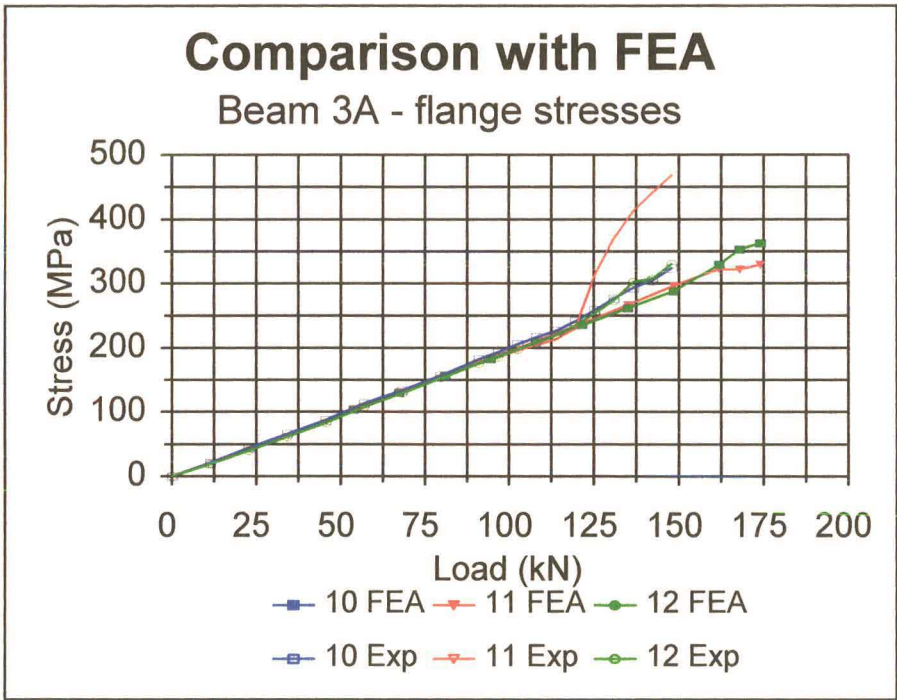
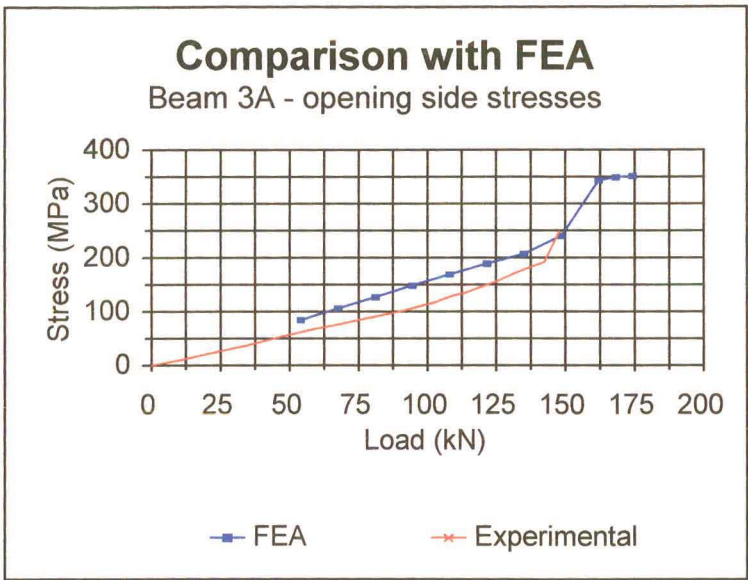
Beam 2B



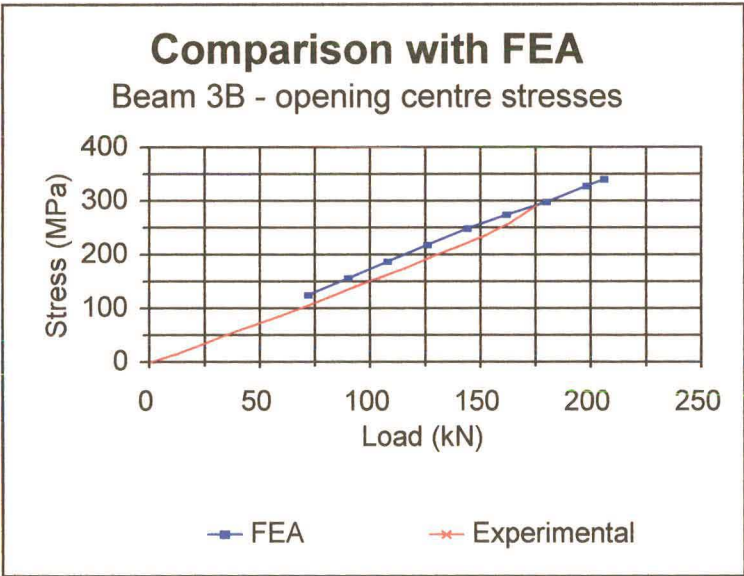
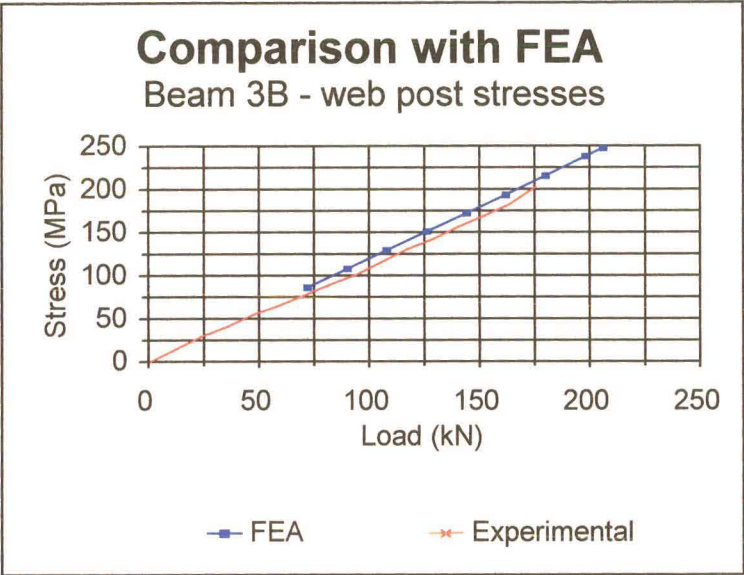


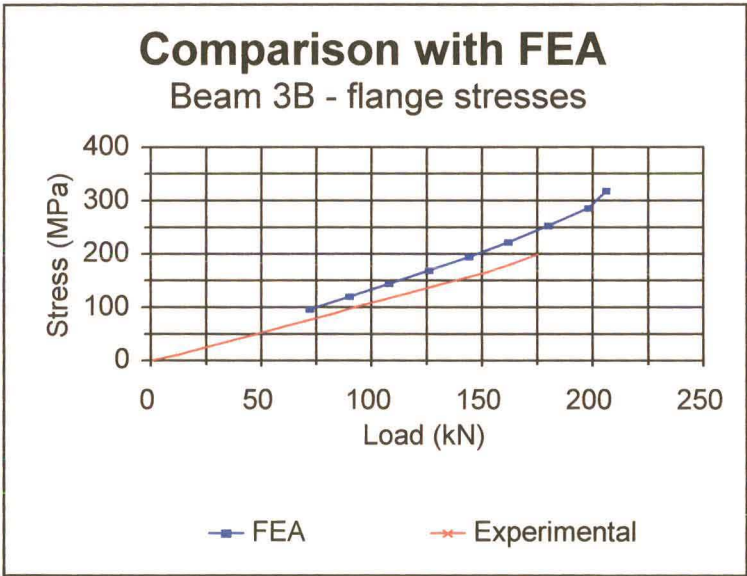
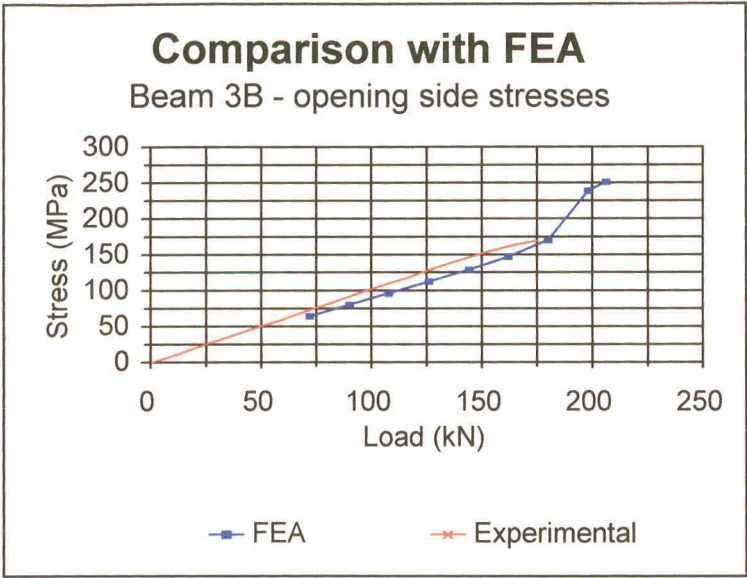
Beam 3A



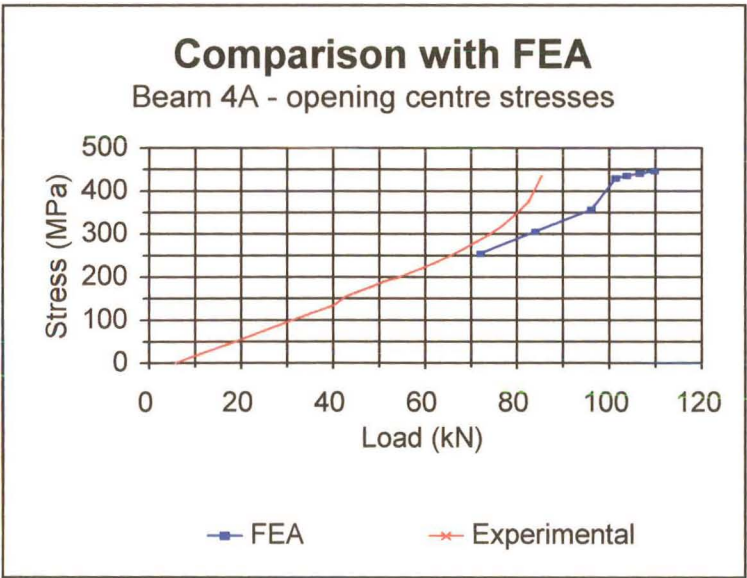
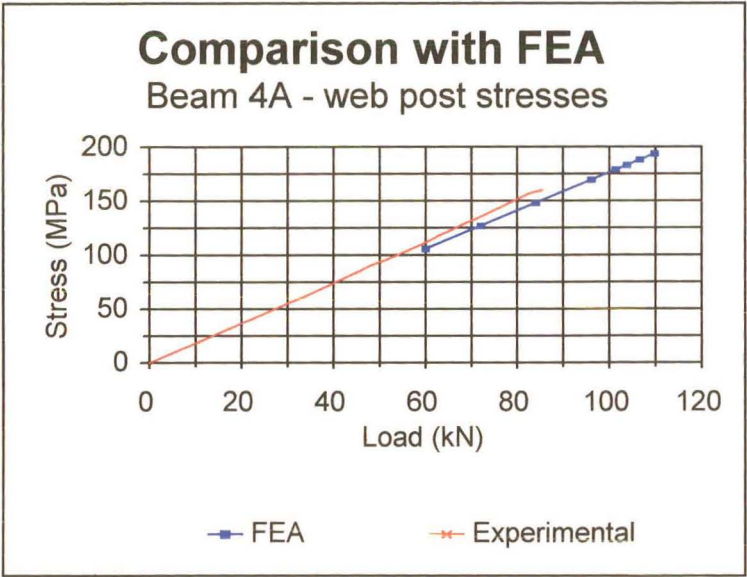


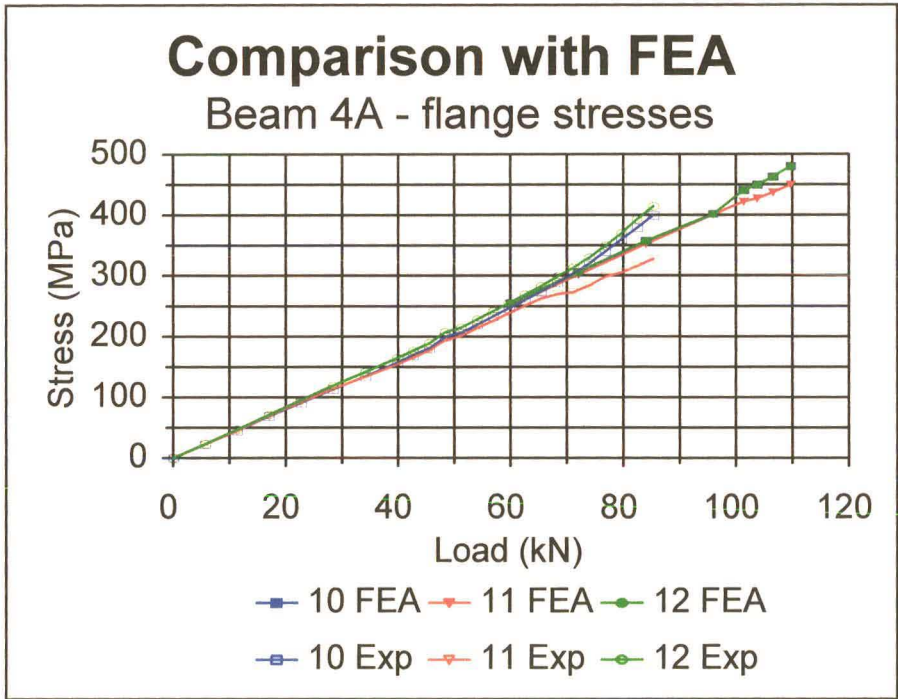
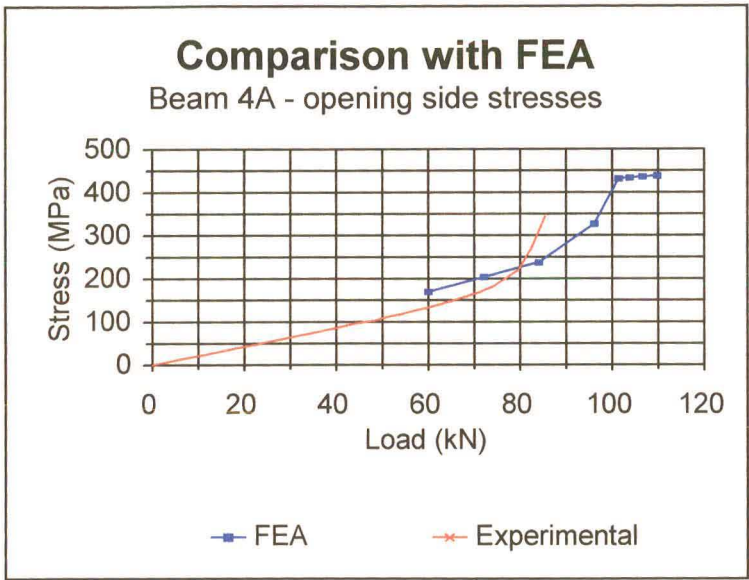
Beam 3B



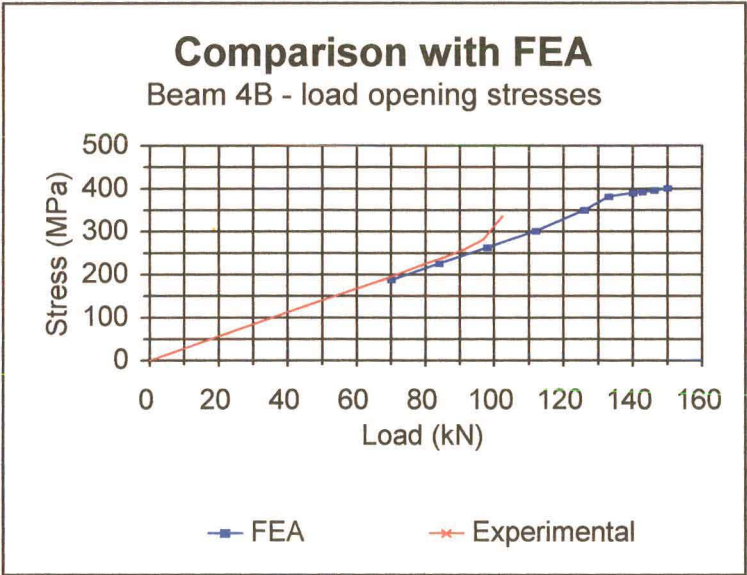
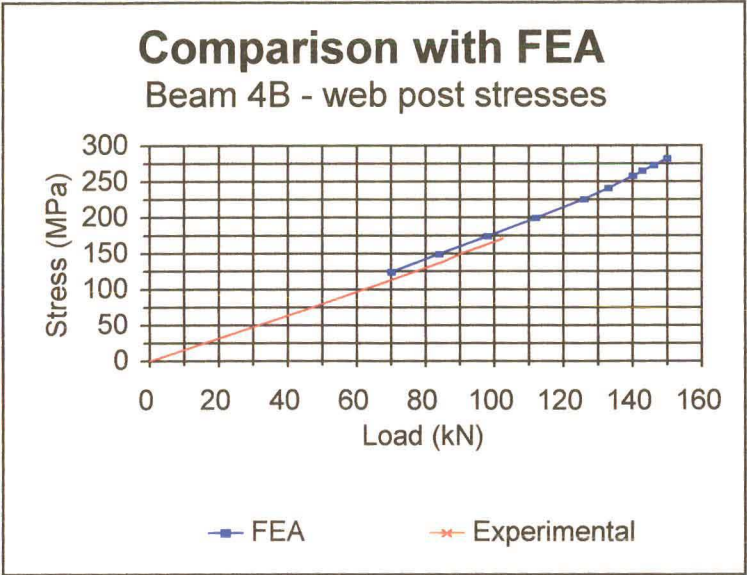


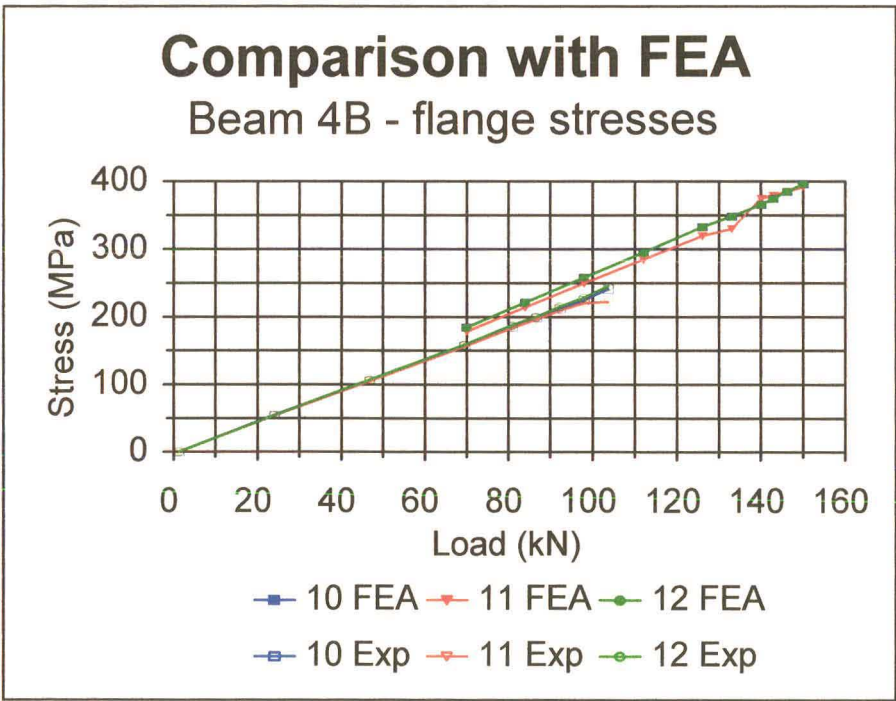
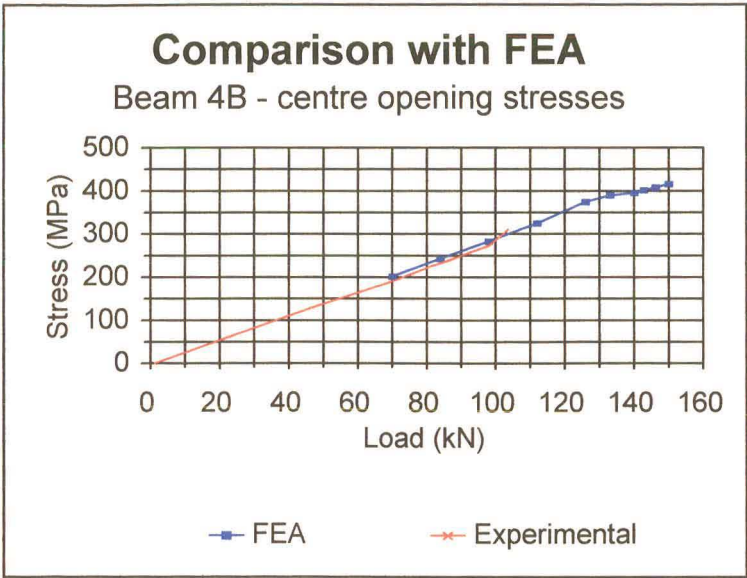
Beam 4A





Beam 4B

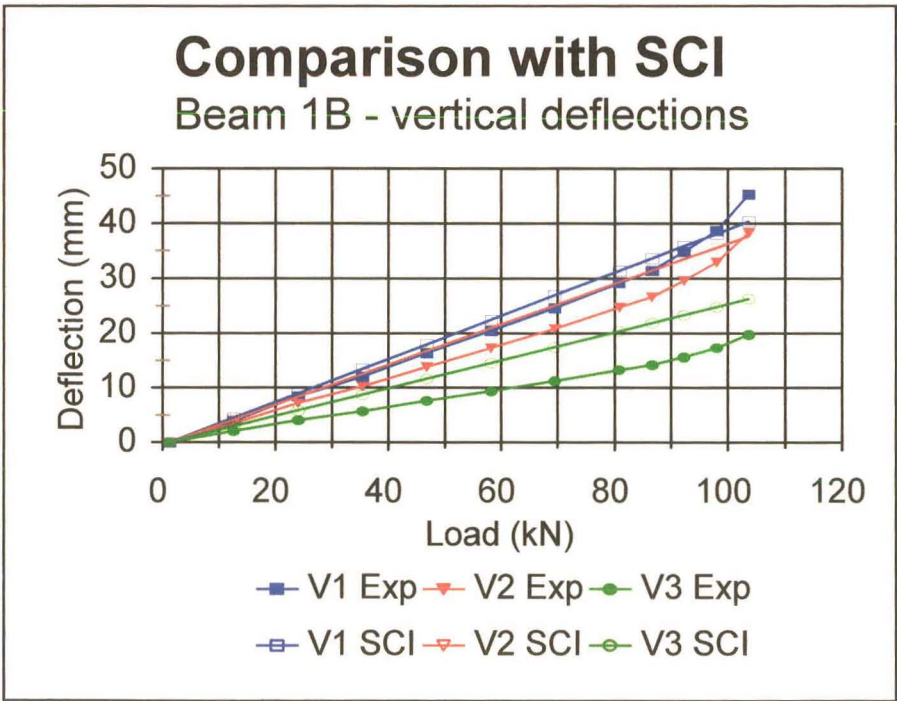
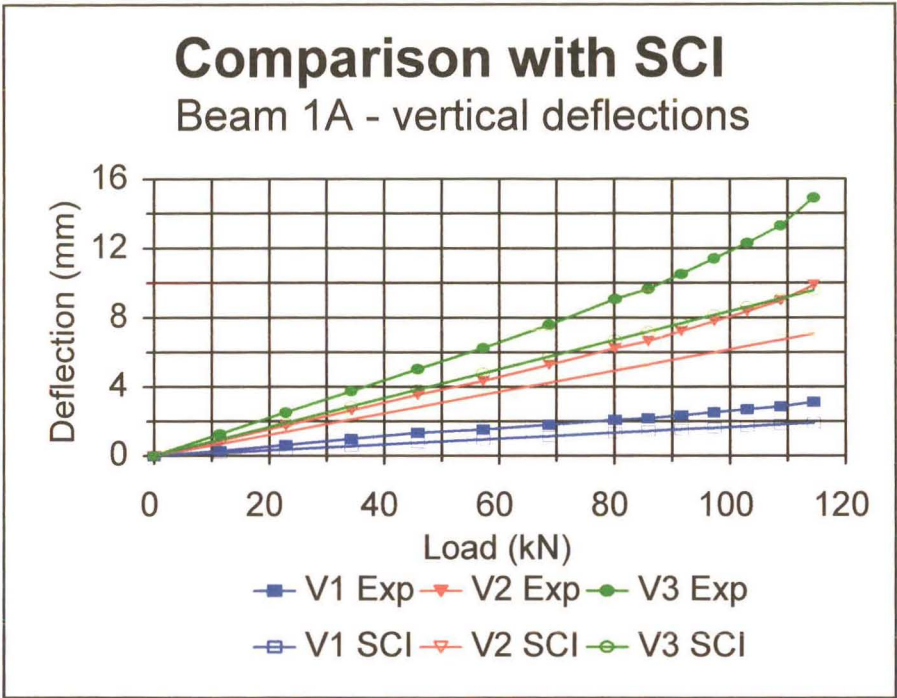




Appendix A3 - Deflections

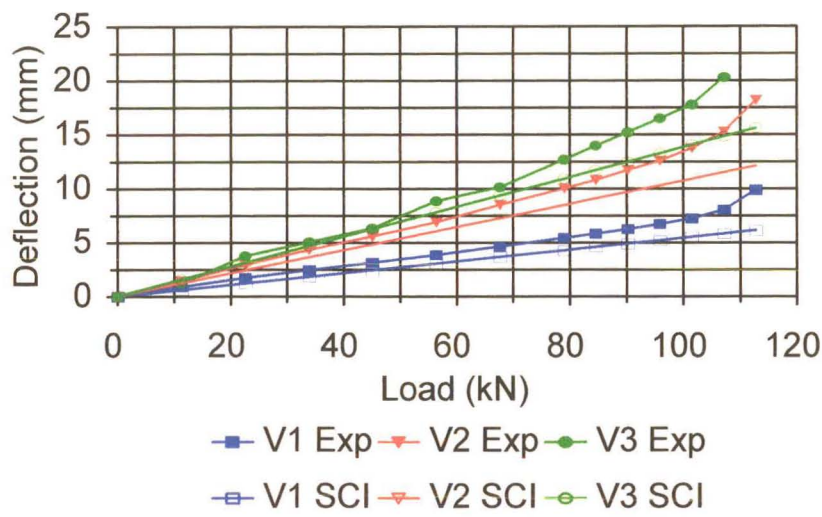
Graphical comparisons between theoretical and experimental results

Steel Construction Institute method



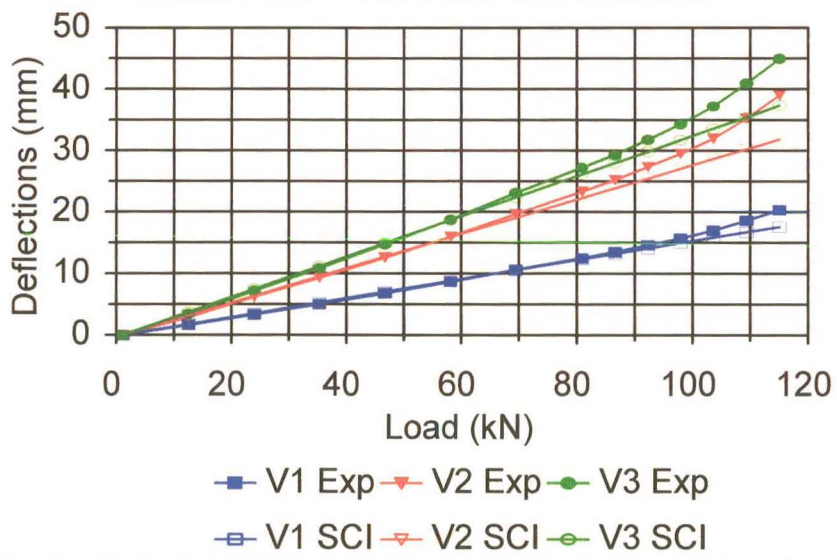
Comparison with SCI

Beam 2A - vertical deflections



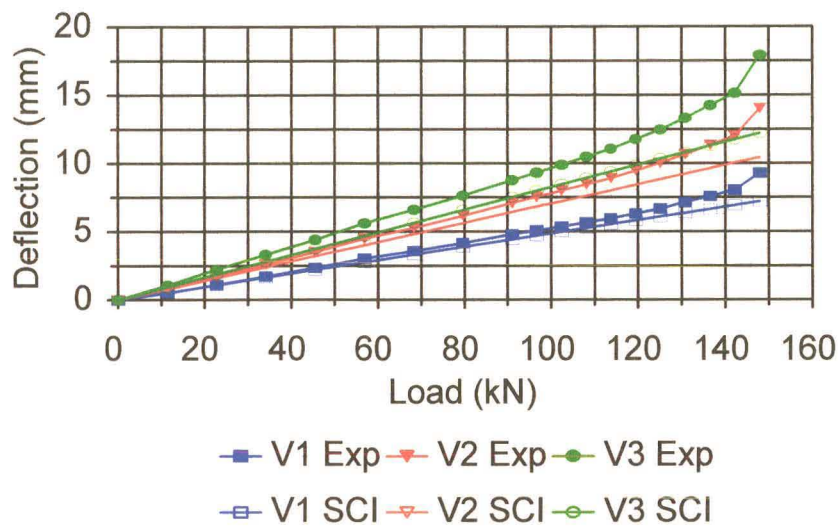
Comparison with SCI

Beam 2B - vertical deflections



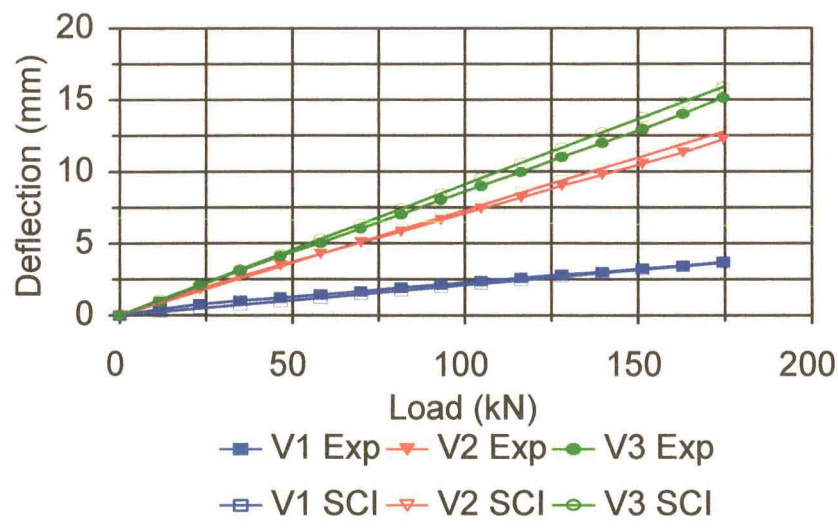
Comparison with SCI

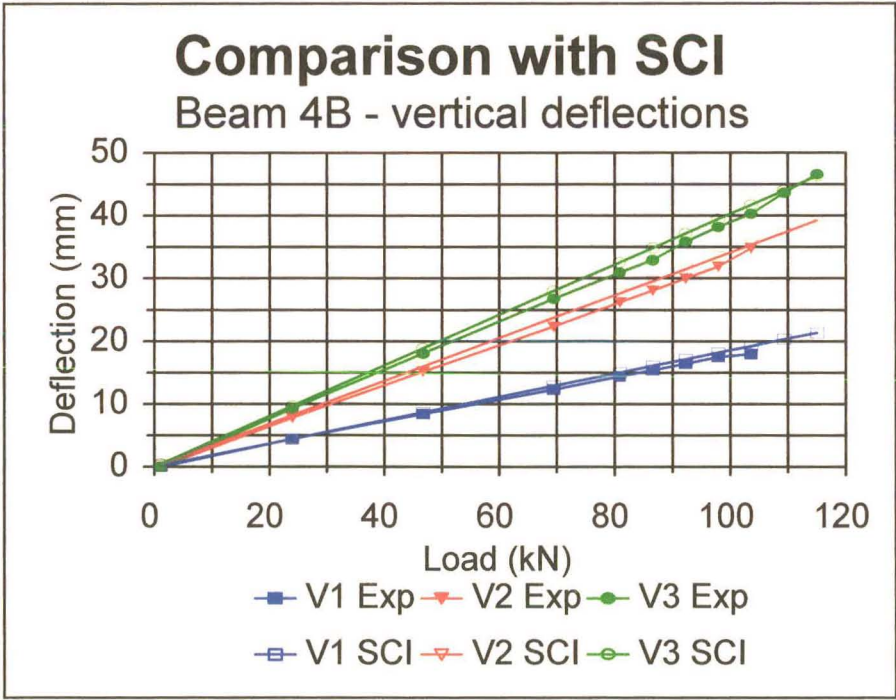
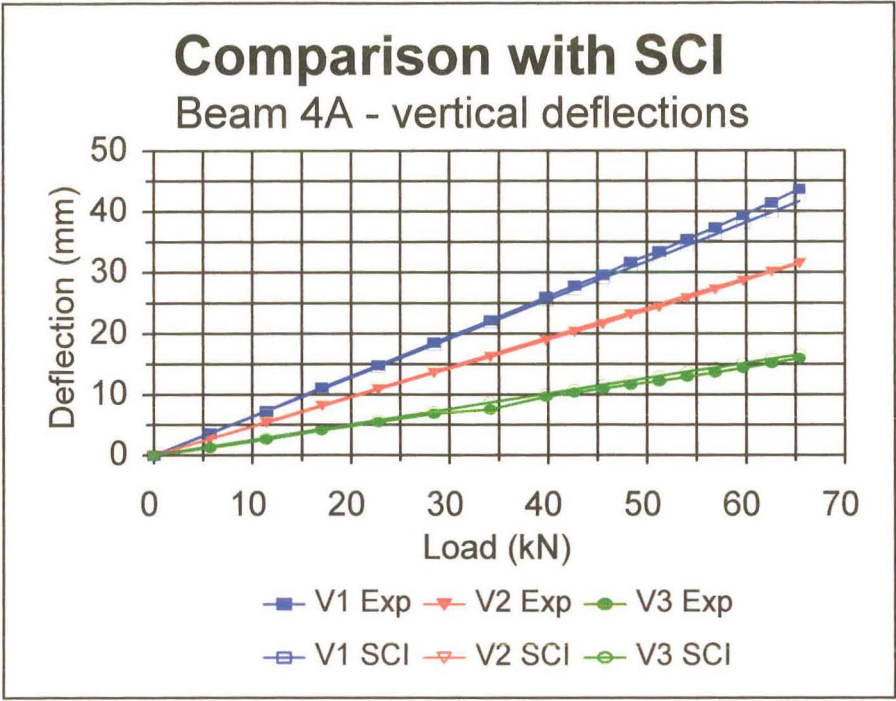
Beam 3A - vertical deflections



Comparison with SCI

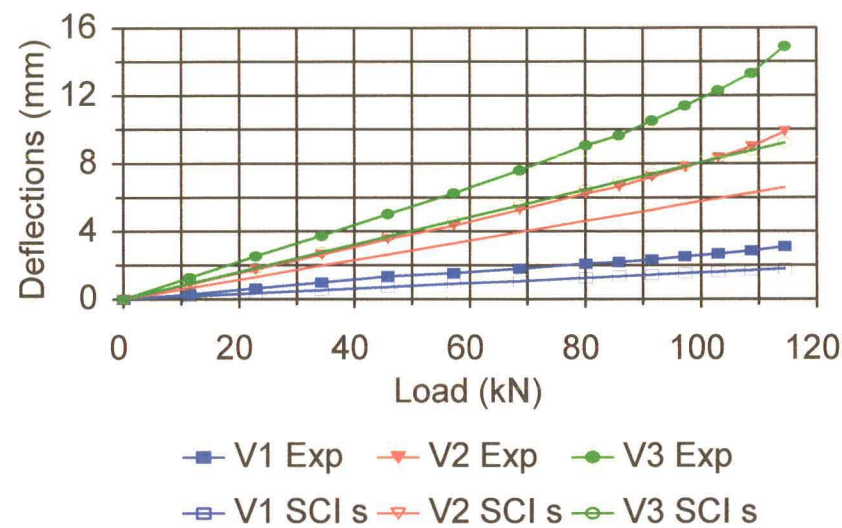
Beam 3B - vertical deflections



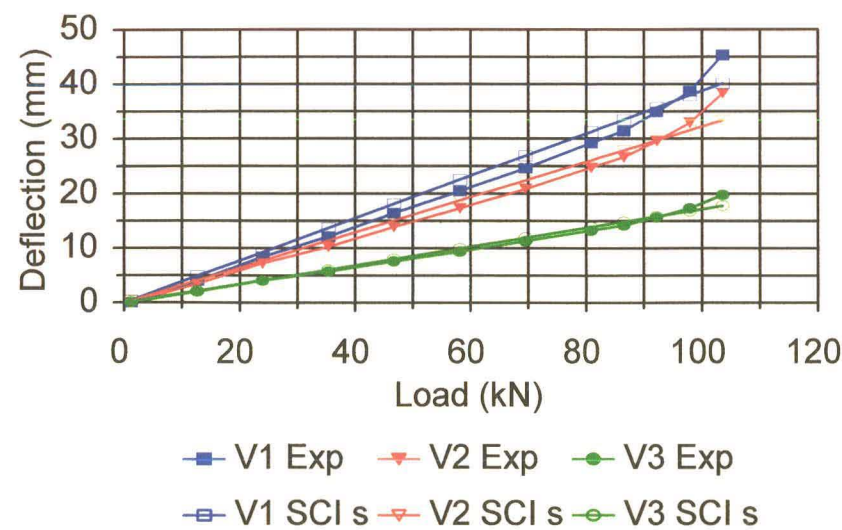


Simplified SCI method

Comparison with simplified SCI
Beam 1A - vertical deflections

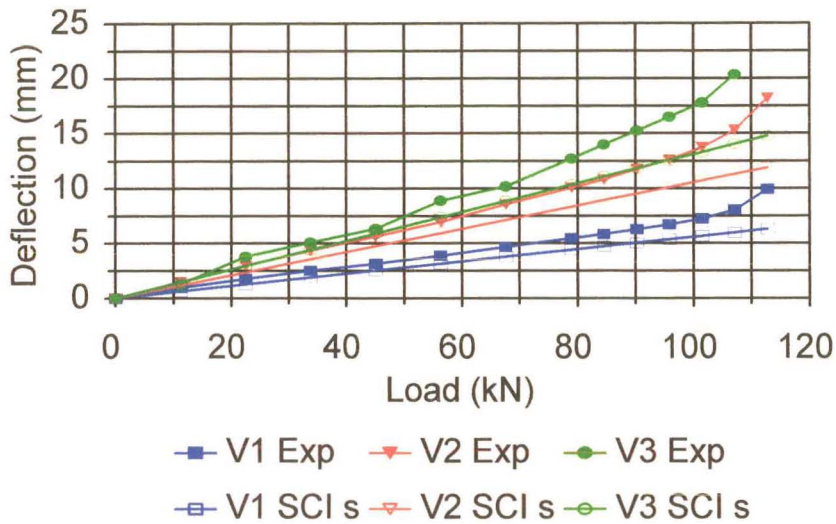


Comparison with simplified SCI
Beam 1B - vertical deflections



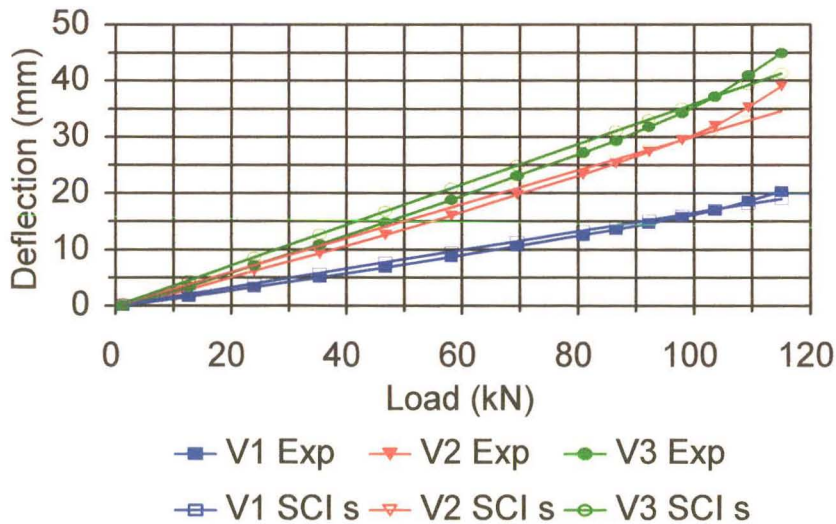
Comparison with simplified SCI

Beam 2A - vertical deflections



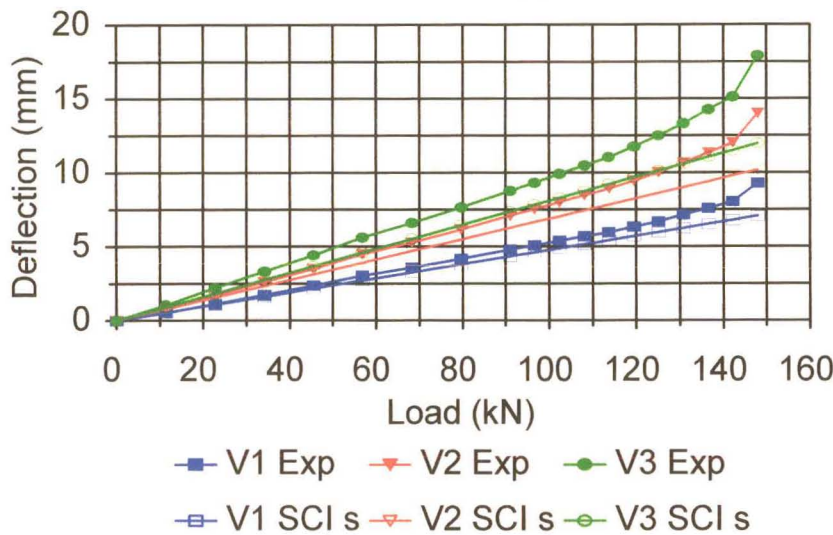
Comparison with simplified SCI

Beam 2B - vertical deflections



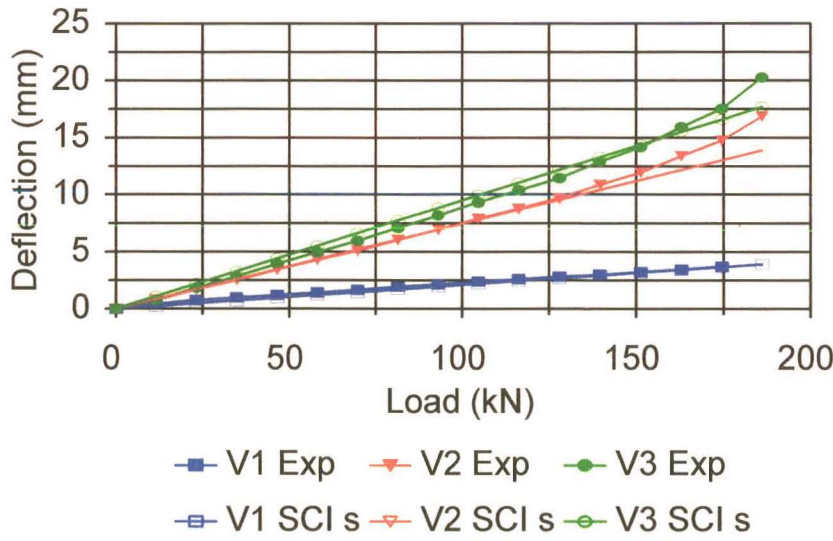
Comparison with simplified SCI

Beam 3A - vertical deflections



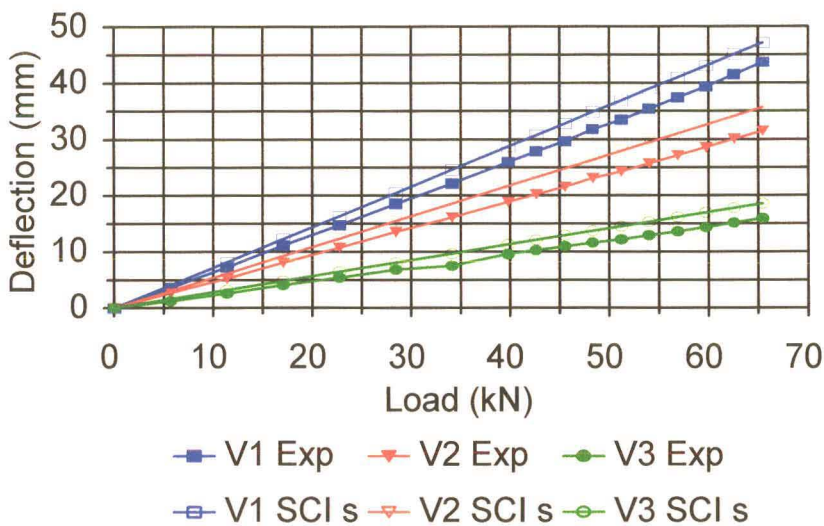
Comparison with simplified SCI

Beam 3B - vertical deflections



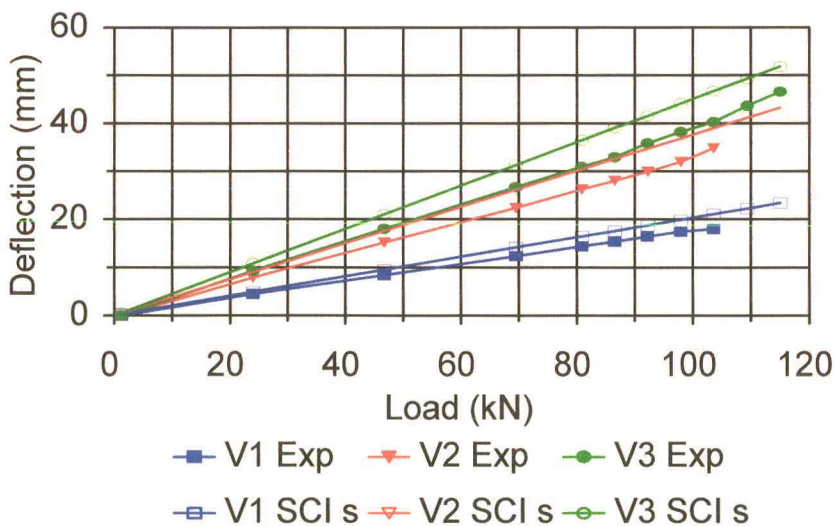
Comparison with simplified SCI

Beam 4A - vertical deflections

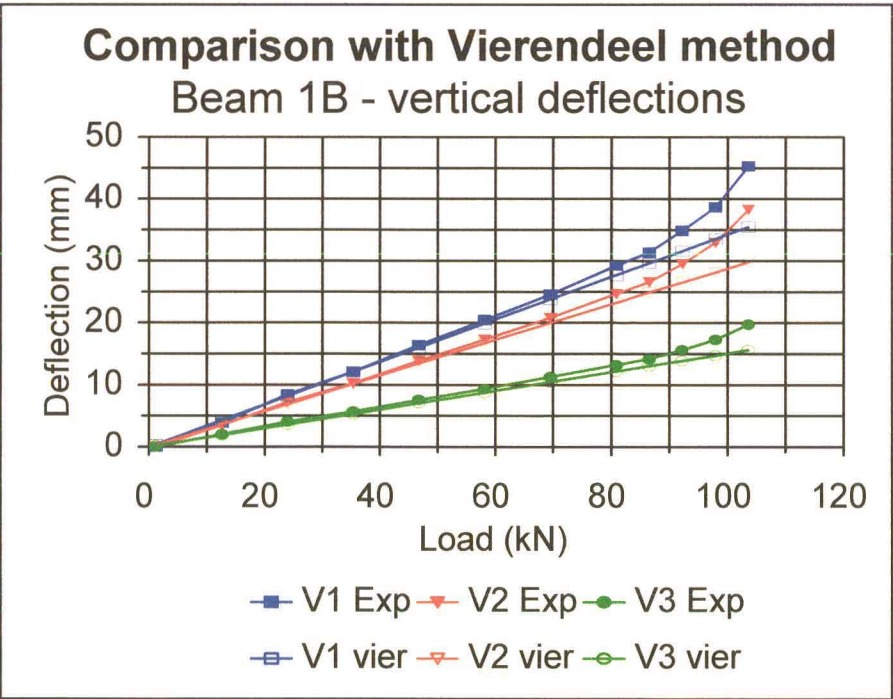
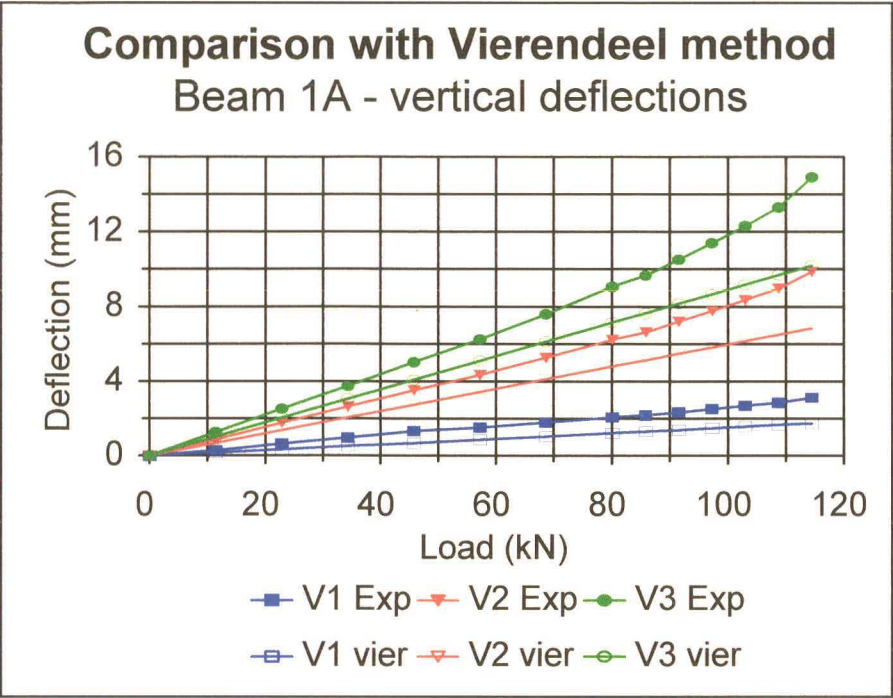


Comparison with simplified SCI

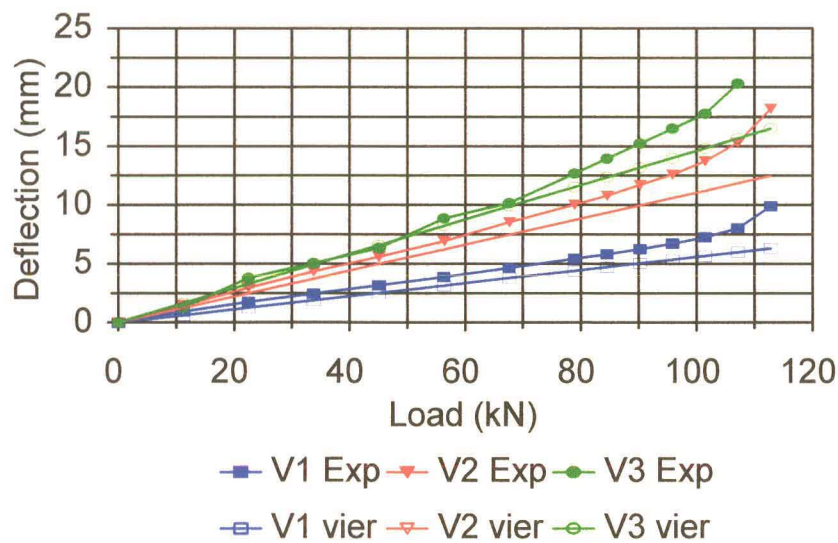
Beam 4B - vertical deflections



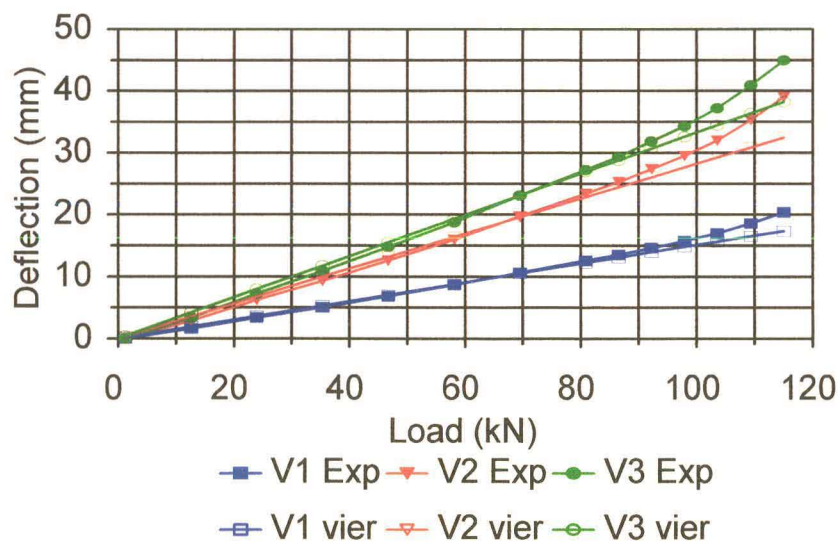
Vierendeel method

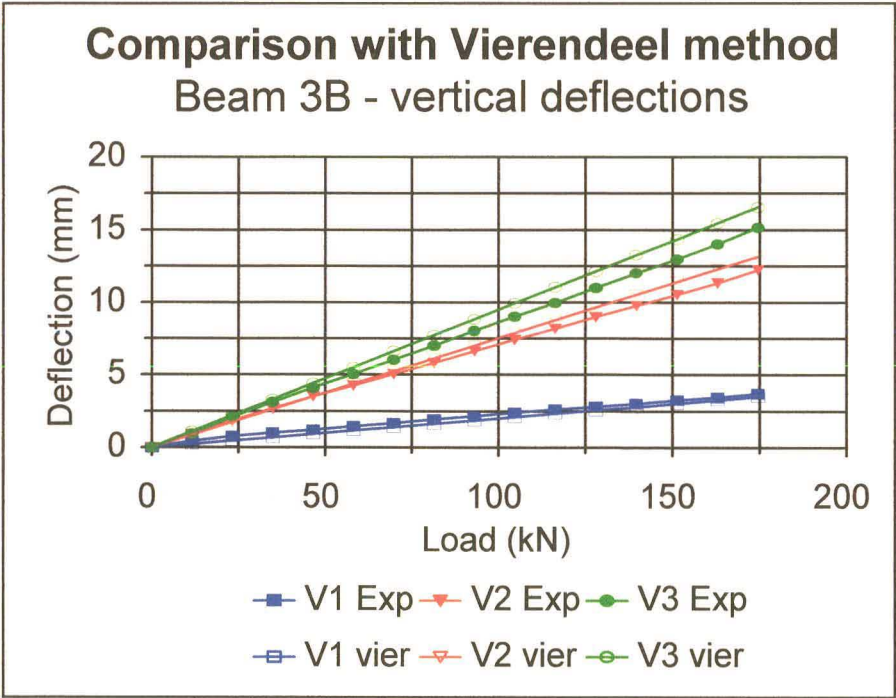
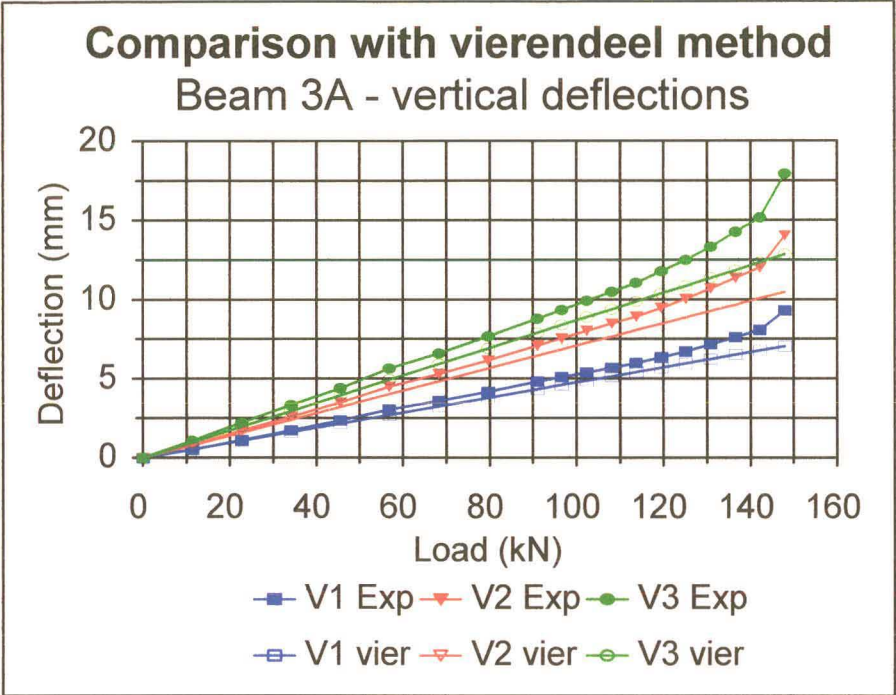


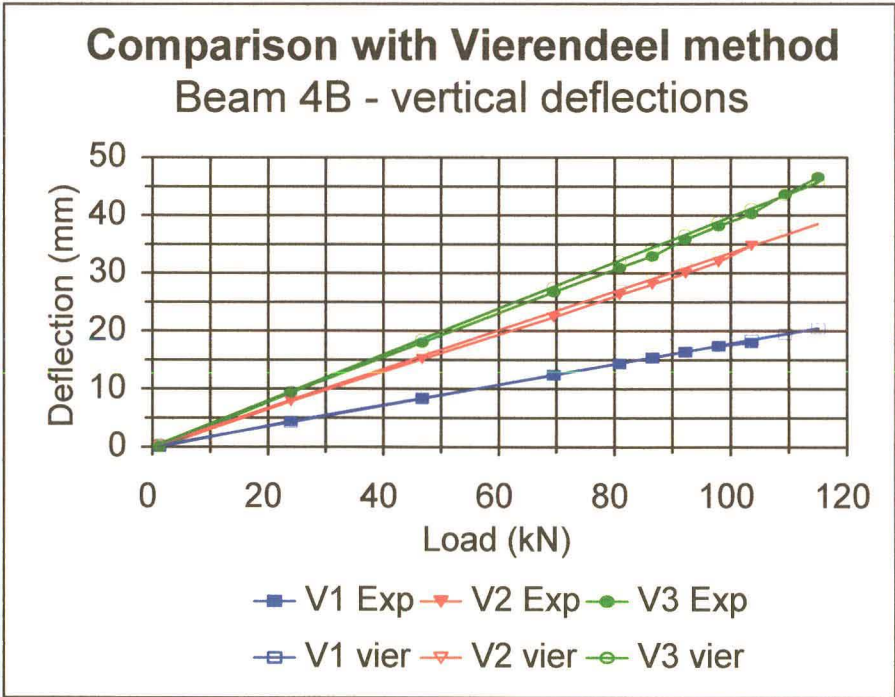
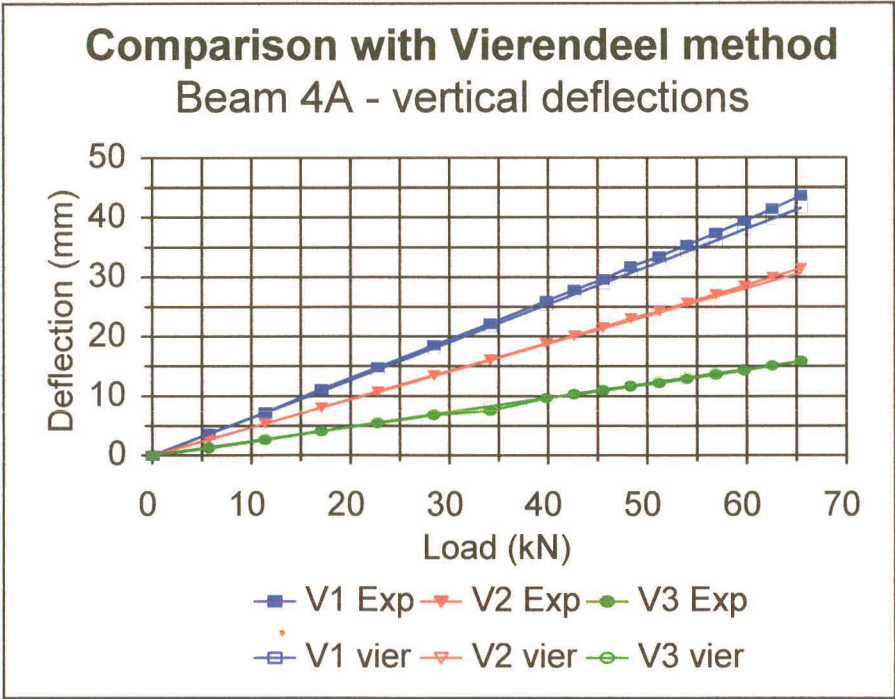
Comparison with Vierendeel method
Beam 2A - vertical deflections



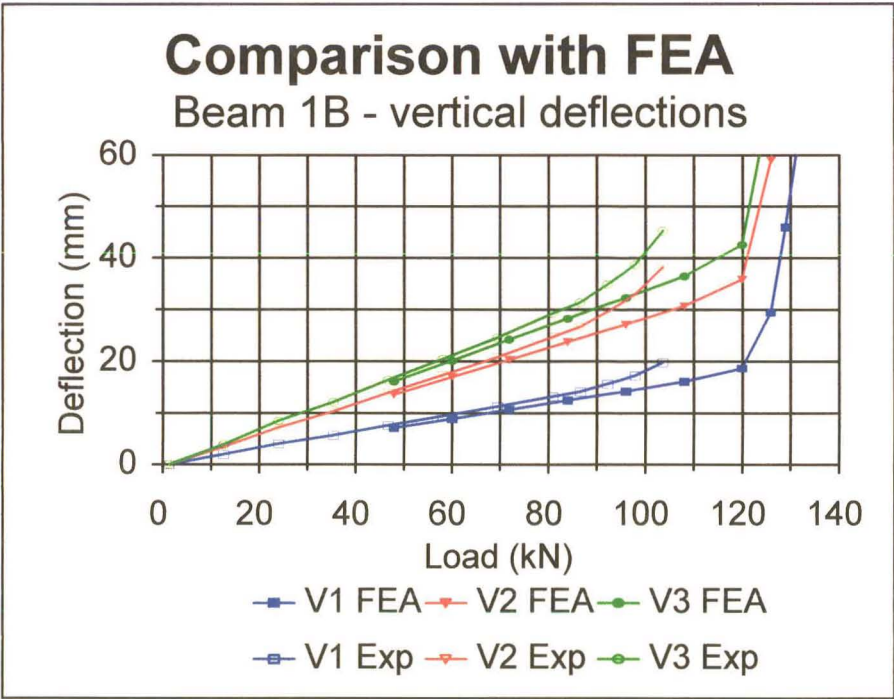
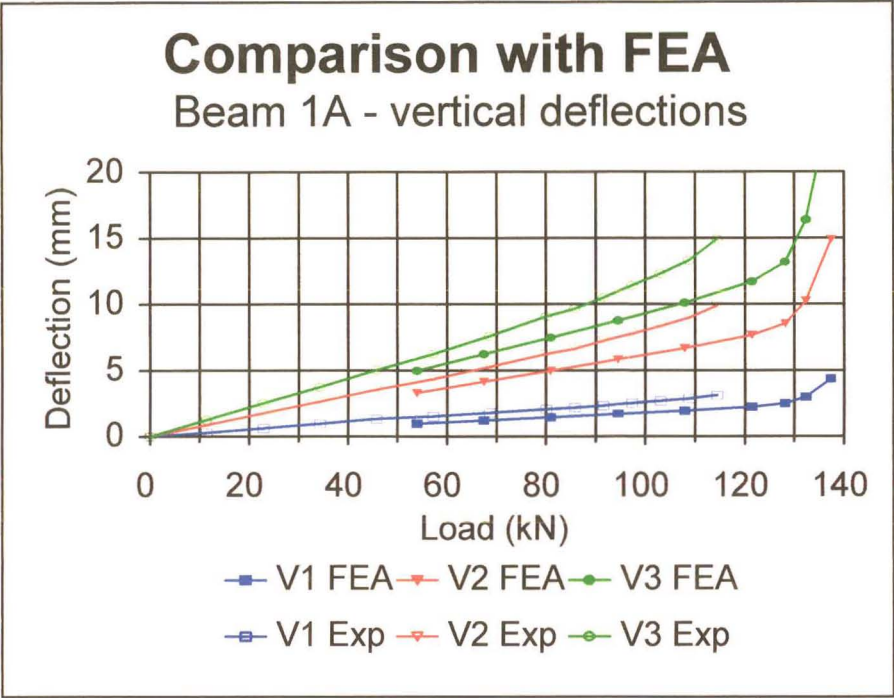
Comparison with Vierendeel method
Beam 2B - vertical deflections





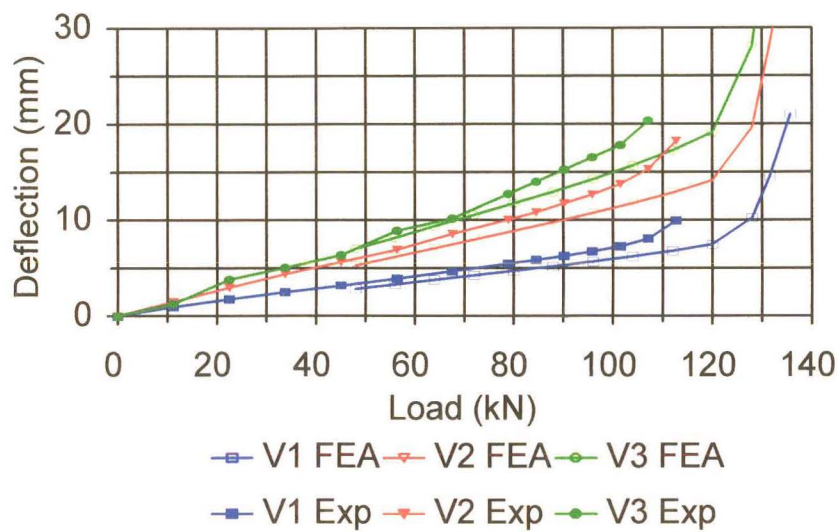


Finite Element Analysis method



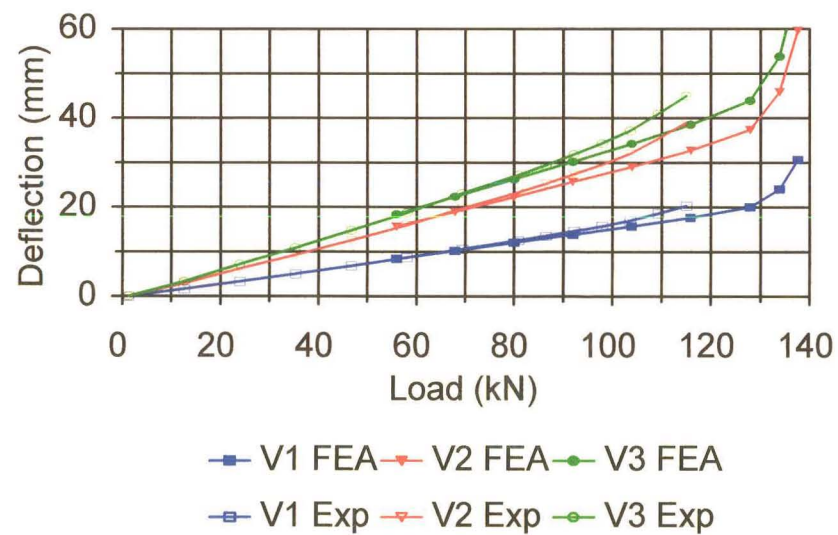
Comparison with FEA

Beam 2A - vertical deflections

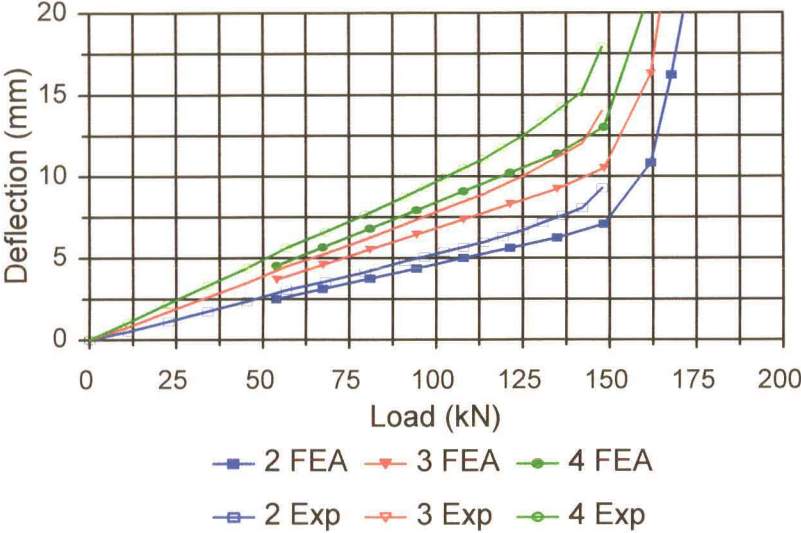


Comparison with FEA

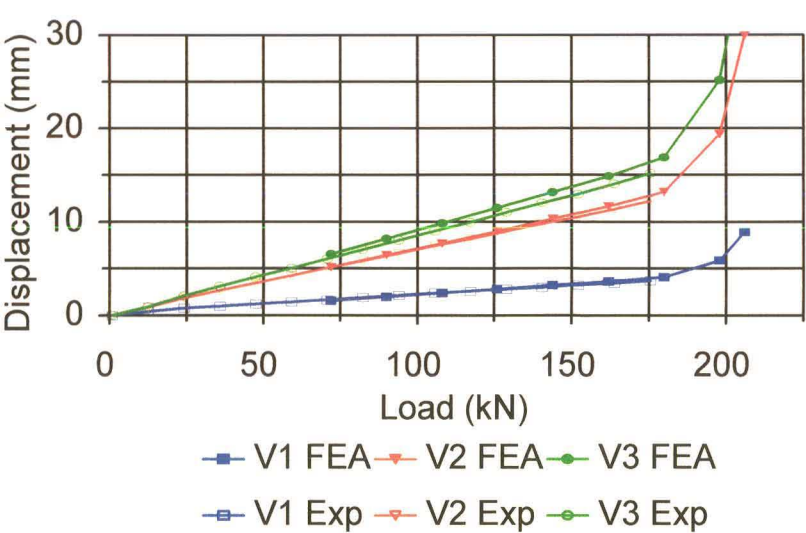
Beam 2B - vertical deflections

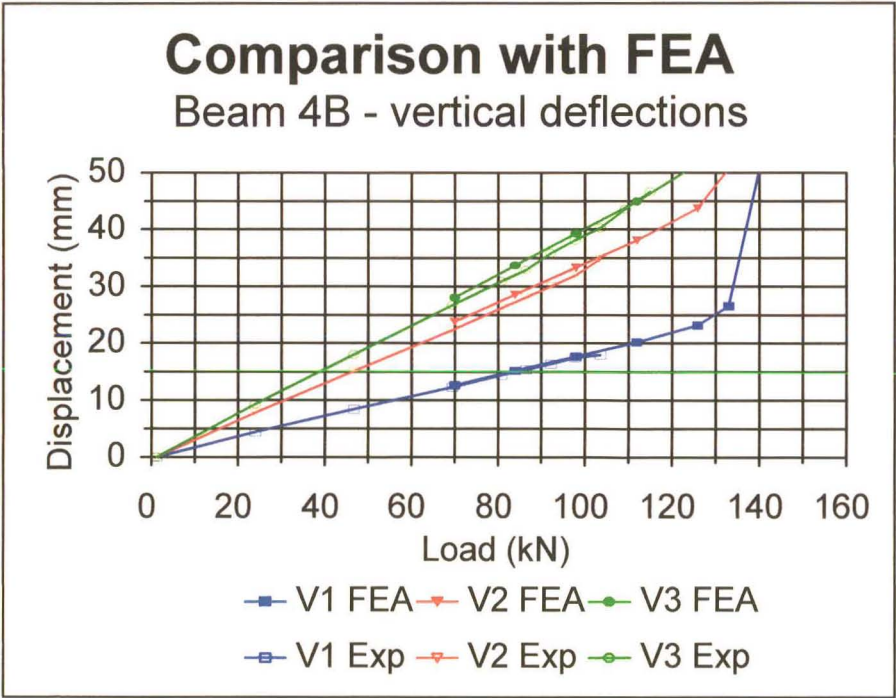
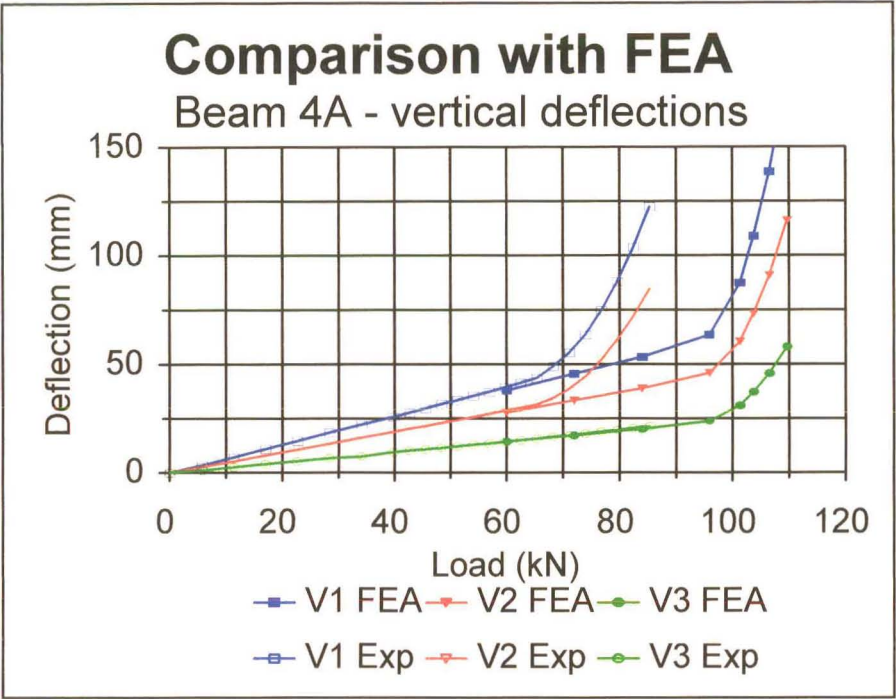


Comparison with FEA Beam 3A - vertical deflections



Comparison with FEA Beam 3B - vertical deflections





Deflection ratios for all dial gauges

Beam	Gauge	SCI	Simplified SCI	Vierendeel	FEA
1A	V1	0,64	0,60	0,59	0,69
	V2	0,78	0,73	0,75	0,78
	V3	0,72	0,69	0,77	0,81
1B	V1	1,55	1,05	0,92	0,91
	V2	1,20	1,07	0,95	0,94
	V3	1,09	1,08	0,96	0,94
2A	V1	0,78	0,80	0,80	0,85
	V2	0,84	0,82	0,86	0,87
	V3	0,85	0,80	0,90	0,91
2B	V1	1,01	1,09	1,00	1,01
	V2	0,99	1,08	1,01	1,01
	V3	0,99	1,10	1,02	1,02
3A	V1	0,91	0,89	0,89	0,87
	V2	0,89	0,87	0,89	0,87
	V3	0,83	0,82	0,88	0,86
3B	V1	0,93	0,93	0,88	0,99
	V2	0,96	0,98	0,99	0,94
	V3	1,01	1,06	1,05	1,02
4A	V1	1,06	1,19	1,01	1,02
	V2	1,02	1,14	0,99	0,98
	V3	0,97	1,10	0,97	0,98
4B	V1	1,05	1,15	1,01	1,02
	V2	1,04	1,15	1,03	1,05
	V3	1,03	1,15	1,02	1,03